

ELECTROMAGNETIC SCATTERING FROM A SHIP AT SEA

John Huang and W. H. Peake

OSU

LEVEL

NA

ADA 081118

The Ohio State University

ElectroScience Laboratory

Department of Electrical Engineering
Columbus, Ohio 43212

Final Report 710660-2

September 1978

Contract N60530-77-C-0218

DTIC
ELECTE
FEB 27 1980
A

DDC FILE COPY

Department of the Navy
Naval Weapons Center
China Lake, California 93555

DISTRIBUTION STATEMENT A

Approved for public release;
Distribution Unlimited

80 2 26 031

NOTICES

When Government drawings, specifications, or other data are used for any purpose other than in connection with a definitely related Government procurement operation, the United States Government thereby incurs no responsibility nor any obligation whatsoever, and the fact that the Government may have formulated, furnished, or in any way supplied the said drawings, specifications, or other data, is not to be regarded by implication or otherwise as in any manner licensing the holder or any other person or corporation, or conveying any rights or permission to manufacture, use, or sell any patented invention that may in any way be related thereto.

UNCLASSIFIED

SECURITY CLASSIFICATION OF THIS PAGE (When Data Entered)

REPORT DOCUMENTATION PAGE		READ INSTRUCTIONS BEFORE COMPLETING FORM
1. REPORT NUMBER Final rept. 15 Aug 77 - 18 Aug 78	2. GOVT ACCESSION NO.	3. RECIPIENT'S CATALOG NUMBER
4. TITLE (and Subtitle) ELECTROMAGNETIC SCATTERING FROM A SHIP AT SEA.	5. TYPE OF REPORT & PERIOD COVERED Final Report 08/15/77 - 08/18/78	6. PERFORMING ORG. REPORT NUMBER ESL-710660-2
7. AUTHOR(s) John Huang and W. H. Peake	8. CONTRACT OR GRANT NUMBER(s) Contract N60530-77-C-0218	
9. PERFORMING ORGANIZATION NAME AND ADDRESS The Ohio State University ElectroScience Laboratory, Department of Electrical Engineering, Columbus, Ohio 43212	10. PROGRAM ELEMENT, PROJECT, TASK AREA & WORK UNIT NUMBERS Project 3310-0332-77	
11. CONTROLLING OFFICE NAME AND ADDRESS Department of the Navy Naval Weapons Center China Lake, California 93555	12. REPORT DATE September 1978	
14. MONITORING AGENCY NAME & ADDRESS (if different from Controlling Office) 129 LEE	13. NUMBER OF PAGES 125	
	15. SECURITY CLASS. (of this report) Unclassified	
	15a. DECLASSIFICATION/DOWNGRADING SCHEDULE	
16. DISTRIBUTION STATEMENT (of this Report) DISTRIBUTION STATEMENT A Approved for public release Distribution Unlimited		
17. DISTRIBUTION STATEMENT (of the abstract entered in Block 20, if different from Report)		
18. SUPPLEMENTARY NOTES The material contained in this report was also used as a dissertation submitted to the Ohio State University Department of Electrical Engineering.		
19. KEY WORDS (Continue on reverse side if necessary and identify by block number) Radar signature Ship-sea scattering model Radar cross-section Composite surface		
20. ABSTRACT (Continue on reverse side if necessary and identify by block number) A simplified model is developed to analyze the high frequency electromagnetic scattering from a ship at sea. The ship is modelled by an elliptic cylinder to represent the superstructure, superim- posed on a portion of an elliptic cone to represent the hull struc- ture. The Geometrical Theory of Diffraction in conjunction with an efficient specular point tracking algorithm is employed to cal- culate the scattering from this ship model. The sea surface is		

DD FORM 1 JAN 73 1473

EDITION OF 1 NOV 65 IS OBSOLETE

UNCLASSIFIED

SECURITY CLASSIFICATION OF THIS PAGE (When Data Entered)

402 251

y/b

UNCLASSIFIED

SECURITY CLASSIFICATION OF THIS PAGE(When Data Entered)

20.

replaced by a "rectangular patch" model which divides the antenna illuminated sea surface into square sub-areas. The scattering from each sub-area is represented by a polarization transforming reflection coefficient derived from the bistatic radar cross-section of the patch. The cross-section used here is that of the composite model in which the scattering cross-section of the ocean is derived from the sum of the geometrical optics cross-section (which predominates in the forward scatter direction and is controlled by the large scale slope distribution of the ocean) and the slope averaged Bragg scatter (which predominates in the back-scatter direction and is controlled by the height spectrum of the ocean).

In general, there are three basic scattering mechanisms that contribute to the total signature as the radar system traverses the ship target. These are the direct back-scattered signal from the sea surface (the so-called clutter component), the ship-sea double-bounce interaction term, and the signature scattered by the ship alone. A number of signatures, for various trajectories, antenna patterns, and polarizations have been calculated, and are used to illustrate the effect of the aspect angle of the trajectory, the curvature of the hull, etc. on the detectability of the ship in clutter, and the relations between the position of the ship and the position of the peak signature voltage.

UNCLASSIFIED

SECURITY CLASSIFICATION OF THIS PAGE(When Data Entered)

The authors wish to express their appreciation to Dr. W. D. Burnside for his guidance in the field of Geometrical Theory of Diffraction. Special thanks is extended to Dr. P. H. Pathak and Dr. R. J. Marhefka for their many consultations and assistance and to Dr. E. Pelton for providing the measurements of the field scattered by a cone described in Appendix D.

The authors wish to express their appreciation to Dr. W. D. Burnside for his guidance in the field of Geometrical Theory of Diffraction. Special thanks is extended to Dr. P. H. Pathak and Dr. R. J. Marhefka for their many consultations and assistance and to Dr. E. Pelton for providing the measurements of the field scattered by a cone described in Appendix D.

[illegible]

TABLE OF CONTENTS

	Page
ACKNOWLEDGMENTS.....	ii
LIST OF FIGURES.....	v
 Chapter	
I INTRODUCTION.....	1
II THE 3-DIMENSIONAL SIMPLIFIED SHIP-SEA MODEL.....	4
III INTRODUCTION TO GEOMETRICAL THEORY OF DIFFRACTION.....	8
A. Reflected Field from a Curved Surface	8
B. Diffraction by a Straight Wedge	10
C. Diffraction by a Curved Wedge	14
IV SEA SCATTERING CHARACTERISTICS.....	18
A. The Bragg Component; Slightly Rough Surface Scattering	20
B. The Specular Component; Very Rough Surface Scattering	23
C. The Composite Cross-Section	
1. Backscatter	26
2. Bistatic scatter	27
V DOUBLE-REFLECTION SIGNATURE FROM THE SHIP-SEA INTERACTION	28
A. Numerical Search Technique for Points of Reflection	28
B. Reflection from the Elliptical Cylinder	31
C. Test Cases: The Elliptic Cylinder; The Reflection Points	34
D. Results	43
VI SHIP SCATTERED SIGNATURES.....	56
A. Corner Reflected Signature	57
B. Diffracted-Reflected Signatures	57

VII	COMBINED SOLUTIONS WITH A CONICAL SHIP HULL AND DIFFERENT ANTENNA PATTERNS.....	69
VIII	CONCLUSIONS AND RECOMMENDATIONS.....	106
Appendix		
A	PENCIL BEAM RADIATION FROM RECTANGULAR APERTURE.....	108
B	BISTATIC SCATTERING MATRIX ELEMENTS (SLIGHTLY ROUGH SURFACE).....	110
C	BISTATIC SPECULAR REFLECTION COEFFICIENTS (VERY ROUGH SURFACE).....	111
D	COMPARISON OF THE MEASURED AND CALCULATED FIELDS SCATTERED BY A CIRCULAR CONE.....	113
	REFERENCES.....	123

LIST OF FIGURES

Figure		Page
1	Basic ship-sea model.....	1
2	Simplified models of the ship's hull and superstructure.....	4
3	Geometry of the cylinder and rectangular patch model.....	6
4	Reflection from a curved surface.....	8
5	Geometry for three dimensional wedge diffraction.	11
6	Geometry for three-dimensional curved wedge diffraction problem.....	16
7	Definition of surface for wedge diffraction problem.....	17
8	Surface arrangement and scattering geometry.....	19
9	Measured and model waveheights temporal spectra and radar cross sections.....	23
10	Geometry of bistatic cross-section.....	25
11	Sub-divided patches of the illuminated sea surface.....	29
12	Geometry for field reflected from elliptical cylinder.....	32
13	Reflection coordinate transformation system on the elliptic cylinder.....	33
14	Configuration for the reflected field pattern measurement.....	35
15	Reflected field pattern for the geometrical configuration shown in Figure 14.....	36

16	Characteristic views of elliptic cylinder and position matrix for broadside incidence.....	37
17	Reflection points versus the sub-area location for the case shown in Figure 16.....	38
18	Reflection points versus the sub-area location for the case shown in Figure 16.....	39
19	Characteristic view of elliptical cylinder and position matrix for off-broadside incidence of the antenna.....	40
20	Reflection points versus the sub-area location for the case shown in Figure 19.....	41
21	Reflection points versus the sub-area location for the case shown in Figure 19.....	42
22	Configuration of elliptical cylinder at sea.....	44
23	Voltage signature for the model of Figure 22, antenna approach angle $SAH=0^\circ$	45
24	Voltage signature for the model of Figure 22, antenna approach angle $SAH=45^\circ$	46
25	Voltage signature for the model of Figure 22, antenna approach angle $SAH=90^\circ$	47
26	Ship-sea double-bounce signal plus the ocean back-scattered signal for the geometrical model of Figure 22, antenna approach angle $SAH=0^\circ$	49
27	Ship-sea double-bounce signal plus the ocean back-scattered signal for the geometrical model of Figure 22, antenna approach angle $SAH=45^\circ$	50
28	Ship-sea double-bounce signal plus the ocean back-scattered signal for the geometrical model of Figure 22, antenna approach angle $SAH=90^\circ$	51
29	Ship-sea double-bounce signatures.....	54
30	Direct wedge diffractions showing the shadow boundaries.....	56

31	Corner reflection configurations.....	58
32	Top view of the ship's corner reflection.....	58
33	Configuration of two superimposed elliptic cylinders with respect to the antenna position.....	59
34	Corner reflected signatures between the two cylinders.....	60
35	Ship scattering mechanisms for diffracted-reflected signature.....	61
36	Top view of the diffracted-reflected configuration.....	62
37	Configuration of the initial scattering points for the search equation.....	64
38	Diffracted-reflected fields between two elliptic cylinders.....	65
39	Diffracted-reflected field configuration.....	66
40	The diffracted-reflected field between two elliptic cylinders for the geometry shown in Figure 39.....	67
41	The diffracted-reflected field between two elliptic cylinders for the geometry shown in Figure 39.....	68
42	Total received field calculated when ship is represented by two elliptic cylinders, antenna approach angle $SAH=0^{\circ}$	70
43	Ship-sea scattered signature for the same geometrical configuration as for Figure 42 except that $SAH=45^{\circ}$	71
44	Ship-sea scattered signature for the same geometrical configuration as that for Figure 42 except that $SAH=90^{\circ}$	72
45	Geometrical configuration of the ship and antenna trajectory. The ship hull is an elliptic cone..	74
46	Elliptic cone configuration.....	75

47	Initial location of (v, z_R) on the elliptic cone for the numerical search technique.....	77
48	Configuration for sea scattered signature collected beyond the ship.....	79
49	Total scattered signature for the ship with a conical hull, antenna approach angle $SAH=0^\circ$	80
50	Total scattered signature for the ship with a conical hull, antenna approach angle $SAH=45^\circ$	81
51	Total scattered signature for the ship with a conical hull, antenna approach angle $SAH=90^\circ$...	82
52	Conical antenna pattern.....	83
53	Total scattered signature from the sea and a ship with conical hull. Hollow cone antenna pattern is used. $SAH=0^\circ$, $ATA=60^\circ$	86
54	Total scattered signature from the sea and a ship with conical hull. Hollow cone antenna pattern is used. $SAH=45^\circ$, $ATA=60^\circ$	87
55	Total scattered signature from the sea and a ship with conical hull. Hollow cone antenna pattern is used. $SAH=90^\circ$, $ATA=60^\circ$	88
56	Total scattered signature from the sea and a ship with conical hull. Hollow cone antenna pattern is used. $SAH=0^\circ$, $ATA=30^\circ$	90
57	Total scattered signature from the sea and a ship with conical hull. Hollow cone antenna pattern is used. $SAH=45^\circ$, $ATA=30^\circ$	90
58	Total scattered signature from the sea and a ship with conical hull. Hollow cone antenna pattern is used, $SAH=90^\circ$, $ATA=30^\circ$	91
59	Total scattered signature from the sea and a ship with conical hull. Hollow cone antenna pattern is used. $SAH=0^\circ$, $ATA=60^\circ$, polarization is horizontal.....	92

60	Total scattered signature from the sea and a ship with conical hull. Hollow cone antenna pattern is used. $SAH=45^{\circ}$, $ATA=60^{\circ}$ polarization is horizontal.....	93
61	Total scattered signature from the sea and a ship with conical hull. Hollow cone antenna pattern is used. $SAH=90^{\circ}$, $ATA=60^{\circ}$, polarization is horizontal.....	94
62	Total scattered signature from the sea and a ship with conical hull. Hollow cone antenna pattern is used, $SAH=0^{\circ}$, $ATA=30^{\circ}$, polarization is horizontal.....	95
63	Total scattered signature from the sea and a ship with conical hull. Hollow cone antenna pattern is used. $SAH=45^{\circ}$, $ATA=30^{\circ}$, polarization is horizontal.....	96
64	Total scattered signature from the sea and a ship with conical hull. Hollow cone antenna pattern is used. $SAH=90^{\circ}$, $ATA=30^{\circ}$ polarization is horizontal.....	97
65	Actual model and simplified model of ship U.S.S. Missouri.....	98
66	Ship-sea scattered signature from the simplified U.S.S. Missouri model. $SAH=0^{\circ}$, $ATA=60^{\circ}$	99
67	Ship-sea scattered signature from the simplified U.S.S. Missouri model. $SAH=45^{\circ}$, $ATA=60^{\circ}$	100
68	Ship-sea scattered signatures from the simplified U.S.S. Missouri model. $SAH=90^{\circ}$, $ATA=60^{\circ}$	101
69	Ship-sea scattered signature from the simplified U.S.S. Missouri model. $SAH=0^{\circ}$, $ATA=30^{\circ}$	102
70	Ship-sea scattered signature from the simplified U.S.S. Missouri model. $SAH=45^{\circ}$, $ATA=30^{\circ}$	103
71	Ship-sea scattered signature from the simplified U.S.S. Missouri model. $SAH=90^{\circ}$, $ATA=30^{\circ}$	104

72	Improved U.S.S. Missouri model.....	105
73	Source coordinate system.....	108
74	Geometry and scattering mechanisms for the circular cone.....	114
75	Diffraction mechanism for creeping wave.....	115
76	Developed cone surface.....	116
77	Configuration of surface diffracted creeping wave.....	118
78	Configuration of curved surface reflection.....	120
79	Field scattered from the circular cone.....	122

CHAPTER I INTRODUCTION

When an antenna is transmitting or receiving in the vicinity of the sea surface, the desired signal is usually contaminated by the presence of signal components that have been scattered from the sea. This form of interference generally degrades system performance unless the system can be designed to take advantage of any differences between the properties of the sea-scattered and the desired signals. The desired signal, in this study, is the radar return due to the presence of a ship. In order to determine the characteristics of this signal and to obtain a better understanding of the sea and ship scattering mechanisms, we have chosen to study the scattered signals through the use of a mathematical model. Such a model should be complex enough to realistically reproduce all the significant features of the real situation, while remaining computationally tractable. The basic form of the model developed here is illustrated in Figure 1 where the ship is modelled by a pair of elliptic cylinders which are taken to represent the ship's hull and superstructure. Although this structure is relatively simple, the model has the potential of handling considerably more complex structural features without any fundamental change in the computational process. Also in Figure 1 the actual sea surface is replaced, in the model, by a set of square patches which divides area illuminated by the antenna into sub-areas.

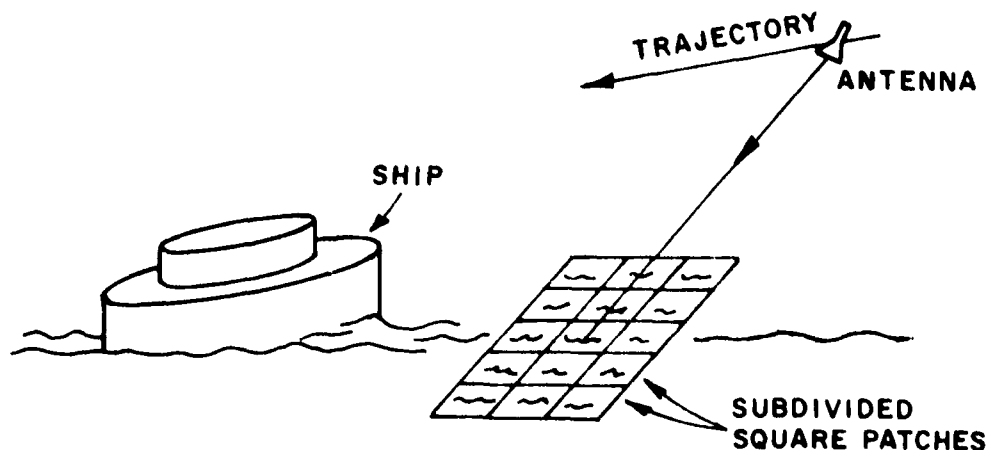


Figure 1. Basic ship-sea model.

As the radar system traverses the ship target, a signature (typically the detector voltage versus time) is generated. There are generally three principal contributions to the total signature. The first of these is the direct backscattered signal from the sea surface, usually referred to as the sea clutter signal. The second is the "double-bounce" corner term formed by any scattering path from transmitter to sea surface to ship and back to receiver (and vice versa). The third type of contribution is the scattered signal from the ship alone, predominantly due to reflection and diffraction from the ship's surfaces and edges. The object of the work reported here is the prediction of these three principal signatures. They will be analyzed by two separate techniques, namely the statistically rough surface theories for the sea scattering, and the Geometrical Theory of Diffraction (GTD) for the ship scattering.

The calculation of scattering of the electromagnetic field by the sea surface, which includes both forward and back scattering, is itself based on a model, in this case the "composite" model, in which a slightly rough surface is superimposed on a larger scale structure. Perturbation theory is used to find the Bragg scatter from the small scale structure, and the methods of Geometrical Optics are employed for scattering from the large scale (gravity wave) structure. The scattered fields are then formulated in terms of the bistatic radar cross section of each patch, as computed by the above two statistical rough surface theories. Chapter IV discusses the characteristics of the sea surface scattering in more detail.

Both the Physical Optics method and the Geometrical Theory of Diffraction (GTD) have been investigated for the calculation of the electromagnetic scattering from the ship. It was found that the GTD is not only more effective in computing the scattering from such objects as elliptic cylinders, plates, rectangular blocks, etc., but also allows one to gain more physical insight into the various scattering and diffraction mechanisms involved. Therefore the method of GTD, which is described in Chapter III, was chosen to formulate the problem of scattering from the ship.

Finally, in order to determine the double-bounce ship-sea interaction term, we have again used the GTD, in which the sea-scattered fields from each patch are represented as a new source. To carry out this procedure, it is essential to locate accurately the reflection point on the surface of the ship's hull. Since huge numbers of patches might be involved if the area illuminated by the antenna is large, a great deal of time could be spent in just computing the reflection points. For this reason, a very efficient numerical search technique is developed to track the reflection point as the source moves from one sub-area to another. Chapter V has a detailed discussion of this technique.

The combined signatures for the complete model are considered in Chapter VII. In this chapter the hull form is changed from an elliptic cylinder to an elliptic cone so that the geometrical shape of the ship is physically more realistic. Also in the same chapter, the antenna pattern is modified from a pencil beam to a conical beam, so the effects of different antenna patterns on the signatures can be analyzed. In the concluding chapter, the general problem of detectability of a ship target in clutter, and some directions for further study are considered.

CHAPTER II

THE THREE DIMENSIONAL SIMPLIFIED SHIP-SEA MODEL

It is the purpose of this chapter to give a basic geometrical description of the simplified ship-sea model. In this model, the radar system is represented by a transmit/receive antenna of specified pattern, moving along a specified straight-line trajectory. Because the interest is in radar wavelengths much smaller than the characteristic dimensions of the ship, and in trajectories which transmit at relatively short range, the problem is formulated here in terms of the Geometrical Theory of Diffraction. The ship, as shown in Figure 2, is first modelled by a single elliptic cylinder

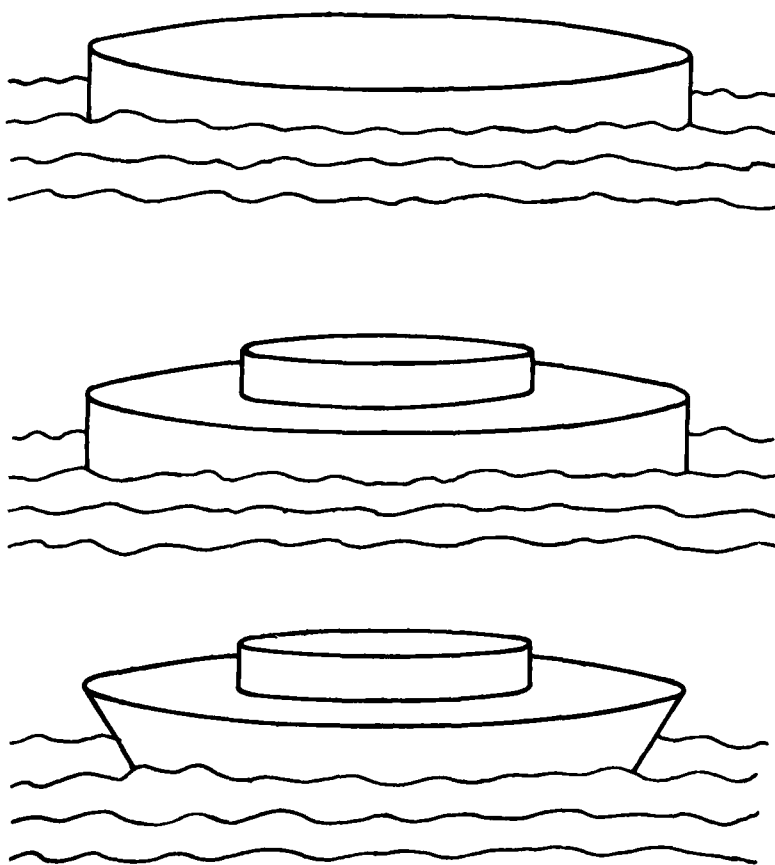


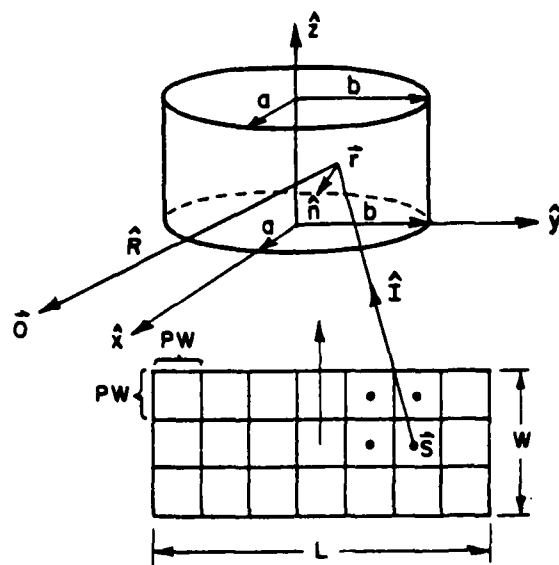
Figure 2. Simplified models of the ship's hull and superstructure.

representing the hull. Later on a smaller elliptic cylinder is added to the top to simulate the superstructure; and, finally, the ship's hull is modified to have the shape of an elliptic cone. Since the elliptic cylinders are three dimensional structures, a 3-D analysis is necessary.

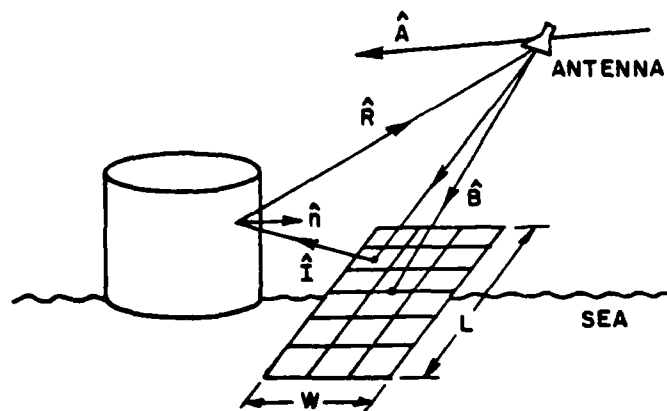
The basic geometry for the ship-sea interaction calculation is shown in Figure 3, in which the antenna is traveling in an arbitrary direction \vec{A} with its main beam axis (bore-sight) pointed in the direction \vec{B} and is illuminating the sea surface over an effective area of $W \times L$. This effective area, which is dependent on the transmitting antenna pattern, is broken up into smaller sub-areas. The scattering from each sub-area is entered into the GTD program as a polarization dependent scattering matrix element with scattering coefficients referred to the center of the sub-area. Each sub-area generates a direct backscattered field to form the sea clutter signal. The forward scattered field which is also generated from each sub-area then appears to come from a new source which in turn illuminates the metallic cylinder, and from which it is reflected to the receiver. The form of this doubly reflected field (the ship-sea interaction term) constitutes one of the major objectives of this research, because it represents one of the important contributions to the overall target signature. Even though this component of the scattered field is somewhat smaller than the signal scattered by the ship alone, it is, in many instances, a stronger signal than that due to the sea clutter. Since this doubly reflected field, whose existence is sometimes overlooked, occurs earlier than the ship scattered signal, it can play an important role in the overall system design, particularly when accurate range estimates are required.

The antenna radiation pattern, as will become apparent later, can also play an important role in the overall signature of the ship-sea model. However, for convenience, the antenna pattern is first chosen to be a pencil beam radiated from a rectangular aperture with Gaussian amplitude distribution in both planes. The rectangular aperture with its coordinate system and the radiated fields are given in Appendix A. Although a near field analysis is required to specify the range dependence of the radiated field (because the antenna may be in the near zone of the ship at the range of interest), it can be shown that the angular dependence of the antenna pattern is equivalent to a far field pattern.

Similarly, the details of the system electronics (detector type, range gate, doppler filters, etc.) can play an important role in the detectability of targets in clutter. For the purposes of this study, however, we have assumed that the emitted signal is a c.w. waveform proportional to $[Re V_0 \exp(2\pi j f_c t)]$ where V_0 is a transmitter reference voltage, f_c is the carrier frequency, and Re designates the real part of the complex expression. The model



(a) PERSPECTIVE TOP VIEW



(b) PERSPECTIVE SIDE VIEW

Figure 3. Geometry of the cylinder and rectangular patch model.

represents the received signal as a sum of contributions with well defined total path length r_n (e.g., for double bounce path, r_n is the round trip path length from transmitter, to patch center, to reflection point back to the receiver). Thus the received signal has the form

$$\text{Re} \sum_n V_n \exp(2\pi j f_c t - j k r_n + \delta_n)$$

where $k = 2\pi/\lambda$, V_n is an amplitude factor, and δ_n is a phase (possibly random) which depend on the scattering process for the particular contribution. The detector is assumed to be of the homodyne type with low pass filter, so that the detected signal $V_d(t)$ has the form

$$V_d(t) = \text{Re} \sum_n V_n \exp(-j k r_n + \delta_n).$$

This is the signal which is computed in the subsequent sections. Note that the doppler shift and the general time dependence of the waveform are contained implicitly in the constantly changing path lengths r_n .

CHAPTER III INTRODUCTION TO THE GEOMETRICAL THEORY OF DIFFRACTION (GTD)

In this chapter the basic GTD solutions used to analyze the simplified ship model are reviewed. The GTD is a high frequency technique that allows a complicated structure to be approximated by basic shapes such as flat plates, curved wedges and convex curved surfaces. It is a ray optical technique and therefore allows one to gain some physical insight into the various scattering and diffraction mechanisms involved. Consequently, one is able to quickly seek out the dominant or significant scattering mechanism for a given geometrical configuration. Several fundamental scattering mechanisms are used in the GTD calculation for the simplified ship model. They are: 1. Reflected field from a curved surface, 2. Diffraction by a straight wedge, and 3. Diffraction by a curved wedge. These scattering mechanisms are individually discussed below.

A. Reflected Field from a Curved Surface

The scattering problem studied here is that of the reflection of a given electromagnetic field $\vec{E}^i(Q_R)$ from a curved surface, as shown in Figure 4. The reflected electric field $\vec{E}^r(s)$ at the observation point is given, in the geometrical optics approximation, by

$$\vec{E}^r(s) = \vec{E}^i(Q_R) \cdot \vec{R} \sqrt{\frac{\rho_1^r \rho_2^r}{(\rho_1^r + s)(\rho_2^r + s)}} e^{-jks} \quad (1)$$

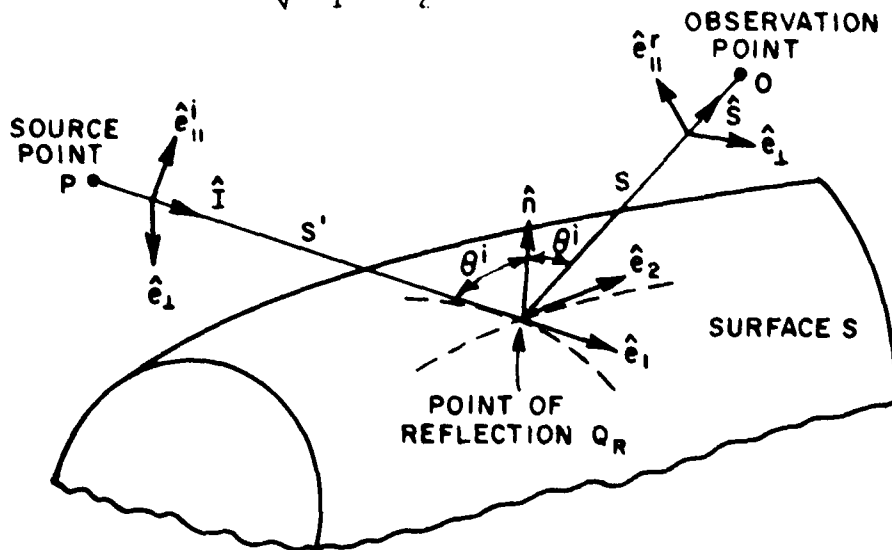


Figure 4. Reflection from a curved surface.

where $E^i(Q_R)$ is the incident electric field at the point of reflection Q_R due to a point source at P . The reflection point Q_R is found from the law of reflection, which requires that the angle of incidence be equal to the angle of reflection. It is determined by the relation

$$-\hat{l} \cdot \hat{n} = \hat{s} \cdot \hat{n} \quad (2a)$$

where \hat{l} is the incident unit vector, \hat{s} is the reflection unit vector, and \hat{n} is the surface normal unit vector. It is also required that all these unit vectors must lie in the same plane at the reflection point, so that

$$\hat{l} \times \hat{n} = \hat{s} \times \hat{n}. \quad (2b)$$

The dyadic reflection coefficient \hat{R} for a perfect conducting surface can be expressed as

$$\hat{R} = \hat{e}_n^i \hat{e}_n^r - \hat{e}_\perp^i \hat{e}_\perp^r \quad (3)$$

where \hat{e}_n^i and \hat{e}_n^r are the incident and reflected unit vector parallel to the plane of incidence (i.e., the plane containing the incident vector and the surface normal), and \hat{e}_\perp is the unit vector perpendicular to the plane of incidence. The quantities ρ_1 and ρ_2 are the principal radii of curvature of the reflected wavefront at the reflection point Q_R . Kouyoumdjian discusses in detail how to find these values for an arbitrary wavefront. For a spherical incident wavefront, the radii are given by

$$\frac{1}{\rho_1^r} = \frac{1}{s'} + \frac{1}{\cos \theta} \left[\frac{\sin^2 \theta_2}{R_1} + \frac{\sin^2 \theta_1}{R_2} \right] + \frac{1}{\cos^3 \theta} \left[\frac{\sin^2 \theta_2}{R_1} + \frac{\sin^2 \theta_1}{R_2} \right]^2 - \frac{4}{R_1 R_2} \quad (4)$$

where

s' is the radius of curvature of the incident wavefront at Q_R .

θ^i is the angle of incidence with $\cos \theta^i = \hat{n} \cdot \hat{s} = -\hat{n} \cdot \hat{l}$,

θ_1 is the angle between the incident ray and the principal surface tangent vector \hat{e}_1 ,

θ_2 is the angle between the incident ray and the principal surface tangent vector \hat{e}_2 .

R_1 and R_2 are the principal radii of curvature of the surface at Q_R .

s is the distance from Q_R to the observation point O .

B. Diffraction by a Straight Wedge

Even though the diffraction by a straight wedge has no direct application to the ship model we have chosen, it is discussed here because it is one of the most fundamental diffraction mechanisms in the GTD analysis and it is essential to understand it before considering the diffraction by a curved wedge in the next section.

An asymptotic solution for the diffraction from a conducting wedge was first obtained by Sommerfeld³. Pauli⁴ introduced the V_R function as a convenient formulation of the diffraction solution for a conducting wedge of finite angle.⁵ Later a plane wave diffraction coefficient was used by Keller⁵ in his original development of the GTD. Recently, however, Hutchins and Kouyoumjian⁶ have presented a formulation for the diffracted field which is significantly more accurate than the Pauli or Keller forms in the transition regions (near the incident and reflection shadow boundaries).

The three dimensional wedge diffraction problem is depicted in Figure 5. The incident field $E^i(s)$ is radiated from the source located at the point $S'(\rho', \phi', z')$. This can be an arbitrary electric or magnetic source producing a plane, a cylindrical or a spherical wave incident on the wedge. Kouyoumjian and Pathak⁷ have recently shown that the diffracted fields may be written compactly in terms of a dyadic diffraction coefficient if the fields are expressed in a ray-fixed coordinate system. The ray-fixed coordinate system is centered at the point of diffraction Q_F which is the so-called stationary phase point (a unique point for a given source and observation point). The incident ray diffracts as a cone of rays such that $\beta_0 = \beta'_0$ (see Figure 5) or

$$-\hat{I} \cdot \hat{z} = \hat{D} \cdot \hat{z} = \cos \beta_0. \quad (5a)$$

The relationships between the orthogonal unit vectors associated with these coordinates $(\hat{I}, \beta'_0, \phi'; \hat{D}, \beta_0, \phi)$ are shown in Figure 5, and are given by

$$\begin{aligned} \hat{I} &= \hat{\beta}'_0 \times \hat{\phi}' \\ \hat{D} &= \hat{\beta}_0 \times \hat{\phi} \end{aligned} \quad (5b)$$

where $\hat{\phi}'$ and $\hat{\phi}$ are the unit vectors at the source and observation point, respectively.

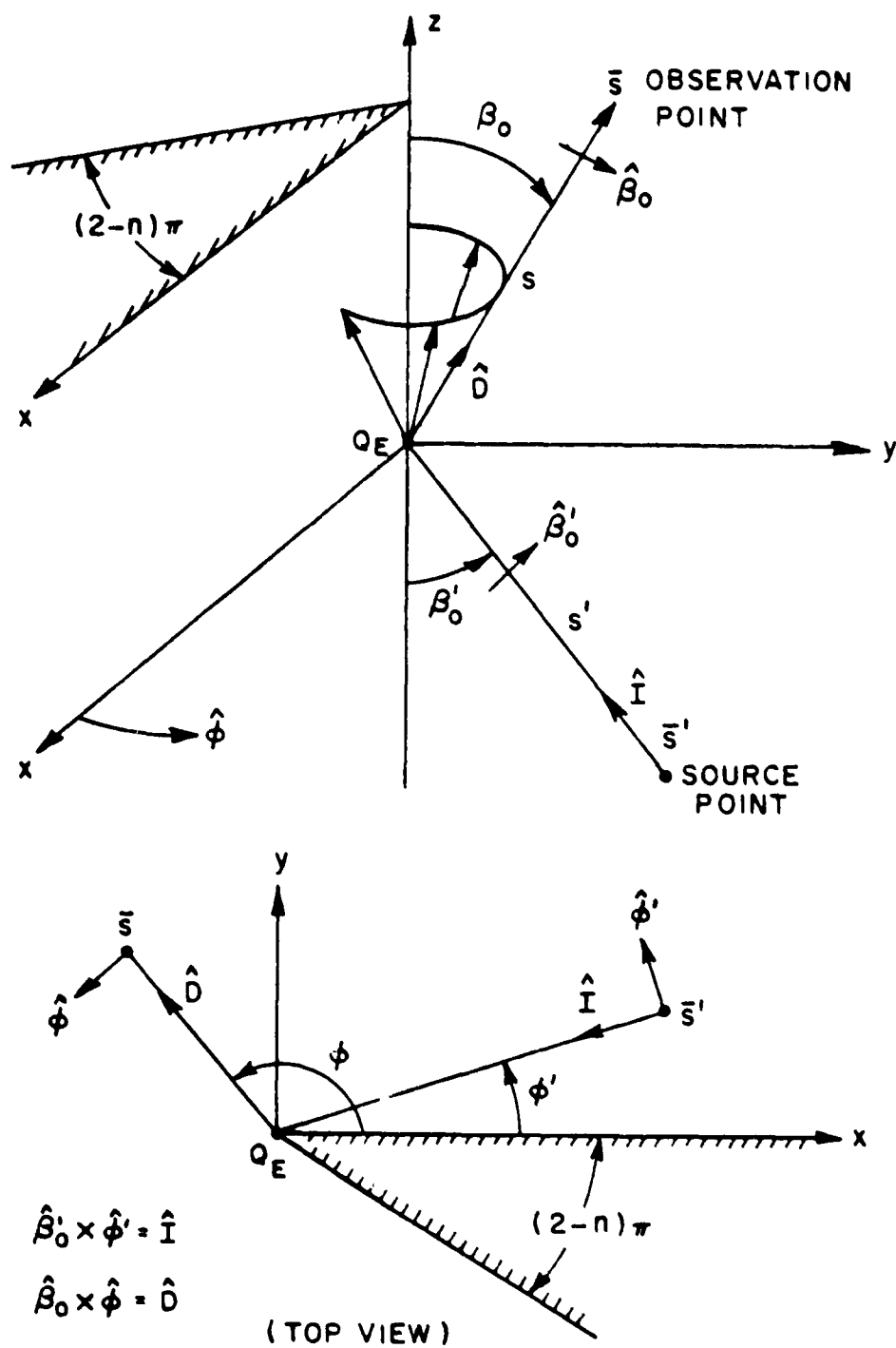


Figure 5. Geometry for three dimensional wedge diffraction.

The diffracted field is now given by

$$\vec{E}^d(s) \approx \vec{E}^i(Q_F) \cdot \vec{D} A(s) e^{-jks} \quad (6)$$

where s is the distance between the observation point and diffraction point, and \vec{D} is the dyadic diffraction coefficient, given by

$$\vec{D} = -\hat{R}_0' \hat{R}_0 D_s - \hat{\phi}' \hat{\phi} D_h$$

with

$$D_{s,h}(\phi, \phi'; R_0) = \frac{-e^{-j\pi/4}}{2n\sqrt{2\pi k} \sin R_0} \left\{ \cot\left(\frac{\pi+\beta^-}{2n}\right) F[kLa^+(\beta^-)] \right. \\ \left. + \cot\left(\frac{\pi-\beta^-}{2n}\right) F[kLa^-(\beta^-)] \mp \left[\cot\left(\frac{\pi+\beta^+}{2n}\right) F[kLa^+(\beta^+)] \right. \right. \\ \left. \left. + \cot\left(\frac{\pi-\beta^+}{2n}\right) F[kLa^-(\beta^+)] \right] \right\}. \quad (7)$$

Here the upper sign (-) corresponds to the soft boundary condition (s) and the lower sign (+) corresponds to the hard boundary condition (h). The angle variables are given by $\beta^\pm = \phi \pm \phi'$, where the $\phi - \phi'$ terms are associated with the incident field and the $\phi + \phi'$ terms are associated with the reflected field. The distance parameter L will be defined later. The function $F[x]$ is called the transition function and is given by

$$F[x] = 2j|\sqrt{x}| e^{jx} \int_{|\sqrt{x}|}^{\infty} e^{-j\tau^2} d\tau \quad (8)$$

The above diffraction coefficient can be shown to be related to the V_B function for a straight wedge by

$$D_{s,h}(\phi, \phi'; R_0) = [V_B(L, R^-) \mp V_B(L, R^+)] \frac{\sqrt{L} e^{ikL}}{\sin R_0} \quad (9)$$

where

$$V_B(L, R) = I_{-\pi}(L, R) + I_{+\pi}(L, R)$$

with

$$I_{\pm\pi}(L, R) = \frac{e^{-j(kL + \pi/4)}}{jn\sqrt{2\pi}} \sqrt{a} \cot\left(\frac{\pi \pm \beta}{2n}\right) e^{jkLa} \int_{\sqrt{kLa}}^{\infty} e^{-j\tau^2} d\tau \\ + [\text{higher order terms}]$$

The higher order terms are negligible for large kL . Here n is defined from the wedge angle $WA = (2-n)\pi$; also

$$a = a^{\pm} = 1 + \cos(\beta - 2n\pi N^{\pm}) \text{ and}$$

N^{\pm} is that positive or negative integer (or zero), which most nearly satisfies the equations

$$2n\pi N^{-} - \beta = -\pi \text{ for } I_{-\pi}$$

$$2n\pi N^{+} - \beta = +\pi \text{ for } I_{+\pi}.$$

For a straight wedge the quantity L is a distance parameter given in general by

$$L = \frac{s(\rho_e^i + s)\rho_1^i \rho_2^i \sin^2 \beta_0}{\rho_e^i (\rho_1^i + s)(\rho_2^i + s)} \quad (10)$$

where ρ_1^i, ρ_2^i are the principal radii of curvature of the incident wavefront at the point of diffraction, and ρ_e^i is the radius of curvature of the incident wavefront in the plane containing the incident ray and the edge. In matrix notation, the diffraction coefficient can be written as

$$\begin{bmatrix} E_{\parallel}^d(s) \\ E_{\perp}^d(s) \end{bmatrix} = \begin{bmatrix} -D_s & 0 \\ 0 & -D_h \end{bmatrix} \begin{bmatrix} E_{\parallel}^i(Q_E) \\ E_{\perp}^i(Q_E) \end{bmatrix} A(s) e^{-jks} \quad (11)$$

The D_s coefficient (minus sign between V_B terms) applies to the E -field component parallel to the edge and is derived from the canonical problem with the acoustically soft boundary condition

$$(\bar{E}|_{\text{wedge}}) = 0.$$

The D_h coefficient (plus sign between V_B terms) applies to the E -field component perpendicular to the edge, and is derived from the canonical problem with the acoustically hard boundary condition

$$\left(\frac{\partial \bar{E}}{\partial n} \middle|_{\text{wedge}} \right) = 0.$$

The quantity $A(s)$ is the ray divergence factor given in general by

$$A(s) = \sqrt{\frac{\rho}{s(\rho + s)}}$$

where for a straight wedge, $\rho = \rho_e^i$ is the radius of curvature of the incident wavefront in the plane containing the incident ray and the edge. For some specific problems the divergence factor is given by

$$A(s) = \begin{cases} \frac{1}{\sqrt{s}} & \text{plane, cylindrical and conical wave incident} \\ \frac{s'}{\sqrt{s(s'+s)}} & \text{spherical wave incident} \end{cases}$$

where s' is the distance from the source to the diffraction point and s is the distance from the diffraction point to the observation point.

C. Diffraction by a Curved Wedge

In this report the hull of the ship is to be modelled first by a finite elliptic cylinder. Since the top and the sides of the elliptic cylinder form a curved wedge at their junction, this configuration must also be considered. The curved wedge problem, which is illustrated in Figure 6, is again analyzed using the GTD technique developed by Kouyoumjian and Pathak². Again, the diffracted field from the curved wedge may be written in the form

$$\vec{E}^d(s) = \vec{E}^i(Q_E) \vec{D} \sqrt{\frac{\rho}{s(\rho+s)}} e^{-jks} \quad (12)$$

The parameter ρ is the distance between the caustic* at the edge and the second caustic of the diffracted ray. This is given by

$$\frac{1}{\rho} = \frac{1}{\rho_e^i} - \frac{\hat{n}_e \cdot (\hat{I} - \hat{s})}{a_e \sin^2 \theta_0} \quad (13)$$

where ρ_e^i , \hat{n}_e , a_e are defined below. The diffraction coefficients for the curved wedge are extended from those in Equation (7) to allow the diffracted field to be continuous at the incident and reflected shadow boundaries. This is accomplished by finding the appropriate distance parameter L in each of the transition functions that makes the total field continuous. The diffraction coefficient for the curved wedge is given by

*A caustic is a location where the rays converge and the geometrical optics field becomes infinite. It can be a point, a line or a surface.

$$D_{s,h}(\phi, \phi'; \beta_0) = \frac{e^{-j\pi/4}}{2n\sqrt{2\pi k} \sin \beta_0} \left\{ \frac{2 \sin \frac{\pi}{n} F[kL^i a(\beta^-)]}{\cos(\frac{\pi}{n}) - \cos(\frac{\beta^-}{n})} + \right. \\ \left. \left[\cot\left(\frac{\pi+\beta^+}{2n}\right) F[kL^{rn} a^+(\beta^+)] + \cot\left(\frac{\pi-\beta^+}{2n}\right) F[kL^{ro} a(\beta^+)] \right] \right\} \quad (14)$$

in which $a(\beta) = 2\cos^2(\beta/2)$ and $a^+(\beta) = 2\cos^2\left(\frac{2\pi n - \beta}{2}\right)$. The distance parameter associated with the incident field is given by

$$L^i = \frac{s(\rho_e^i + s)\rho_1^i \rho_2^i \sin^2 \beta_0}{\rho_e^i (\rho_1^i + s)(\rho_2^i + s)} \quad (15a)$$

The distance parameters L^{ro} associated with the reflecting surface denoted by o , or L^{rn} associated with the reflecting surface denoted by n , are given by (see Figure 7)

$$L^{ro, rn} = \frac{s(\rho_e^r + s)\rho_1^r \rho_2^r \sin^2 \beta_0}{\rho_e^r (\rho_1^r + s)(\rho_2^r + s)} \quad (15b)$$

The parameters ρ_1^i and ρ_2^i are the principal radii of curvature of the incident wavefront at the diffraction point Q_E . The parameter ρ_e^i is the radius of curvature of the incident wavefront at Q_E taken in the plane containing the incident ray and the tangent unit vector \hat{e} at the edge (see Figure 6). In the case of plane, cylindrical and conical waves, ρ_e^i is infinite and for the case of spherical waves $\rho_e^i = s^i$. The parameters ρ_1^r and ρ_2^r are the principal radii of curvature of the reflected wavefront at Q_E and may be found from Equation (4) for spherical wave incidence. Note that ρ_1^r , ρ_2^r , and ρ_e^r must be determined separately for the o and n surfaces, in that each surface has its own reflection properties. The parameter ρ_e^r is the radius of curvature of the reflected wavefront at Q_E taken in the plane containing the reflected ray and the tangent unit vector \hat{e} and is given by

$$\frac{1}{\rho_e^r} = \frac{1}{\rho_e^i} - \frac{2(\hat{n} \cdot \hat{n}_e)(\hat{I} \cdot \hat{n})}{a_e \sin^2 \beta_0} \quad (16)$$

where \hat{n} is the unit normal to the surface either o or n . The unit normal to the edge (\hat{n}_e) is directed away from the center of edge curvature, and $a_e > 0$ is the radius of curvature of the edge at Q_E .

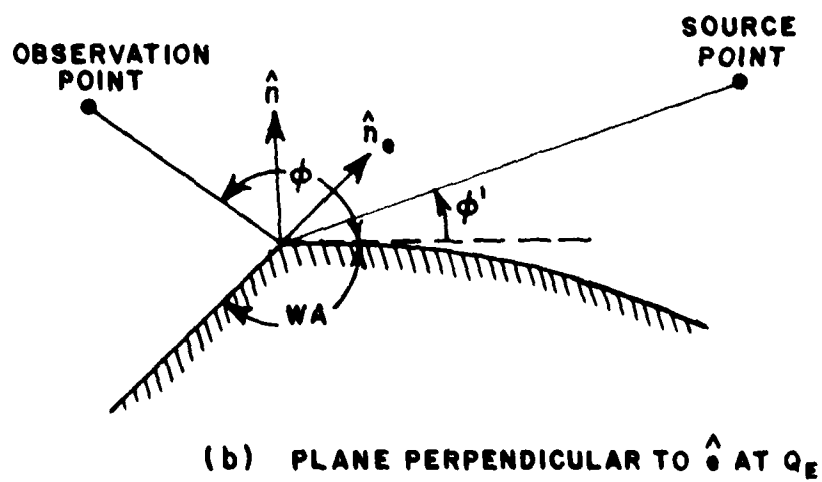
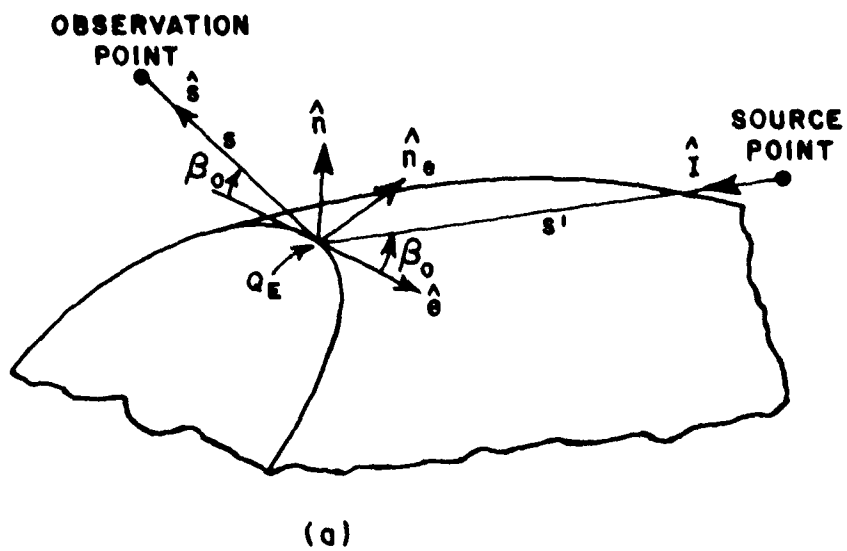


Figure 6. Geometry for three-dimensional curved wedge diffraction problem.

These three standard GTD solutions will form the basis of our calculations for the ship and ship-sea scattering contributions to the signatures detected by the radar.

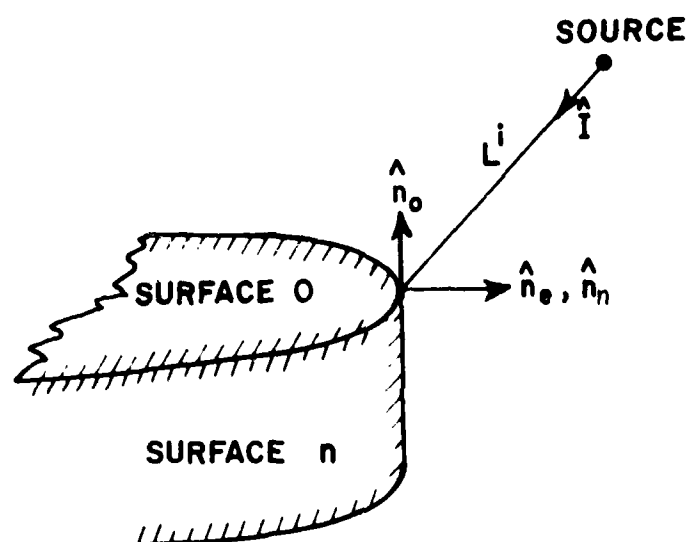


Figure 7. Definition of surfaces for wedge diffraction problem.

CHAPTER IV SEA SCATTERING CHARACTERISTICS

The scattering caused by the presence of the ocean surface should be calculated, in principle, from the actual state of the surface, i.e., from a specification of the height of the surface as a function of position and time. This would be both difficult and expensive. At the present time there is not available a sufficiently detailed description of the ocean surface to correctly formulate the microwave scattering problem. If there were such a description, the scattering problem still could not be solved exactly with present techniques. Finally, even such approximate techniques as physical optics would require a double integration over the extremely large surface area which can interact with the ship and the radar system. Thus in the ship-sea model developed here the actual scattering properties of the surface have been replaced by a statistically averaged bistatic radar cross-section of the ocean. In this chapter we discuss how the radar cross-section approach is implemented in the model, and what particular form of radar cross-section is used.

When using the radar cross-section to characterize the ocean scatter, care must be taken to duplicate, as far as possible, the statistical properties of the actual received signal. We have approached this problem by dividing up the total surface in the vicinity of the ship model into rectangular patches (see Figure 3). Now the scattering from each patch can be found from the radar cross-section per unit area of the patch, and its area. The size of the patches must be chosen small enough so that the angular dependence of the cross-section does not change greatly from patch to patch, but large enough so that the scattering from patch to patch is statistically independent. Because of the random character of ocean surface, the positions of the specular points which contribute to the forward cross-section are themselves random. Thus the minimum patch size should contain enough specular points (say more than 10) so that the signal from each patch has a statistically random character. We have not addressed the problem of determining the optimum patch size in this report, but believe, based on the consideration suggested above, that the dimension of the patch should be several times the wavelength of the significant ocean wave size, and that the angle subtended by the centers of adjacent patches should probably not be much more than 10 degrees.

To specify more formally the contribution from a single patch, consider the geometry of Figure 8. If a plane wave with electric

field $\vec{E}_0 \exp(-jkx \sin\theta_i + jkz \cos\theta_i)$ is incident on the patch $L \times L$ with angle of incidence θ_i , then the electric field in the scattering direction θ_s, ϕ_s at range R_s will be given, in our model, by

$$\vec{E}_s = \frac{|\vec{E}_0|}{R_s} \vec{P}(\theta_i, \theta_s, \phi_s) \sqrt{\frac{\sigma_0 L^2}{4\pi}} e^{-jkR_s + j\delta} \quad (17)$$

where $\vec{P}(\theta_i, \theta_s, \phi_s)$ is a unit vector which specifies the polarization state of the observed field, δ is a random phase angle with $-\pi < \delta < \pi$, and $\sigma_0(\theta_i, \theta_s, \phi_s)$ is the bistatic radar cross-section per unit area of the ocean. We consider next the specification of the quantity σ_0 .

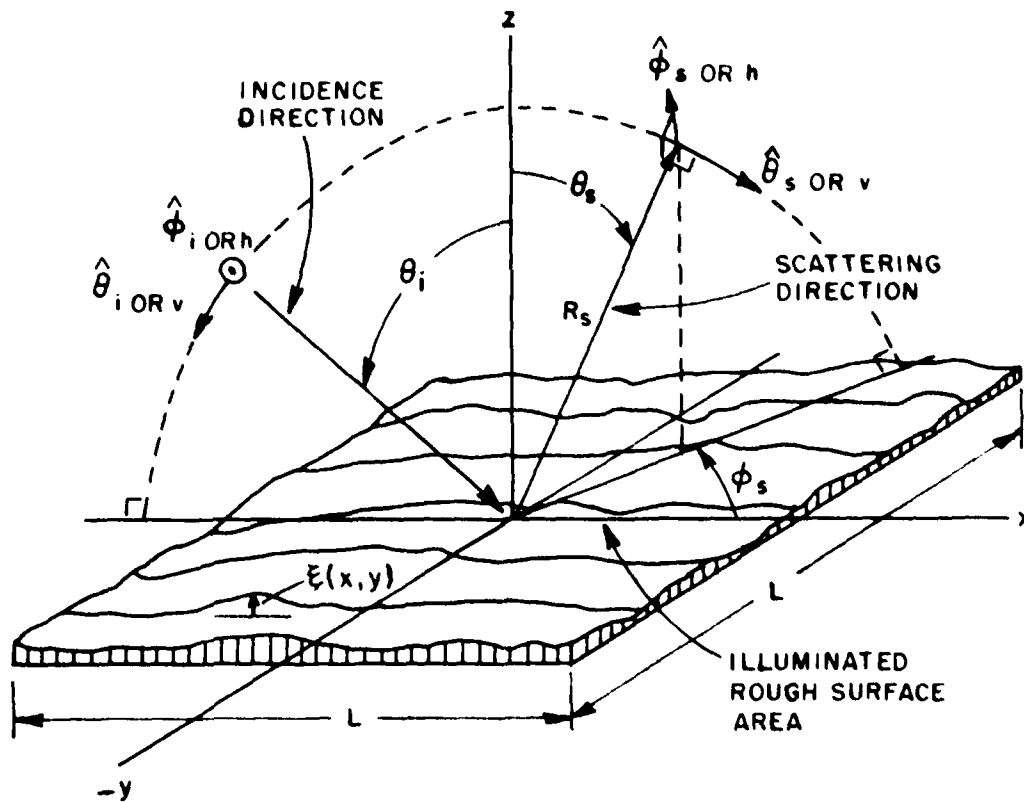


Figure 8. Surface arrangement and scattering geometry.

The general problem of scattering of electromagnetic waves by the ocean is an extremely difficult one. The forces of wind, gravity, surface tension, acceleration, etc. produce a spectrum of ocean waves of various heights, lengths and directions of motion which collectively behave as a random rough surface. The scattering from statistically rough surfaces has been studied extensively in recent years and two important special cases of rough surface scattering, distinguished by their relative roughness scales, and by the analytical methods used to obtain the scattered field, have particular relevance to ocean scatter. The currently accepted view of the scattering behavior of the ocean is contained in the so-called "composite" model. In this model, the scattering near the specular direction (i.e., near normal incidence for back-scatter) is controlled by the slope distribution of the large scale structure of the surface. This part of the scattered field is calculated by physical or geometrical optics, and provides an explanation not only for the near-normal incidence back-scattering cross-section but also for forward scatter (multipath) effects, and for the dependence of brightness temperature on wind-speed and polarization. For the back-scatter cross-section away from normal incidence, the scattering mechanism is the "Bragg" scatter from capillary and short wavelength components of the surface. This contribution is calculated by perturbation theory, and when utilized with the known spectrum of the ocean it explains the angular and polarization dependence of the radar cross-section, and the weak dependence of this cross-section on wind speed and electromagnetic wavelength. In this composite model, these two contributions to the scattered power are considered to be statistically independent, so that the total cross-section may be written as the sum,

$$\sigma_0(\theta_i, \theta_s, \phi_s) = \sigma_{os}(\theta_i, \theta_s, \phi_s) + \langle \sigma_{op}(\theta_i, \theta_s, \phi_s) \rangle \quad (18)$$

where σ_{os} is the specular component, and $\langle \sigma_{op} \rangle$ is the perturbation component averaged over the slope distribution of the large scale surface structure. These two components are considered separately as follows.

A. The Bragg Component; Slightly Rough Surface Scattering

The slightly rough surface is one having a scale of roughness whose r.m.s. roughness height, h , is much less than the electrical wavelength and whose surface slopes are small compared to unity. This slightly rough surface model, based on a perturbation calculation, was originally formulated by Rice⁸ in 1951 and was adapted to problems of radar scattering a few years later by Peake⁹. The perturbation or smallness parameters are the surface height - $\xi(x,y)$ and the surface slopes - ξ_x and ξ_y . By expanding the surface height

$\xi(x,y)$ in a Fourier Series, and applying the perturbation theory with the appropriate boundary conditions, one obtains the average scattering cross section per unit surface area for bistatic scattering:

$$\sigma_{\eta\epsilon}^0(\theta_i, \theta_s, \phi_s) = 16\pi k^4 \cos^2\theta_i \cos^2\theta_s |\alpha_{\eta\epsilon}|^2 S(k_x, k_y) \quad (19)$$

- where η and ϵ are the scattered and incident polarization states, respectively,
- k is the free space wave number ($2\pi/\lambda$) of the electromagnetic wave.
- The angles $\theta_i, \theta_s, \phi_s$ are illustrated in Figure 8. The incident plane is assumed to be aligned with the x-axis. For backscattering $\theta_i = \theta_s, \phi_s = \pi$.
- $\alpha_{\eta\epsilon}$ is the scattering matrix element for a homogeneous dielectric surface and is a function of the polarization states and material properties (see Appendix B).
- The function $S(k_x, k_y)$ is physically the surface height spectral density,
- k_x, k_y are the (mechanical) radian wave numbers in the x and y directions, respectively.

$$k_x = k(\sin\theta_s \cos\phi_s - \sin\theta_i), \quad k_y = k \sin\theta_s \sin\phi_s$$

The density $S(k_x, k_y)$ is defined as

$$S(k_x, k_y) = \frac{1}{(2\pi)^2} \iint_{-\infty}^{\infty} \langle \xi(x,y) \xi(x',y') \rangle e^{-jk_x \tau_x} e^{-jk_y \tau_y} d\tau_x d\tau_y$$

where $\tau_x = x - x'$ and $\tau_y = y - y'$,

or

$$S(k_x, k_y) = \frac{h^2}{(2\pi)^2} \iint_{-\infty}^{\infty} R(\tau_x, \tau_y) e^{-jk_x \tau_x} e^{-jk_y \tau_y} d\tau_x d\tau_y$$

where $R(\tau_x, \tau_y)$ is the surface height correlation function. Since the surface roughness is assumed to be isotropic, the height correlation function $R(\tau_x, \tau_y)$ is a function only of the separation

r , between the surface points x, y and x', y' , (i.e., $r = \sqrt{(x-x')^2 + (y-y')^2} = \sqrt{\tau_x^2 + \tau_y^2}$). Hence one can define $\rho(r) \equiv R(\tau_x, \tau_y)$ to be the surface height correlation function. Here h^2 is the surface mean square height and is given by the relation

$$h^2 = \langle \xi^2(x, y) \rangle.$$

Thus the scattering cross section is proportional to the power spectral density of the surface height. The height spectrum of the ocean surface, $S(k_x, k_y)$, has been reviewed by Phillips¹⁰, who found that in the equilibrium range, the spectrum has the convenient approximate form

$$S(k_x, k_y) = S(k_0) = \begin{cases} 0 & k < k_1 \\ Bk_0^{-4} & k_1 < k < k_c \end{cases} \quad (20)$$

where $k_0 = \sqrt{k_x^2 + k_y^2}$,

B is the Phillips constant, $B \approx 0.006$,

$$k_1 = g/\mu_0^2,$$

$$k_c = 3.6 \text{ cm}^{-1},$$

g is the acceleration of gravity (9.8 m/sec^2) and

μ_0 is the wind velocity (m/sec).

The lower cut-off k_1 represents the gravity waves with phase velocity equal to the wind velocity. The upper cut-off k_c represents the capillary waves of minimum phase velocity. For wave numbers greater than k_c , the exact form of $S(k_0)$ is not well known, and is very sensitive to local wind speed. Thus at present, the use of the perturbation theory is limited to electromagnetic wavelengths greater than about 4 cm. Physically, the Phillips spectrum implies that the wind speed does not affect the shape of the spectrum in the equilibrium range. As the wind speed increases it merely drives the cut-off (k_1) to smaller wave numbers. The upper cut-off, k_c , occurs because viscous dissipation quickly damps out larger wave numbers. Figure 9 shows measurements (of Valenzuela et al.¹¹) of the spectrum of the sea surface $S(k)$ computed from measured back-scattering cross-section at UHF, L, and C band. It is apparent that the Phillips spectrum is an excellent approximation to the actual spectrum in the wave number region where the perturbation theory is valid, and that the cross-sections based on Equation (19) and (20) are in good agreement with measured results.

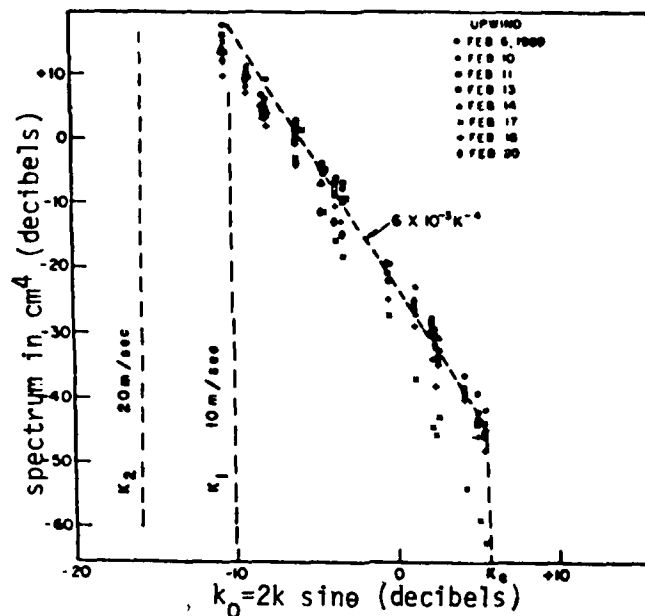


Figure 9. Spectra inferred from vertical radar cross-section data by means of the composite model, after Valenzuela et al. The line indicates the Phillips spectrum for wind speeds of 10 and 20 ms.

B. The Specular Component; Very Rough Surface Scattering

The specular component σ_{OS} is calculated from the "very rough surface" scattering model. The very rough class of surfaces are those having a large scale roughness such that the r.m.s. roughness height, h , is larger than the electric wavelength and the local surface radii of curvature are also greater than this wavelength. In the past, two different techniques have been used to calculate the fields scattered by such surfaces, viz. the Physical Optics approach, and the Geometrical Optics or stationary phase approach. If these are used correctly, they lead to the same result.

The Physical Optics approach, which employs a physical optics integral expression for the scattered field, is probably the most mathematically thorough and exact approach. Among others, Semenov¹², Kodis¹³ and Barrick¹⁴ have addressed the problem of scattering from a very rough surface of homogeneous material, using a vector formulation which accounts for polarization. Since this method probably yields the least physical insight into the scattering mechanism and is computationally time consuming, it will not be used here.

The Geometrical Optics approach, originated by Muhleman¹⁵, subdivides the rough surface into a grid of smaller flat sub-areas each having the same projected area in the x-y plane. Each sub-area reflects the incident power specularly, and the direction of reflection is determined by the direction of the local normal (i.e.,

the direction bisecting the angle between the incidence and scattering directions). Hence the amount of power scattered into a given direction is directly proportional to the number of sub-areas whose normals are pointed in the proper direction, divided by the total number of sub-areas. This quantity is the probability density function for the surface normal. An identical result for the scattering cross section may also be obtained from a slightly different point of view, in which the incidence and scattering directions are specified, and the specular reflection points on the surface located. From elementary geometrical optics considerations, the scattering cross section of a single specular point is π times the principal radii of curvature at that point. For multiple specular points, Kodis¹³, starting with an exact integral equation for the fields and evaluating it asymptotically by the method of stationary phase, has shown that the average scattered power is proportional to the average number of specular points on the surface times the average radii of curvature at these points.

From these two analyses, Barrick¹ has presented the equation for the average scattering cross section per unit area of a very rough surface of homogeneous material. This is given by

$$\sigma_{ne}^0 = \pi n_A \langle |r_1 r_2| \rangle |R_{ne}(\nu)|^2 \quad (21)$$

where n_A = average number of specular points per unit area,

$\langle |r_1 r_2| \rangle$ = average absolute value of product of principal radii of curvature at specular point,

$R_{ne}(\nu)$ = Fresnel reflection coefficient for incident polarization state e and scattered polarization state n . These quantities are given in Appendix C.

ν = local angle of incidence at specular point (half the angle between incidence and scattering directions) with $\cos \nu = \sqrt{\frac{1}{2}(1 - \sin \theta_i \sin \theta_s \cos \phi_s + \cos \theta_i \cos \theta_s)}$, see Figure 10.

After determining, from the statistical properties of the surface, the quantities n_A and $\langle |r_1 r_2| \rangle$, Barrick obtained, for a general surface,

$$\sigma_{ne}^0 = \pi \sec^4 B p(\xi_{xsp}, \xi_{ysp}) |R_{ne}(\nu)|^2 \quad (22)$$

where $p(\xi_{xsp}, \xi_{ysp})$ is the joint probability density function for the surface slopes in both x, y directions at the specular point with ξ_{xsp} and ξ_{ysp} defined as $(\partial \xi(x, y))/\partial x$ and $(\partial \xi(x, y))/\partial y$ at the specular point. B is the angle between z axis (mean surface normal) and the local surface normal with $\cos B = (\cos \theta_i + \cos \theta_s)/2 \cos \nu$ (see Figure 10). Since the probability density function for the surface

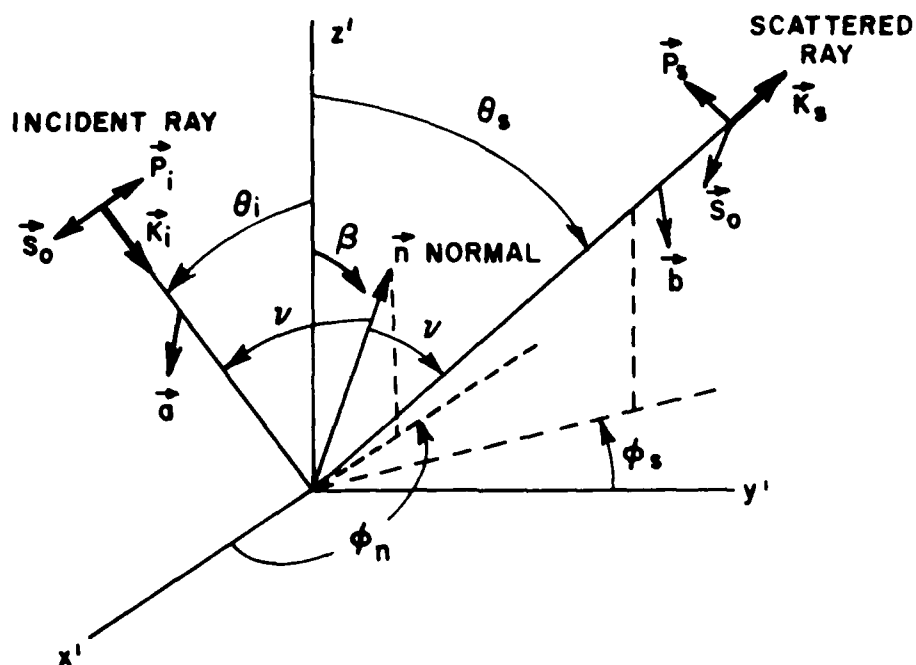


Figure 10. Geometry of bistatic cross-section.

slopes in the x and y directions is simply related to the probability density function for the local surface normal, one can show that, if the slope distribution is independent of azimuth angle ϕ_n , then

$$\sigma_{ne}^0 = \pi \sec \beta P(\beta) |R_{ne}(\nu)|^2 \quad (23)$$

where $P(\beta)d\Omega$ is now the probability that the surface normal lies in a small cone of solid angle $d\Omega$ in the direction \vec{n} (see Figure 10). The difference factor $\sec \beta$ between Equations (22) and (23) is due to the Jacobian of the transformation between β , ϕ_n and ξ_{xsp} , ξ_{ysp} . The probability density function $P(\beta)$ for the ocean surface depends on a number of factors, but for the purpose of this report it is assumed to have the simple isotropic form (very similar to the cross-wind form of the Cox-Munk¹⁶ distribution):

$$P(\beta) = \frac{\cos \beta}{\pi t^2} \exp[-\tan^2 \beta / t^2 (1+t^2)] \quad (24)$$

where t^2 is the mean square surface slope. For the sea surface which possesses the Phillips spectrum, the effective mean surface slope is

$$t^2 = B \log(k_2/k_1) \quad (25)$$

Here k_1 and k_2 are the effective lower and upper limits of the ocean spectrum, respectively. The lower wave number limit, in the Phillips spectrum, is given in Equation (20). The upper limit is determined by the condition that there be a smooth transition in the back-scattering cross section between the results of Equations (23) and (19). The expression given here is a convenient empirical result:

$$k_2 = \sqrt{k_1^2 + \frac{2}{(3.5\lambda)^2 B}} \quad (26)$$

Both shadowing and multiple scattering between different surface points are neglected in the above theories for the very rough surface; these limitations are not expected to be serious as long as the slopes are not too precipitous and near-grazing angles are avoided. If it is desired to account for the shadowing correction, there is a large literature (see, for example, reference 17) devoted to the problem.

C. The Composite Cross-Section

The "composite" model for the surface views the small scale structure of the surface (which produces the Bragg scatter component) to be superimposed on the large scale structure. Thus the perturbation component of the scattered field is viewed as a local scattering phenomenon occurring on a tilted surface which must be averaged over the large scale slope distribution of the surface. The general procedure has been discussed in detail by Valenzuela, [25] but for the purpose of this report it is more convenient to consider expressions for the bistatic and the back-scattering cross-section separately.

1. Backscatter

For back-scatter, ($\theta_i = \theta_s$; $\phi = \pi$) both the specular and the Bragg components of scatter will be significant. When the averaging of the Bragg component over the slope distribution is carried out, the resulting cross-section can be written in the form

$$\sigma_{\eta\epsilon}^0(\theta_i) = \pi \sec \theta_i |R_{\eta\epsilon}(0)|^2 P(\theta_i) + 16\pi k^4 \cos^4 \theta_i |\alpha'_{\eta\epsilon}|^2 S(2k \sin \theta_i, 0) \quad (27)$$

where we have chosen the specific polarization states h (horizontal) and v (vertical) to represent the incident polarization (η), and

that polarization component (ϵ) of the scattered field accepted by the receiver (thus $\alpha_{\eta\nu}$ represents a transmitter with horizontal polarization and a receiver with vertical polarization). Clearly, for back-scatter, the Fresnel coefficients $|R_{hh}(0)|$ and $|R_{vv}(0)|$ are equal, while $R_{hv} = R_{vh} = 0$. The parameter $|\alpha'_{\eta\epsilon}|^2$ includes the effect of the average over the surface slopes, with direct polarized form

$$|\alpha'_{\eta\eta}|^2 = |\alpha_{\eta\eta}|^2 \cos^2 \gamma + |\alpha_{\epsilon\epsilon}|^2 \sin^2 \gamma \quad (28a)$$

where $\eta = h$ or v , $\epsilon = v$ or h , $\eta \neq \epsilon$ for $\theta_i = \theta_s$ and $\phi_s = \pi$,

and cross polarized form

$$|\alpha'_{\eta\epsilon}|^2 = |\alpha_{\eta\epsilon}|^2 \cos^2 \gamma + |\alpha_{\epsilon\eta}|^2 \sin^2 \gamma \quad (28b)$$

where $\eta = h$ or v , $\epsilon = v$ or h , $\eta \neq \epsilon$ for $\theta_i = \theta_s$ and $\phi_s = \pi$.

The factor $\sin^2 \gamma$ represents the effect of averaging over the surface slopes and can be approximated by the convenient empirical form

$$\sin^2 \gamma = \frac{t^2}{2} \frac{(t^2 + \sin^2 \theta_i)^2}{(t^2 + \sin^2 \theta_i)^2} \quad (29)$$

where t^2 is the r.m.s. surface slope given by Equation (25). The coefficients $\alpha_{\eta\epsilon}$ are given in Appendix B. Thus the back-scattered clutter contribution to the signature from each patch is calculated from Equations (17), (27), (28) and (29). Note that for each patch in the model, the local scattering angles θ_i , θ_s , ϕ_s , etc. must be computed from the position of the radar and the position of the patch center.

2. Bistatic scatter

Although in general the bistatic cross-section should contain both the perturbation and specular components of the cross-section, it is found that in the forward scatter direction (for $\phi_s < \pi/2$) the total cross-section is dominated by the specular part. Thus in the ship-sea model, the ship-sea interaction term, which involves a forward scatter contribution from the surface, is found from the specular component alone (Equation (23)). Again, however, the local scattering angles θ_i , θ_s and ϕ_s which give β and ν (and the appropriate polarization states) must be found from the position of the radar, the patch center, and the specular point on the ship structure.

CHAPTER V

DOUBLE-REFLECTION SIGNATURE FROM THE SHIP SEA INTERACTIONS

A. Numerical Search Technique for Points of Reflections

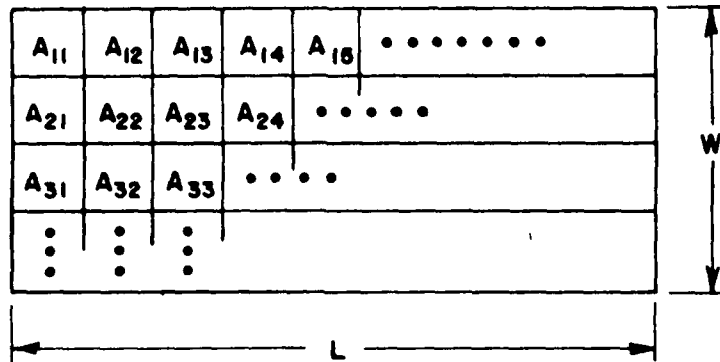
In this section the techniques for calculating the ship-sea interaction term are considered in detail. In the flat patch model for the sea surface described in Chapter IV, the scattering from each patch is calculated in terms of the area of the patch and its bistatic radar cross-section as if the entire scattered field emanated from a single reference point in the patch. Once the "reflecting" properties of the patch of ocean are known, one may return to the problem of calculating the double-bounce contribution of a particular patch. From any one of the sub-areas to the receiver via the reflection from the elliptical cylinder, there must exist one reflection point on the cylinder except when the receiver is in the shadow region of the cylinder. To find this reflection point, the laws of reflection, as defined by Equations (2a) and (2b) must be satisfied. When these laws are applied in a systematic manner, it is found⁸ that the position of the reflection point can be recovered from a single unknown parameter α (defined in the reference given) which satisfies a sixth order polynomial,

$$C_6\alpha^6 + C_5\alpha^5 + C_4\alpha^4 + C_3\alpha^3 + C_2\alpha^2 + C_1\alpha + C_0 = 0. \quad (20)$$

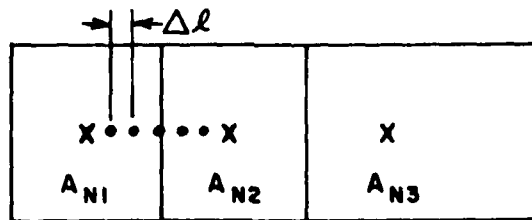
The coefficients C_0, C_1 , etc. are functions of the "source" location (i.e., the center of the patch), the receiver location, and the cylinder parameters. Since the derivation of this polynomial is quite a laborious process, and it has been derived in the reference given above, it will not be reproduced.

The polynomial technique is very time consuming if it must be carried out for every sub-area at each point of the trajectory. Hence it is used only for initial acquisition of the reflection point for the first sub-area of the Nth row (A_{N1}) as shown in Figure 11. This reflection point is then tracked by a very fast numerical search technique through many small increments (width = Δl) to the new reflection point for sub-area A_{N2} . This numerical search technique is thereafter applied to find all the reflection points for the sub-areas in the same row (sub-area A_{N3}, A_{N4} , etc.), and the procedure is then repeated for each row.

The polynomial method can be considered as an exact solution (except for a numerical truncation error). In the numerical search technique, a new reflection point is found from the previously determined point; therefore this approach can have an accumulation



(a)



ENLARGED VIEW OF THE N^{th} ROW

(b)

Figure 11. Sub-divided patches of the illuminated sea surface.

of errors. In order to control this situation, an error bound is defined such that if it is exceeded by the accumulated error, the number of increments is increased (Δl being reduced) until the error bound is satisfied. The numerical search technique is briefly discussed below. One needs first to define (see Figure 3) position vectors \vec{s} , \vec{o} , and \vec{r} , where the vector \vec{s} is the position of the center of sub-area, vector \vec{o} is the position of the observation point (which is fixed for any instantaneous antenna location) and vector \vec{r} is the position of the reflection point on the cylinder. Thus the vectors

$$\vec{s} = x_s \hat{x} + y_s \hat{y}$$

$$\vec{o} = x_o \hat{x} + y_o \hat{y} + z_o \hat{z}$$

$$\vec{r} = x_r \hat{x} + y_r \hat{y} + z_r \hat{z}$$

define the corresponding coordinates x_s, y_s , etc.

A parameter v is introduced to define the reflection point on the elliptic cylinder such that

$$\cos v = \frac{x_r}{a}, \quad \sin v = \frac{y_r}{b}$$

where a, b are the semi-major and semi-minor axes of the ellipse. Thus,

$$\vec{r} = a \cos v \hat{x} + b \sin v \hat{y} + z_r \hat{z}.$$

Now Equations (2a) and (2b) can be combined to form:

$$(\vec{n} \cdot \vec{I})(\vec{n} \times \vec{R}) + (\vec{n} \times \vec{I})(\vec{n} \cdot \vec{R}) = 0 \quad (31)$$

where $\vec{n} = n_x \hat{x} + n_y \hat{y} = b \cos v \hat{x} + a \sin v \hat{y}$ a normal vector

$$(32a)$$

$$\begin{aligned} \vec{I} &= I_x \hat{x} + I_y \hat{y} + I_z \hat{z} = \vec{r} - \vec{s} \\ &= (a \cos v - x_s) \hat{x} + (b \sin v - y_s) \hat{y} + z_r \hat{z} \text{ an incident vector} \end{aligned}$$

$$(32b)$$

$$\begin{aligned} \vec{R} &= R_x \hat{x} + R_y \hat{y} + R_z \hat{z} = \vec{0} - \vec{r} \\ &= (x_0 - a \cos v) \hat{x} + (y_0 - b \sin v) \hat{y} + (z_0 - z_r) \hat{z} \text{ a reflection vector} \end{aligned}$$

$$(32c)$$

After performing the dot and cross products, Equation (31) can be separated into two equations:

$$f(v, x_s, y_s) = (n_x I_x + n_y I_y)(n_x R_y - n_y R_x) + (n_x R_x + n_y R_y)(n_x I_y - n_y I_x) = 0 \quad (33a)$$

$$g(v, x_s, y_s, z_r) = (n_x I_x + n_y I_y) R_z + (n_x R_x + n_y R_y) I_z = 0. \quad (33b)$$

By substituting Equations (32b) and (32c) into Equation (33b), one finds that

$$z_r = \frac{(n_x I_x + n_y I_y) z_0}{(n_x I_x + n_y I_y) - (n_x R_x + n_y R_y)} \quad (34)$$

which is a function of v , x_s and y_s . For Equation (33a), one can apply the Taylor Series expansion which says that the equation for the new reflection point ($f_{j+1}=0$) is given in terms of the previous point (f_j) by

$$f_{j+1} = f_j + \delta f_j = 0$$

$$\text{where } \delta f_j \cong \frac{\partial f_j}{\partial v} \delta v + \frac{\partial f_j}{\partial x_s} \delta x_s + \frac{\partial f_j}{\partial y_s} \delta y_s$$

with $\frac{\partial f_j}{\partial x_s}$ indicating the value of $\frac{\partial f}{\partial x_s}$ evaluated at the j th point.

Hence,

$$\delta v = - \frac{f_j + (\partial f_j / \partial x_s) \delta x_s + (\partial f_j / \partial y_s) \delta y_s}{\partial f_j / \partial v} \quad (35)$$

which is a function of the old reflection point (v, x_s, y_s) and the incremental distances ($\delta x_s, \delta y_s$). The new reflection point in the x - y plane is now defined by $v_{j+1} = v_j + \delta v$ and can be substituted along with the new source location ($x_s + \delta x_s, y_s + \delta y_s$) into Equation (34) to yield the new reflection point in the z -coordinate. After the point ($j+1$) has been determined it can be substituted into Equations (35) and (34) again to find the next new point ($j+2$). This process continues until it reaches the center of the adjacent sub-area from which an additional reflected field is then calculated.

B. Reflection from the Elliptical Cylinder

Once the field scattered from the center of each sub-area has been calculated and the corresponding reflection point on the cylinder located, the reflected field incident on the receiver is readily computed using the geometry illustrated in Figure 12. The scattered field for each sub-area, as described in Chapter IV, is treated as the field incident on the cylinder ($E^i(Q_R)$). The reflected field is given by Equation (1),

$$\vec{E}^r(s) = \vec{E}^i(Q_R) \cdot \vec{R} \sqrt{\frac{\rho_1^r \rho_2^r}{(\rho_1^r + s)(\rho_2^r + s)}} e^{-jks}$$

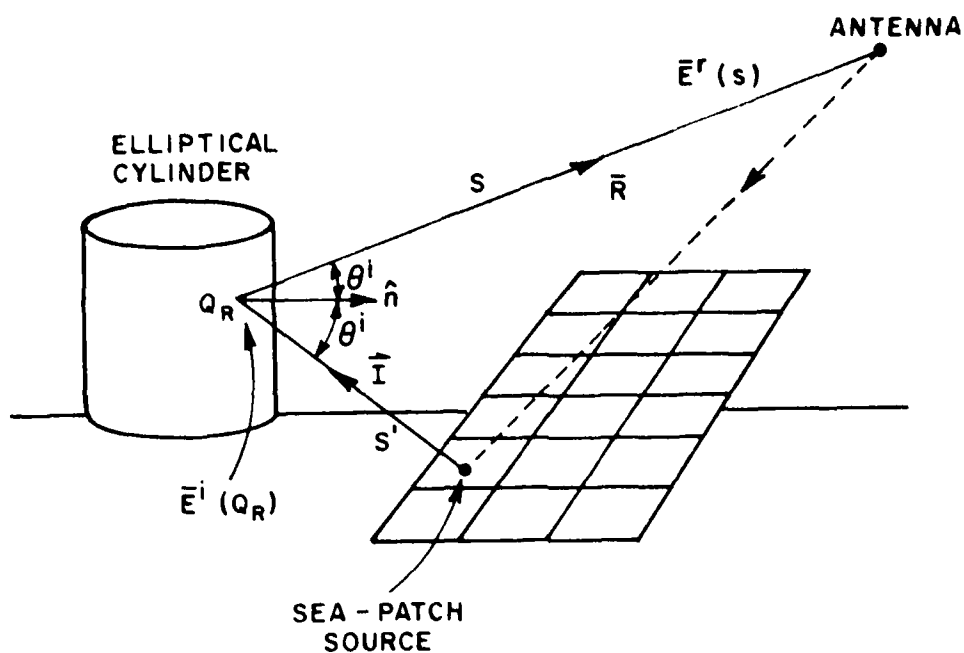


Figure 12. Geometry for field reflected from elliptical cylinder.

In order to calculate the principal radii of curvature of the reflected wavefront ρ_1 and ρ_2 , the values of R_1 and R_2 , the principal radii of curvature of the elliptic cylinder, are needed. In this case

$$R_2 = \infty, \quad R_1 = \frac{(b^2 \cos^2 v + a^2 \sin^2 v)^{3/2}}{ab}$$

Using the above expressions and Equation (4), one finds that

$$\frac{1}{\rho_1} = \frac{1}{s'} + \frac{2 \sin^2 \theta_i}{R_1 \cos \theta_i} \quad \text{and} \quad \frac{1}{\rho_2} = \frac{1}{s'}$$

All the parameters have been defined before in Chapter III. The dyadic reflection coefficient is given by

$$\bar{R} = [\hat{e}_n^i \hat{e}_n^r - \hat{e}_t^i \hat{e}_t^r]$$

and can be calculated in the following manner (see Figure 13).

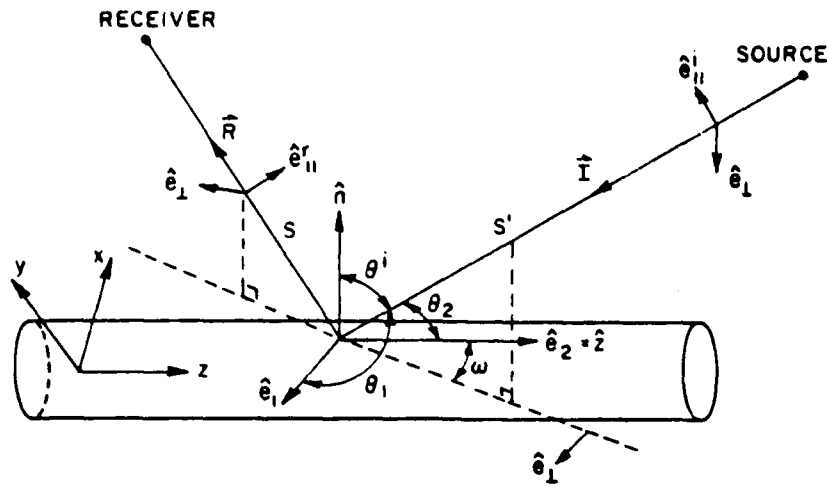


Figure 13. Reflection coordinate transformation system on the elliptical cylinder.

The incident vector \hat{I} in Figure 13 can be transformed to the orthogonal coordinate system \hat{n} , \hat{e}_1 , \hat{e}_2 as

$$\hat{I} = -\cos\theta^i \hat{n} - \sin\theta^i \cos\omega \hat{e}_2 - \sin\theta^i \sin\omega \hat{e}_1 \quad (36)$$

where ω is the angle between \hat{e}_2 and the projection of \hat{I} onto the plane containing \hat{e}_1 and \hat{e}_2 such that

$$\hat{I} \cdot \hat{e}_2 = -\sin\theta^i \cos\omega.$$

Since it is also true that $\hat{I} \cdot \hat{e}_2 = -\cos\theta_2$, we have

$$\cos\omega = \frac{\cos\theta_2}{\sin\theta^i}.$$

The unit vector \hat{e}_1 is found by the orthogonal relationship:

$$\hat{e}_1 = \hat{e}_2 \times \frac{|\vec{n}|}{|\vec{n}|} = \hat{z} \times \frac{\vec{n}}{|\vec{n}|}$$

where \vec{n} can be obtained from Equation (32a). Hence

$$\hat{e}_1 = e_{1x} \hat{x} + e_{1y} \hat{y}$$

with

$$e_{1x} = -\frac{a \sin v}{\sqrt{b^2 \cos^2 v + a^2 \sin^2 v}} \quad \text{and} \quad e_{1y} = \frac{b \cos v}{\sqrt{b^2 \cos^2 v + a^2 \sin^2 v}}$$

From Figure 13 one can easily transform the vectors used in the dyadic reflection coefficient into the x-y-z coordinate system,

$$\begin{aligned} \hat{e}_\perp &= -\sin \omega \hat{e}_2 + \cos \omega \hat{e}_1 \\ &= -\sin \omega \hat{z} + \cos \omega \cdot e_{1x} \hat{x} + \cos \omega \cdot e_{1y} \hat{y} \end{aligned} \quad (37a)$$

and

$$\hat{e}_\parallel^i = \hat{i} \times \hat{e}_\perp \quad (37b)$$

$$\hat{e}_\parallel^r = \hat{r} \times \hat{e}_\perp \quad (37c)$$

Due to the principle of reciprocity, the ray which travels in the opposite direction to that shown in Figure 12 will produce exactly the same field at the receiver terminals; therefore the doubly reflected field calculated for the ray path depicted in this figure should be doubled to give the total field.

C. Test Cases: The Elliptic Cylinder; The Reflection Points

Before showing the results for the doubly reflected field, it is helpful to ensure that the GTD solution for the reflected field from an elliptic cylinder is correctly calculated. Consider the test case with an electric current moment placed close to an elliptic cylinder, as shown in Figure 14, with the reflected field pattern calculated in accordance with Equation (1). The result is compared against that obtained by Marhefka¹⁸, and excellent agreement (see Figure 15) is achieved. Marhefka's solution which is also based on the GTD technique has itself been validated by a moment method solution.

The results of the computer program for obtaining the reflection points on the elliptic cylinder have also been verified. As an example, for the case of broadside incidence on the cylinder, as shown in Figure 16, the locations of the reflection points on the cylinder versus the sub-area positions are illustrated in Figures 17 and 18. Figure 17 shows the reflection points in the x-y plane as measured by the parameter v (the elliptic parameter v is related to angle ϕ by $v = \arctan[(A/B)\tan\phi]$), and Figure 18 shows the reflection points in the z-plane as measured by the height z_r . For the case of off-broadside incidence (45°), shown in Figure 19, the reflection points versus the positions of the sub-area are illustrated in Figures 20 and 21. The curves of position generated for broadside incidence are symmetric with respect to the center sub-area

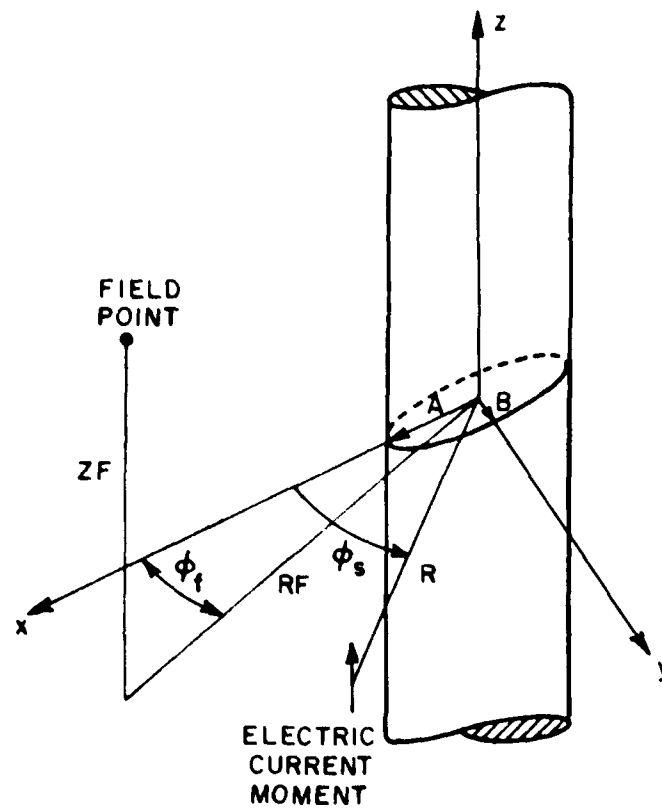


Figure 14. Configuration for the reflected field pattern measurement. The source is located in the x - y plane.

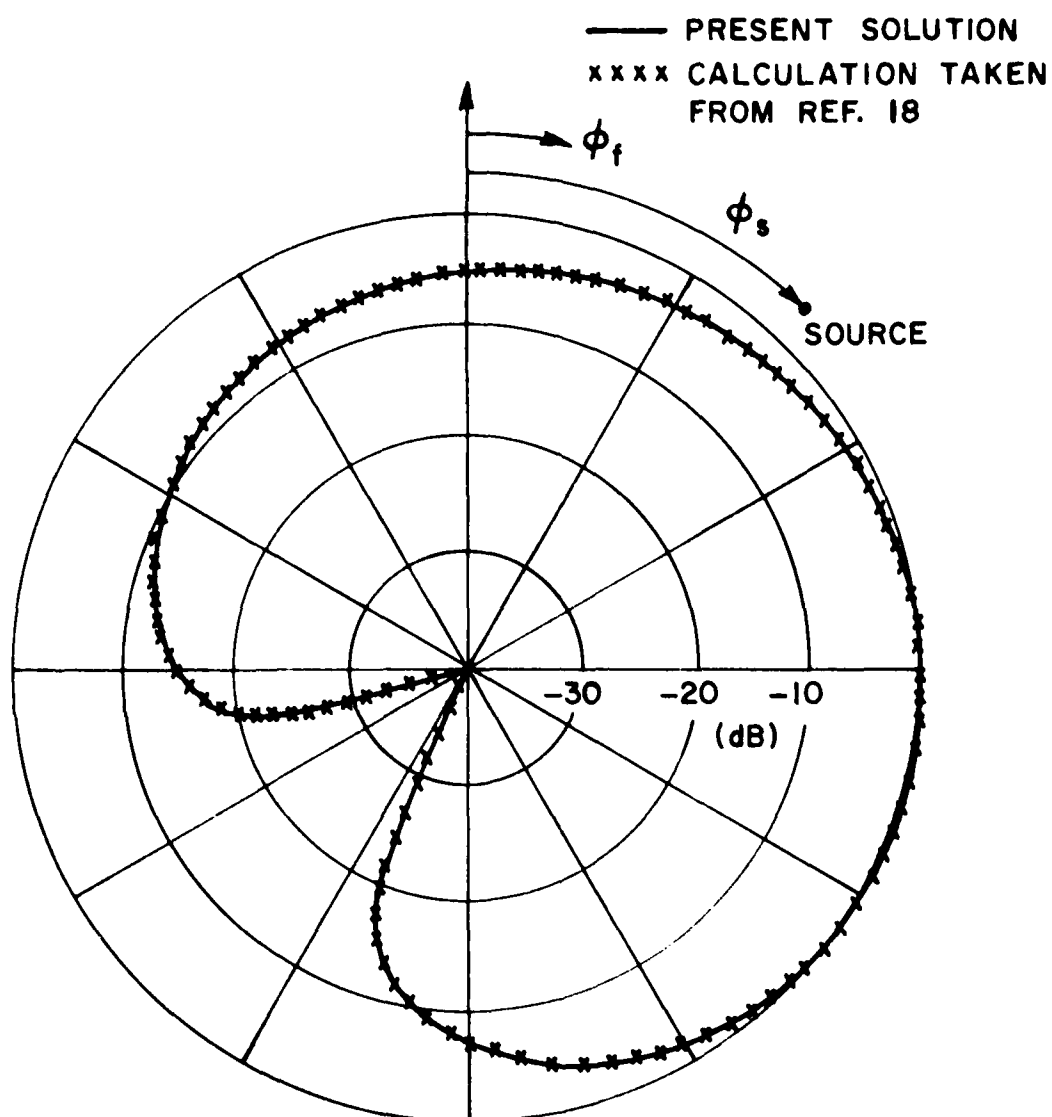


Figure 15. Reflected field pattern for the geometrical configuration shown in Figure 14 with $A=2\lambda$, $B=1\lambda$, $R=4\lambda$, $\phi_s=45^\circ$, $RF=200\lambda$, $ZF=200\lambda$.

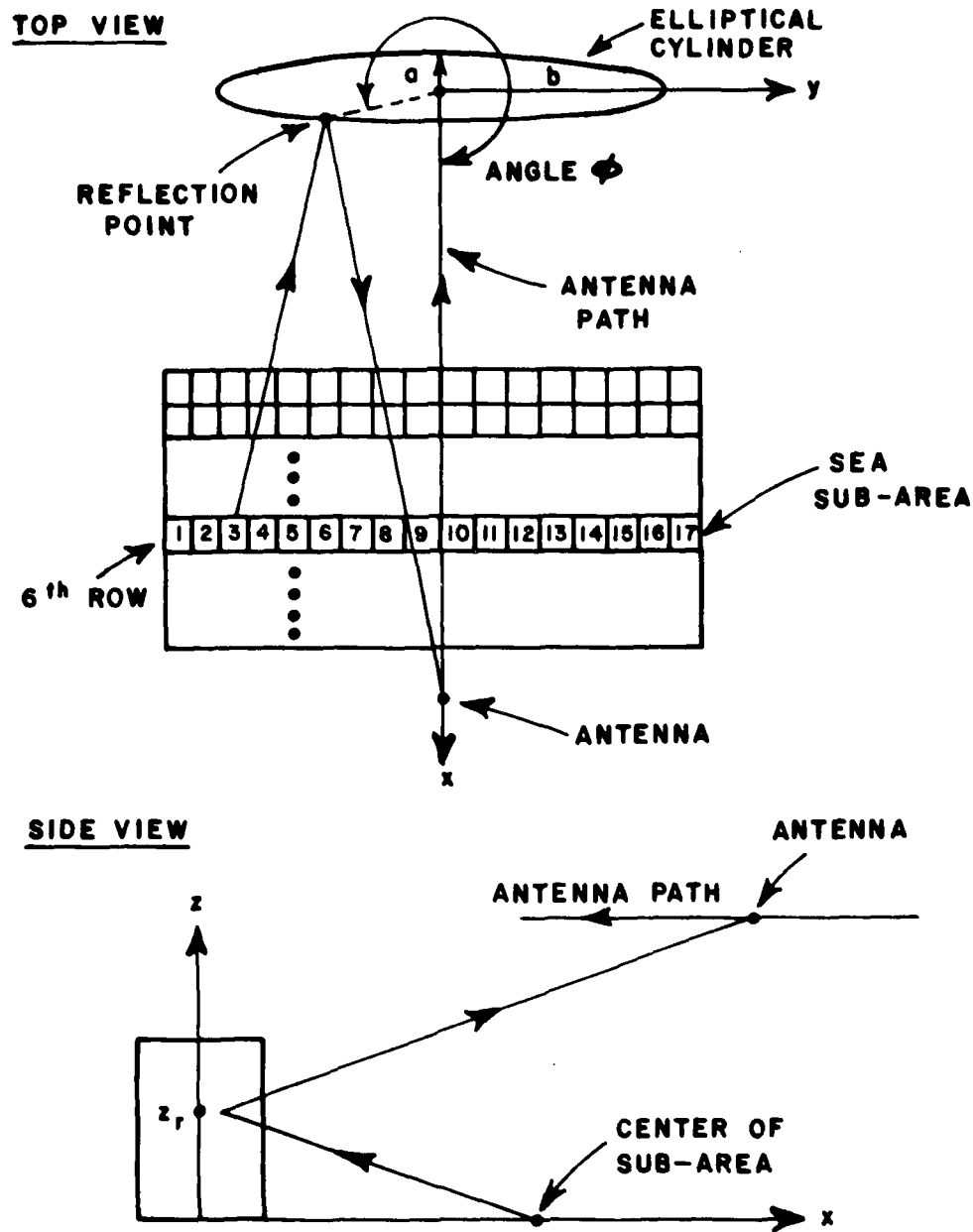


Figure 16. Characteristic views of elliptical cylinder and position matrix for broadside incidence. The antenna is instantaneously fixed at location ($x=55.2$, $y=0$, $z=40.5$, and $a=3$, $b=30$; arbitrary distance units).

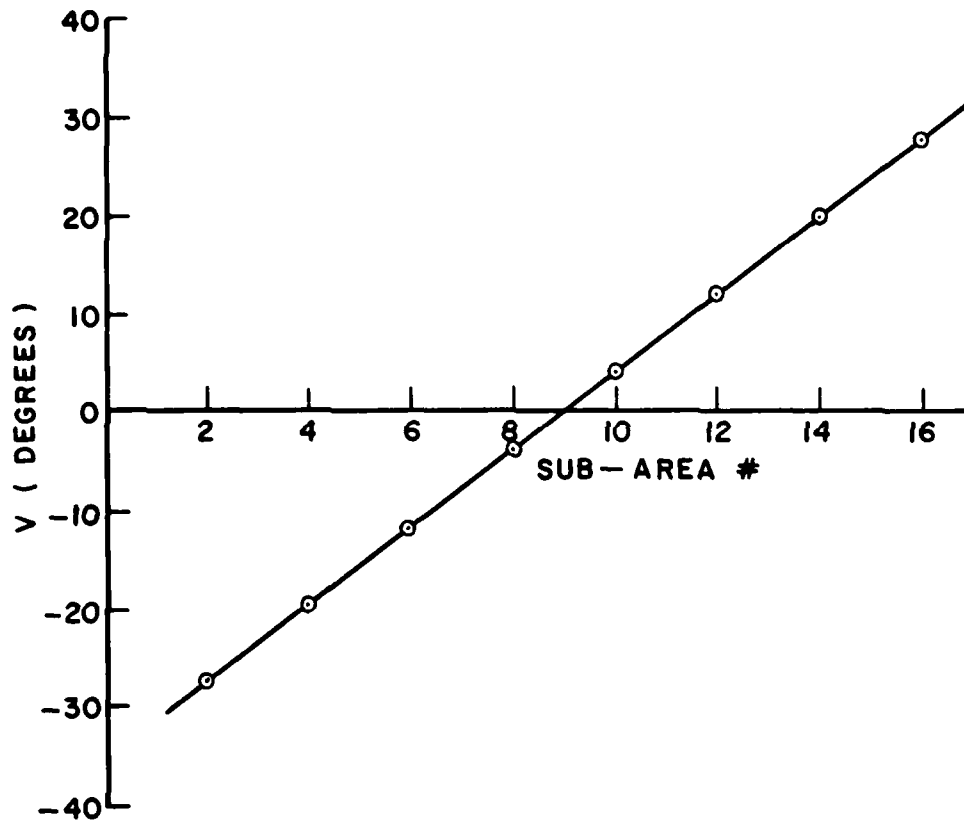


Figure 17. Reflection points (measured in angular parameter v) versus the sub-area location for the case shown in Figure 16. The sixth row in the scattering matrix is used.

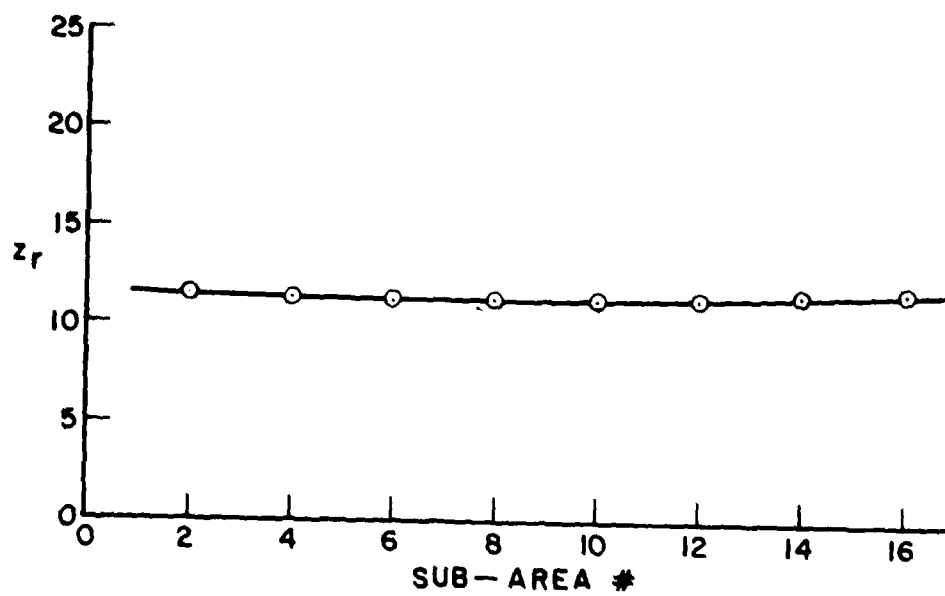


Figure 18. Reflection points (measured in vertical height z_r) versus the sub-area location for the same case shown by Figure 17.

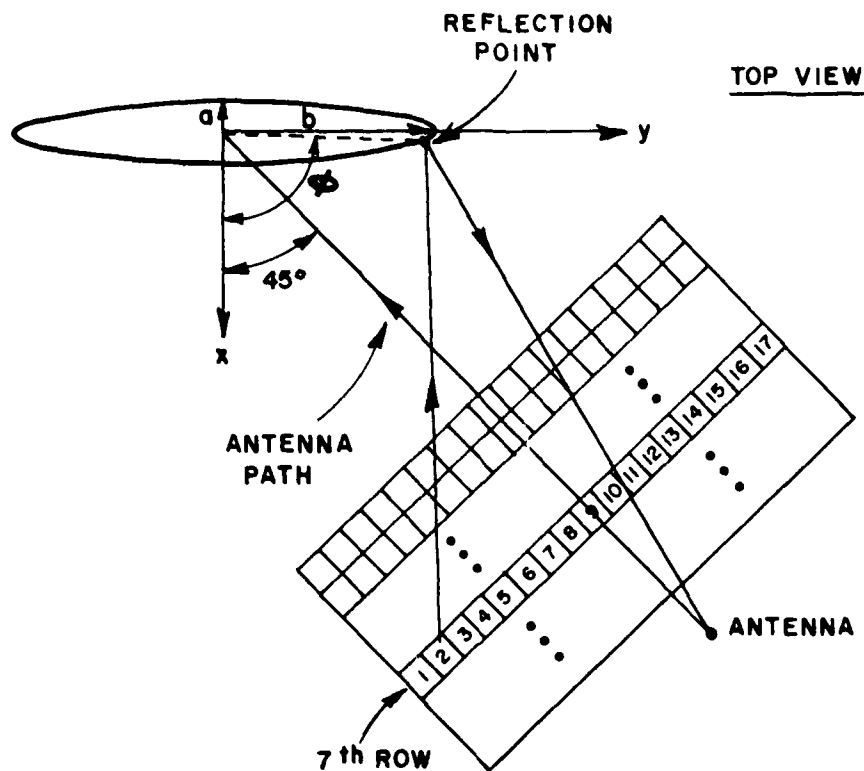


Figure 10. Characteristic view of elliptical cylinder and position matrix for off-broadside incidence of the antenna. The antenna is instantaneously fixed at location ($x=30.0$, $y=30.0$, $z=40.5$ and $a=3$, $b=30$; arbitrary distance units).

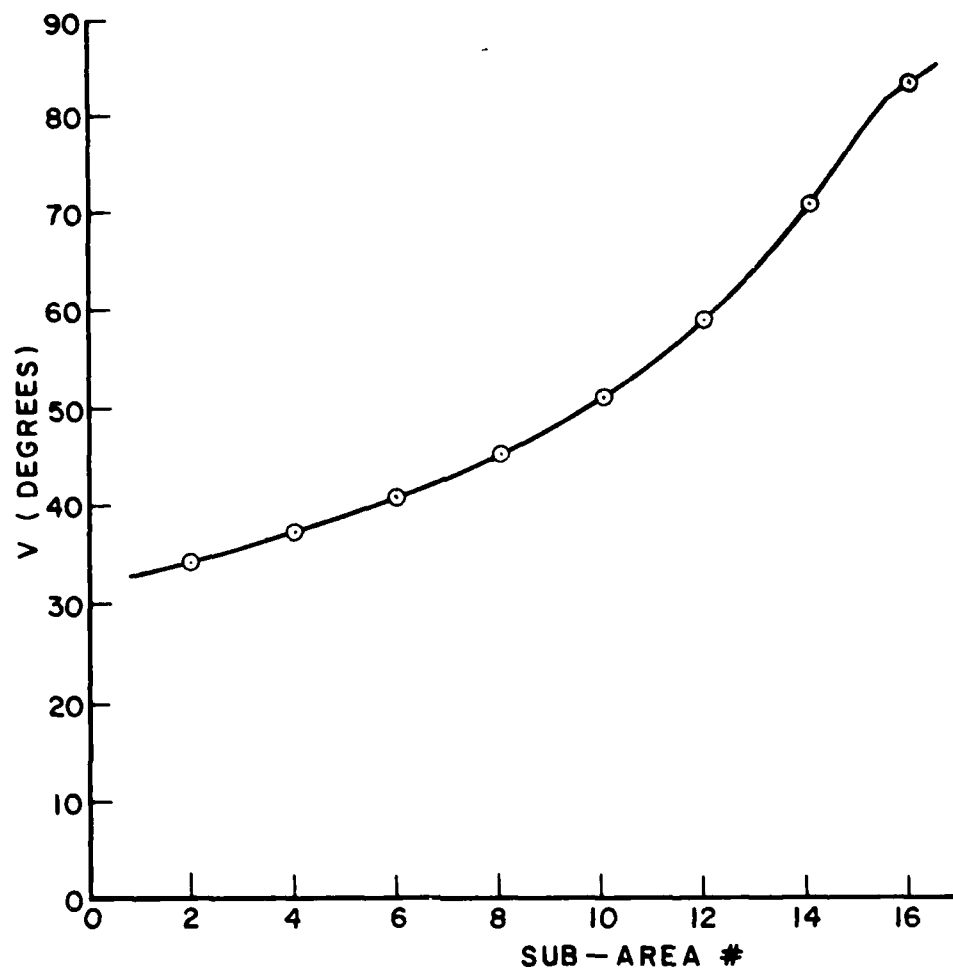


Figure 20. Reflection points (measured in angular parameter) v) versus the sub-area location for the case shown in Figure 19. The seventh row in the scattering matrix is used.

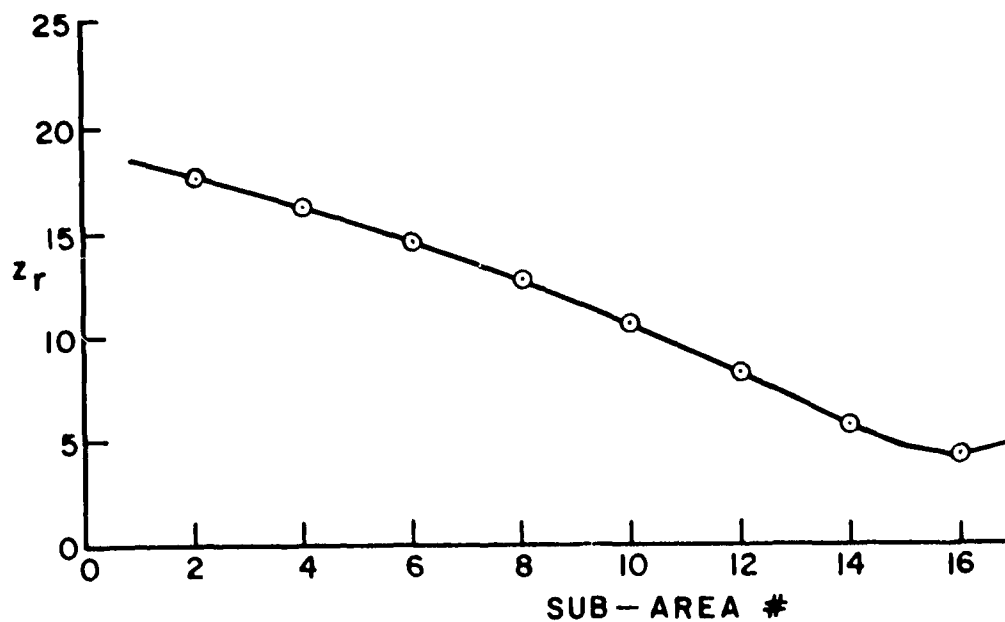


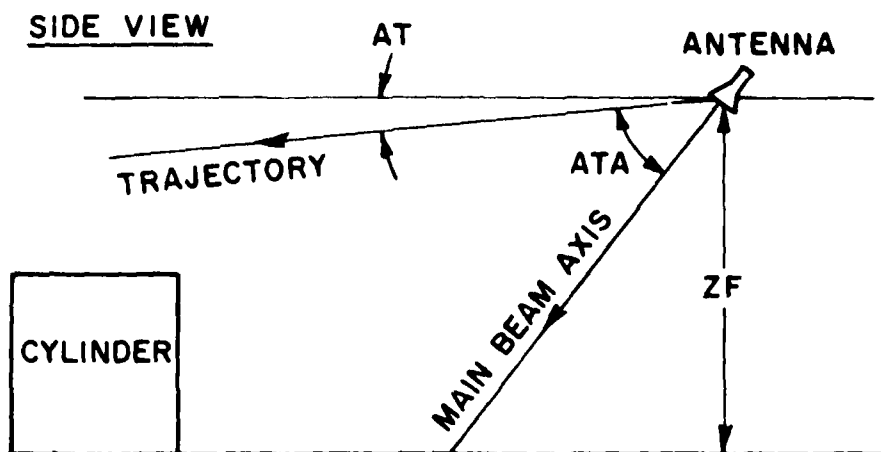
Figure 21. Reflection point (measured in vertical height - z_r) versus the sub-area locations for the same case shown by Figure 20.

as expected. The curves in Figures 17 and 18 are nearly straight lines for the reason that the broad face of the elliptical cylinder is nearly flat. The abrupt change at the end of the curves in Figures 20 and 21 is due to the fact that the reflection points have reached the narrow end of the elliptical cylinder where the surface curvature varies drastically with position.

D. Results

After the above technique and tests have been verified, we are now ready to consider the actual scattered fields at the receiver due to the double bounce corner contribution (forward scatter from transmitter to ocean to ship to receiver) as the radar position moves along a straight line. For each sub-area of the sea surface scattering grid, the field incident upon it is calculated from the antenna's radiation functions as expressed in Appendix A. The scattered field from this sub-area is then obtained by multiplying the incident field by a scattering coefficient which is a function of the angle of incidence, angle of reflection, sea surface characteristics, polarization of the incident field, and size of the sub-area as given by Equations (17) and (23). It is clear that the angle of reflection is determined by the location of the reflection point on the cylinder. This location is first calculated by the polynomial method and then tracked by the numerical search technique as the scattering source moves from one sub-area to another. Once the scattered field from the sub-area to the reflection point on the cylinder is computed, the reflected field from this reflection point to the receiver is readily calculated by the method of GTD which is given by Equation (1). The final solution is then a summation of all the doubly reflected fields for the sub-areas that are illuminated by the antenna. Of course, the field at the receiver terminals needs to be multiplied by the antenna pattern function again. A number of typical signatures for the geometry illustrated in Figure 22 have been calculated, and are shown in Figures 23 through 25.

In these, and subsequent signatures, the electromagnetic wavelength has been taken as the unit of length; i.e., the dimensions of the ship models, and the altitude (Z_F) and distance along the trajectory (RF) are given in units of wavelength. The signatures then represent the nominal received voltage V_r in dB versus the distance RF of the antenna from its starting position. Note that the receiver voltage is calculated only at finite intervals along the trajectory, the incremental distance being 1.2 length units in all signatures (except Figures 66-71). The received voltage has been interpolated between the calculated points to produce a continuous signature. Note also that the vertical scales of the plots indicate the nominal received voltage V_r in dB (i.e., $V_r = 20 \log E_r$), where E_r is the received electric field intensity in



TOP VIEW

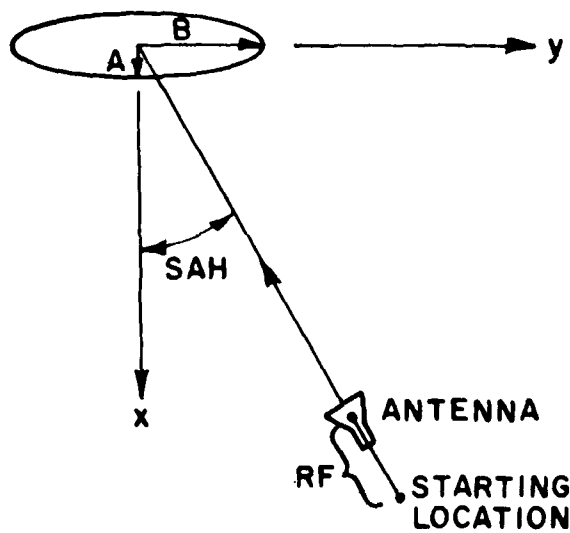


Figure 22. Configuration of elliptical cylinder at sea.
Patch size=3x3 length units. Vertical polarization
is employed.

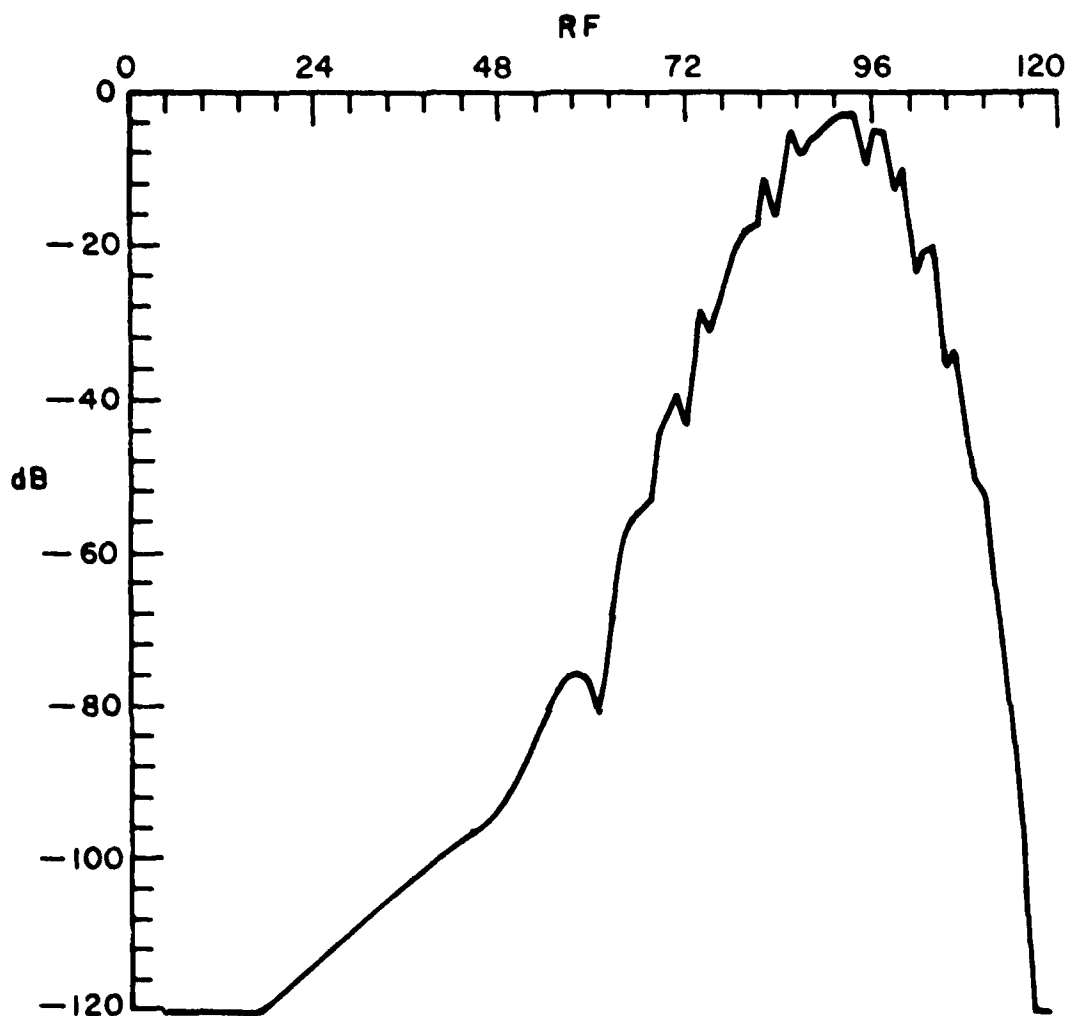


Figure 23. Voltage signature for the model of Figure 22. Horizontal trajectory ($AT=0^\circ$) at altitude 40.5 units. Ship dimension $A=5$, $B=25$ units. Antenna depression angle $ATA=60^\circ$. Antenna approach angle $SAH=0^\circ$. RF is the distance traveled by the radar from its starting location. The ship's center is located at $RF=120$ length units. Cylinder height is 24.36 length units.

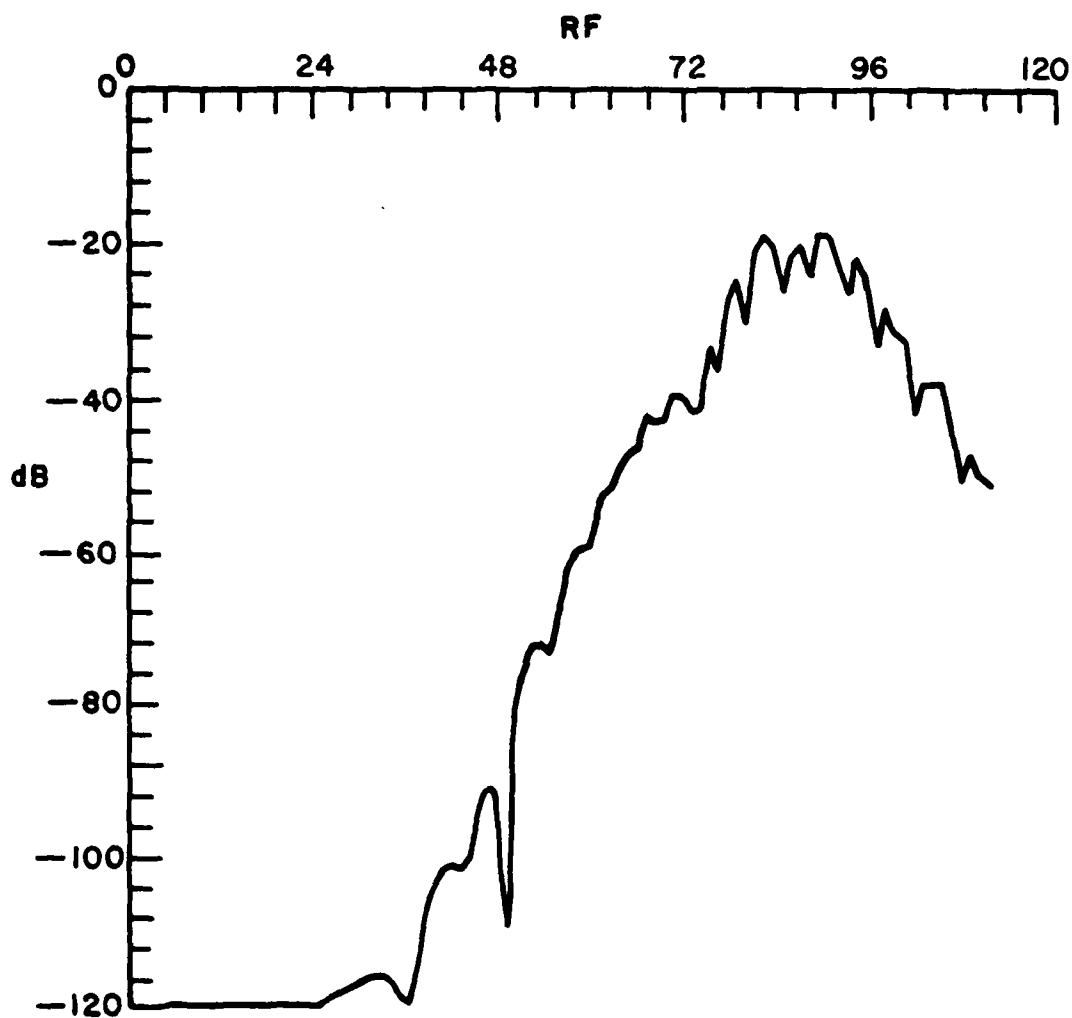


Figure 24. Voltage signature for the model of Figure 22.
All the parameters are the same as that for Figure 23
except the antenna approach angle $SAH=45^\circ$.

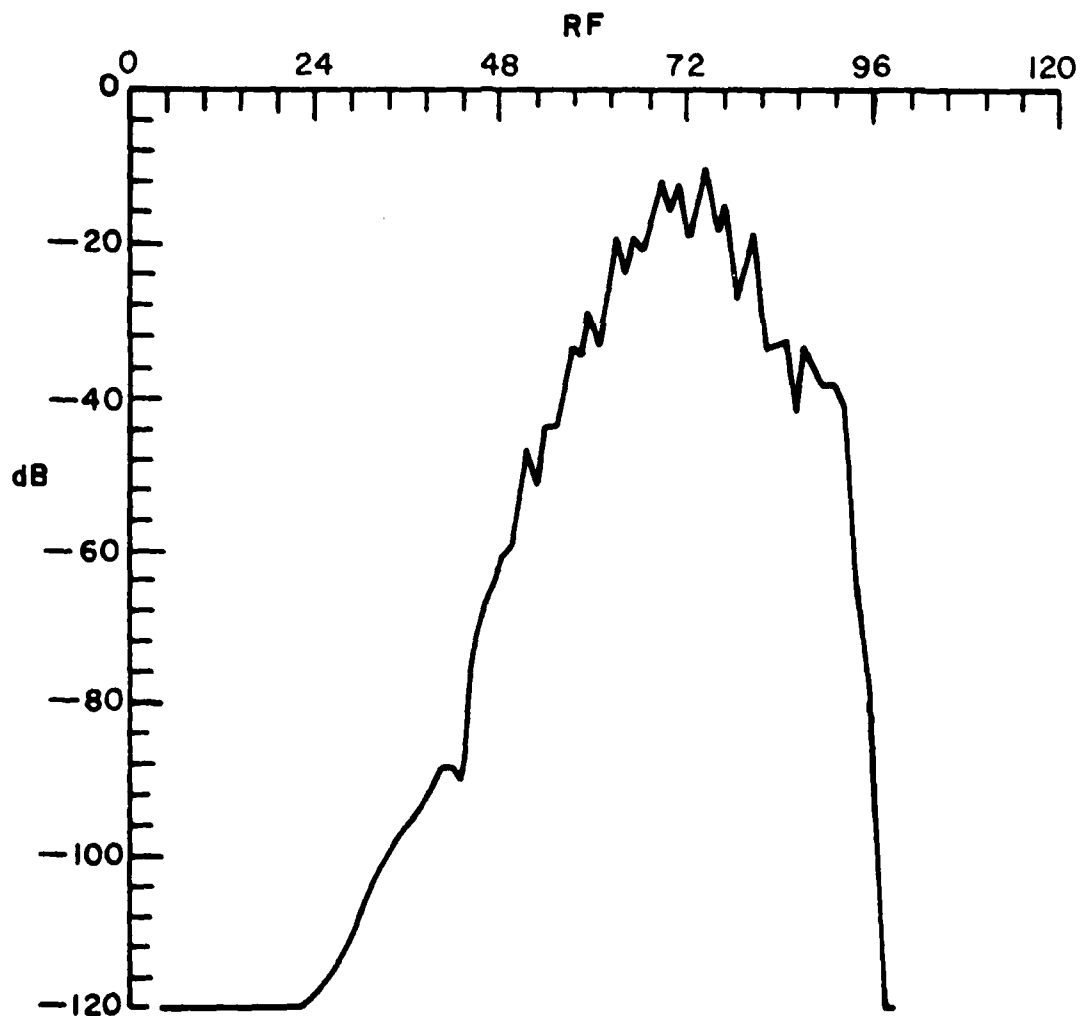


Figure 25. Voltage signature for the model of Figure 22.
All the parameters are the same as that for Figure 23
except the antenna approach angle $SAH=90^{\circ}$.

volts per meter calculated by the equations employed in this report. If one wishes to calculate the power delivered (P_{del}) to the matched load of the antenna from the scattered-voltage plots given in this report, given the power transmitted (P_t) from the antenna, the following equation is available

$$P_{del} = 10^{V_r/10} \frac{4 P_t G_t A_{eff}}{[J_0 a]^2 k^2 Z_0^2} \quad (38)$$

where G_t is the transmitting antenna directive gain, A_{eff} is the receiving antenna effective aperture, J_0 and a are defined in Appendix A, k is the free space wave number, and Z_0 is the free space impedance. Note that $10^{V_r/10}$ recovers the quantity E_r^2 in (volts/meter)².

Also in computing the signatures, it has been assumed that the dielectric constant is approximately that of sea water at S band ($\epsilon = 69 - j38$), and the r.m.s. slope of the ocean surface was 10° , and the antenna current has been taken as $J_0 a^2 = 1$. In computing the back-scattered and double-bounce contributions, the patch sizes were taken as 3×3 length units (except in Figures 66-71) and the patch array size was 17×17 (ie., 289 patches). Vertical polarization of transmitter and receiver was used, unless otherwise specified.

In Figures 23 through 25, signatures with horizontal trajectory ($AT=0^\circ$) made with a 15° antenna beam at a depression angle (ATA) of 60° are shown, for the case of the elliptic cylinder target with semi-major axis of 25 length units and a semi-minor axis of 5 length units. The trajectory altitude (ZF) is 40.5 length units, and the horizontal range (radar to target center) varies from 120 to 0 length units. The three different signatures in Figures 23 through 25 correspond to different antenna approach angles, which varied from broadside incident ($SAH=0^\circ$) to head-on ($SAH=90^\circ$). Although the general form of the signature is quite similar, being strongly influenced by the assumed Gaussian pencil beam antenna pattern, the trajectory and the beam depression angles, the relative received voltage varies markedly as the approach angle changes. Among the three computer plots, the received voltage level is the lowest when the approach angle is 45° ; this is because the energy that is concentrated in the main beam is being reflected away by the cylinder instead of being reflected back to the receiver, as happened in the other two cases. The reason that the head-on signature is lower than the broad-side signature is apparently because of the higher energy spreading factor due to the larger curvature in the bow or stern region.

The direct backscattered signal (i.e., the "clutter signal") from each ocean sub-area is computed using the formulation presented

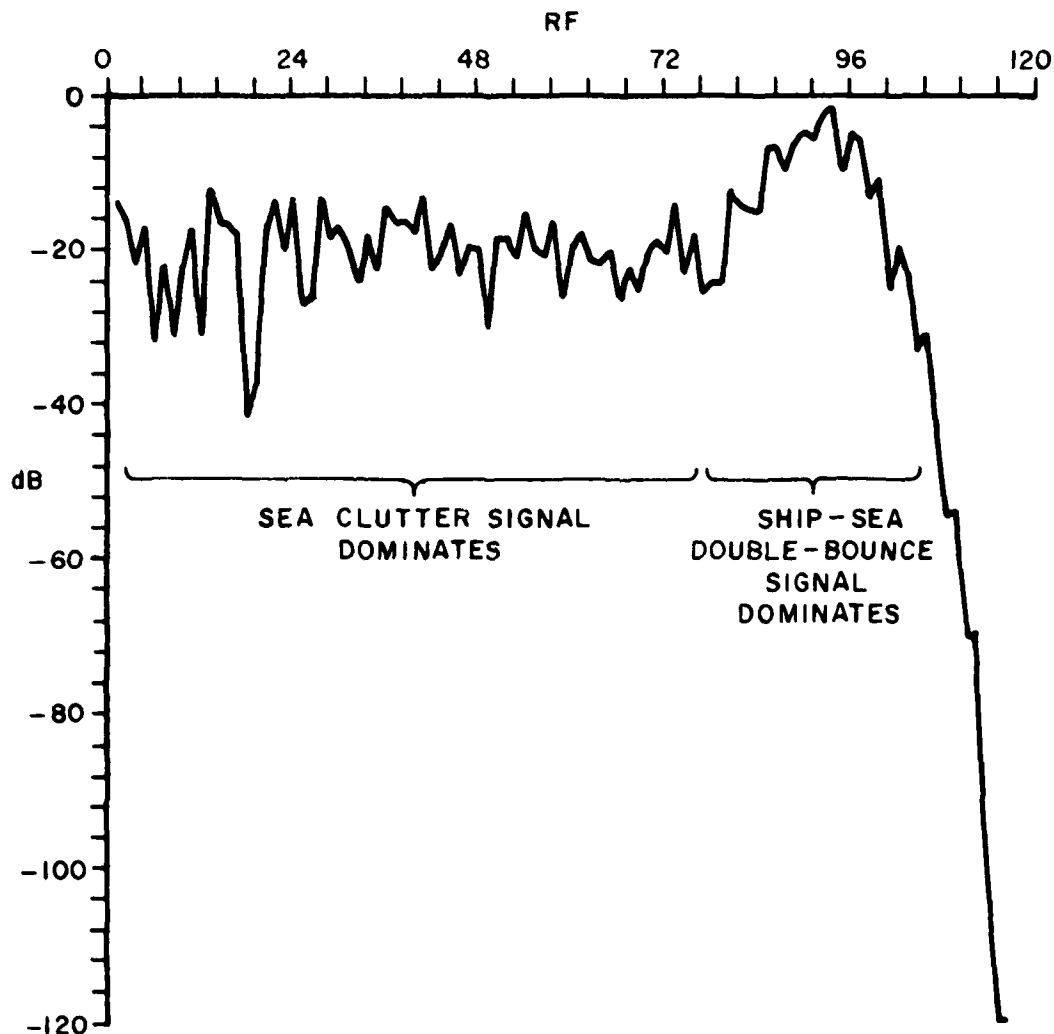


Figure 26. Ship-sea double-bounce signal plus the ocean back-scattered signal for the geometrical model of Figure 22. Trajectory is horizontal ($AT=0^\circ$) at altitude (ZF) of 40.5 units. Ship dimension is $A=5$, $B=25$ units. Antenna depression angle (ATA) is 60° . Antenna approach angle (SAH) is 0° . RF is the distance traveled by the radar from its starting location. The ship's center is located at $RF=120$ length units. Cylinder's height is 24.36 length units.

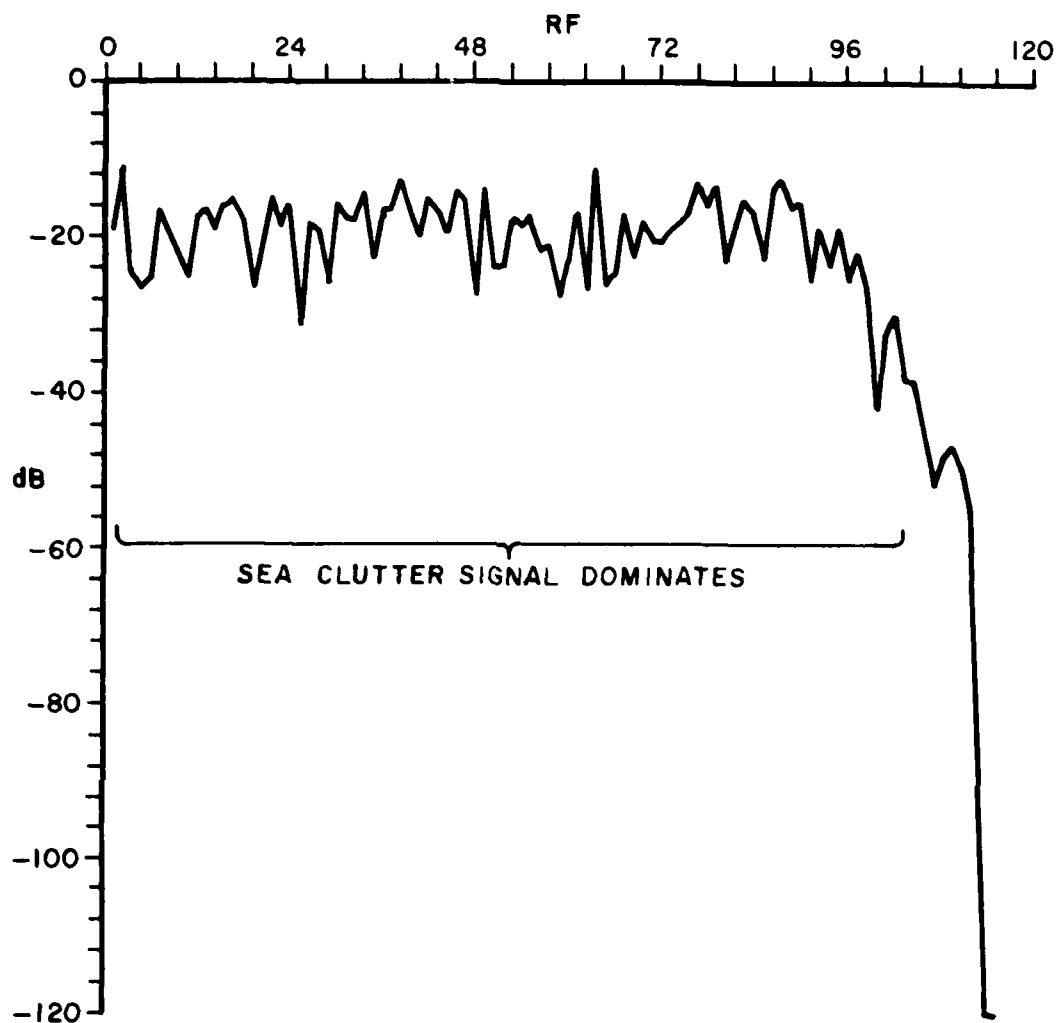


Figure 27. Ship-sea double-bounce signal plus the ocean back-scattered signal for the geometrical model of Figure 22.
All the parameters are the same as that for Figure 26 except the antenna approach angle $SAH=45^\circ$.

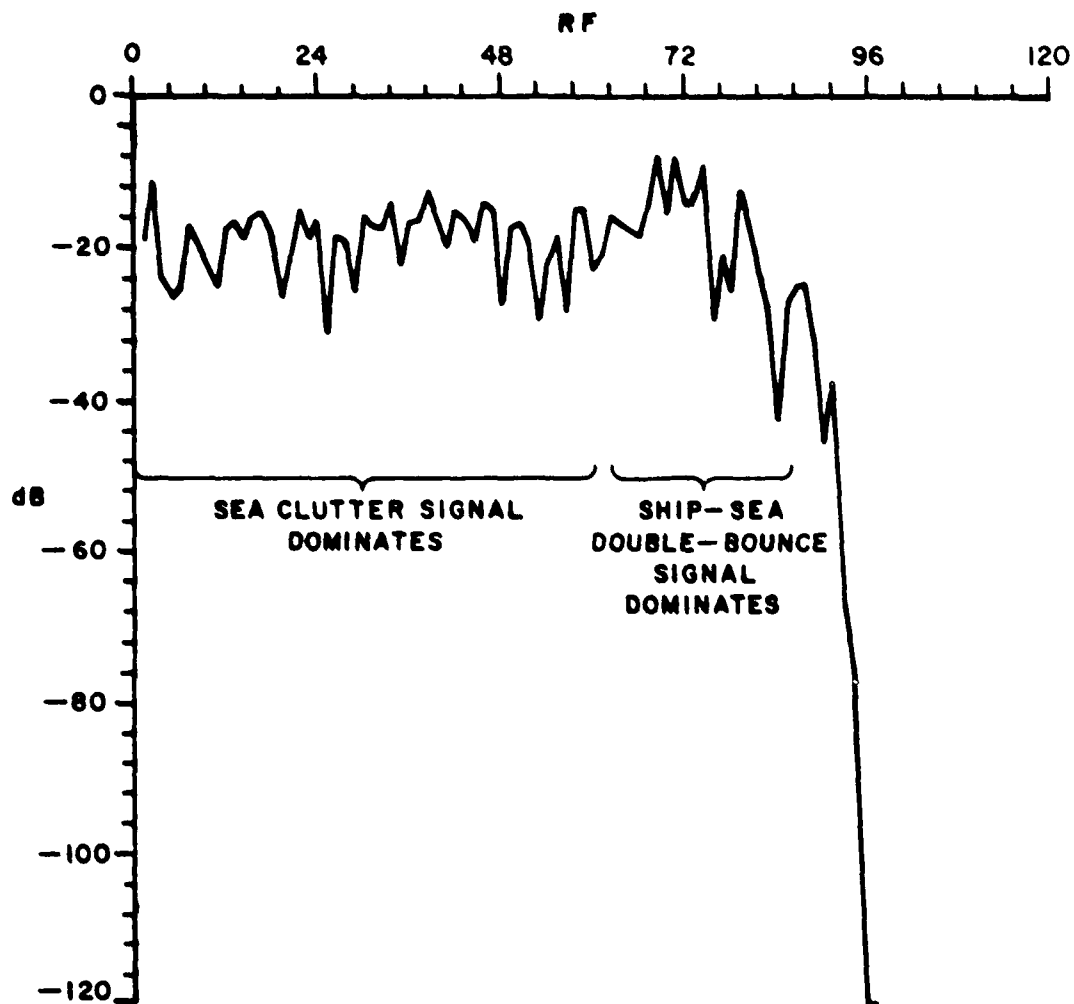


Figure 28. Ship-sea double-bounce signal plus the ocean back-scattered signal for the geometrical model of Figure 22. All the parameters are the same as that for Figure 26 except the antenna approach angle $SAH=90^\circ$.

in Chapter IV. A uniformly distributed random phase for each sub-area path is incorporated into the backscattered field. These random backscattered signals, summed with the forward sea scattered double-bounce signals, are illustrated in Figures 26 through 28. It can be seen from these figures that, except for broadside incidence, the ship-sea double-bounce signals have mostly disappeared into the noise-like sea clutter signal. In other words, the sea clutter signal has contaminated the signal caused by the double-bounce ship-sea interaction. The sudden termination of the signal near the end of the trajectory is caused by the fact that signals from the illuminated sea patches beyond the ship were not included in the calculation.

In considering the exact form of the range dependent clutter signal (which would thus be the time dependent signal in a radar moving with constant velocity) it is important to bear in mind one feature of the computer program which implements the calculation. To simplify certain geometrical factors in the calculation, the grid of sub-areas was referenced to the antenna position rather than the position of the ship. That is, the entire grid moves over the sea surface along with the antenna. At each point of the trajectory, a new set of random phase angles was generated for each sub-area. It is clear that this procedure will generate a discontinuous time function no matter how small the incremental distance along the trajectory between calculations. Thus each point on the clutter part of the signal, and the clutter modulation of the double bounce return must be regarded as a sample from a different number of an ensemble of signatures (an attempt to obtain the doppler spectrum of a position of the signal by taking its Fourier transform would produce essentially a white noise spectrum rather than the correct spectrum). Note also that because the clutter signal is the sum of a number of signals with random phase, there is a finite probability that total clutter signal may be considerably larger than the levels indicated for short intervals (roughly the reciprocal of the fade rate).

It is a relatively simple matter to change the program so as to keep the sub-areas fixed relative to the ship, and to assign a random phase shift δ_n to each sub-area which would remain constant for the entire trajectory. This would produce a continuous signature, which should be a good approximation to the correct signature for a "frozen" sea surface, i.e., for a surface which does not change significantly during the time over which the signature is computed. The doppler spectrum, in turn, should then be a good approximation to the correct spectrum. A more difficult problem would occur if it were desired to take into account the effect of the actual motion of the sea surface on the time signal and the spectrum. In this case the δ_n should be random functions of time, varying at a rate compatible with the surface motion. We have not addressed the problem of determining a suitable form (amplitude, spectrum, etc.) for the $\delta_n(t)$.

At this stage, having produced a program to compute both the forward and back scattering from the ocean surface, it may be appropriate to ask the question: What is the appropriate size for the sub-area or patch in the model? The ocean surface model is a statistical one, with a uniformly distributed random-phase assigned to each patch. It is clear that the r.m.s. scattered field averaged over a number of trajectories should be independent of the size of each sub-area, as long as the total illuminated area is kept constant. Even though Equation (17) indicates that the scattered field from a single sub-area does depend on the physical area A_0 , one should realize that when A_0 is reduced, the total number of sub-areas will consequently be increased. However, the size of each sub-area can not be chosen arbitrarily. The size can not be too small otherwise computer time will become a problem, and from a physical point of view the model will be incorrect because it will assign uncorrelated returns (because of the random phase term) to scattering from arbitrary close surface points. Nor can the patch size be chosen too large, otherwise one may miss some of the dominant specular reflection points. In Figure 29, a number of ship-sea double-bounce signatures have been calculated as the sub-area width (pw) was varied from one length unit to ten length units. The signatures are calculated for the same geometry as that for Figures 12 and 13 except that the antenna beam depression angle is chosen to be 30° instead of 60° . It can be seen that, for the frequency range and target size being used, the average signatures are nearly invariant to the sub-area size. This empirical finding has permitted us to use fairly large patch sizes of six to ten length units, and thus achieve reasonable program run times.

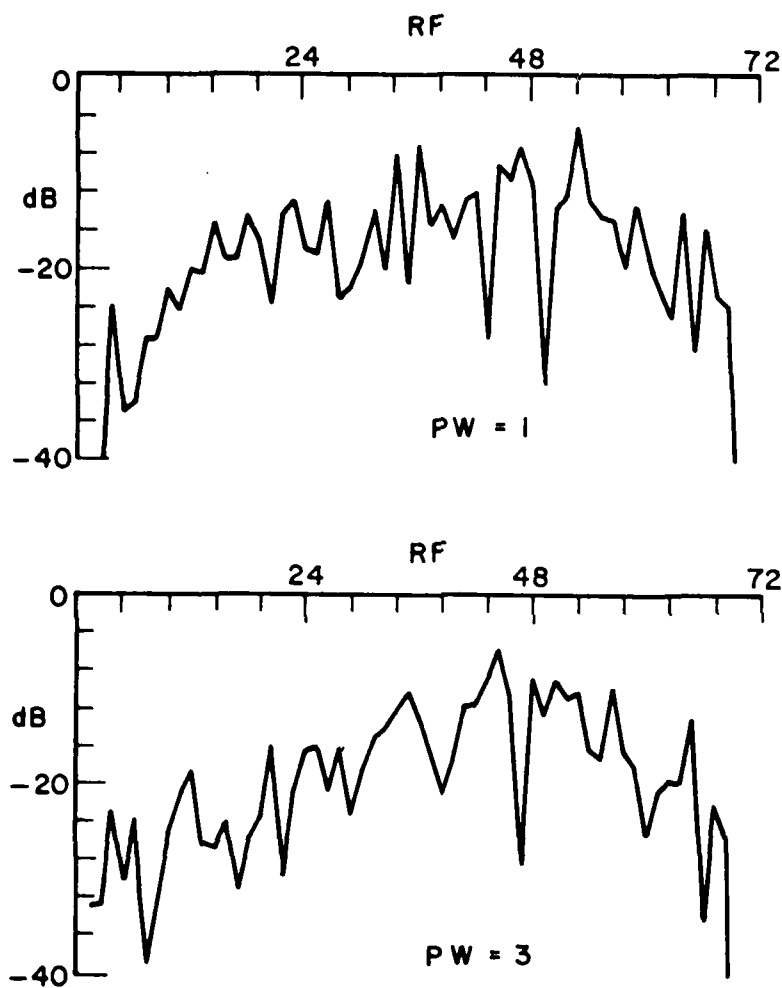


Figure 29. Ship-sea double bounce signatures. RF is the distance traveled by the radar from its starting position. Patch width PW is in length units. Antenna beam depression angle is 30° . Antenna approach angle $SAH=0^\circ$. Ship's center is located at $RF=120$ length units.

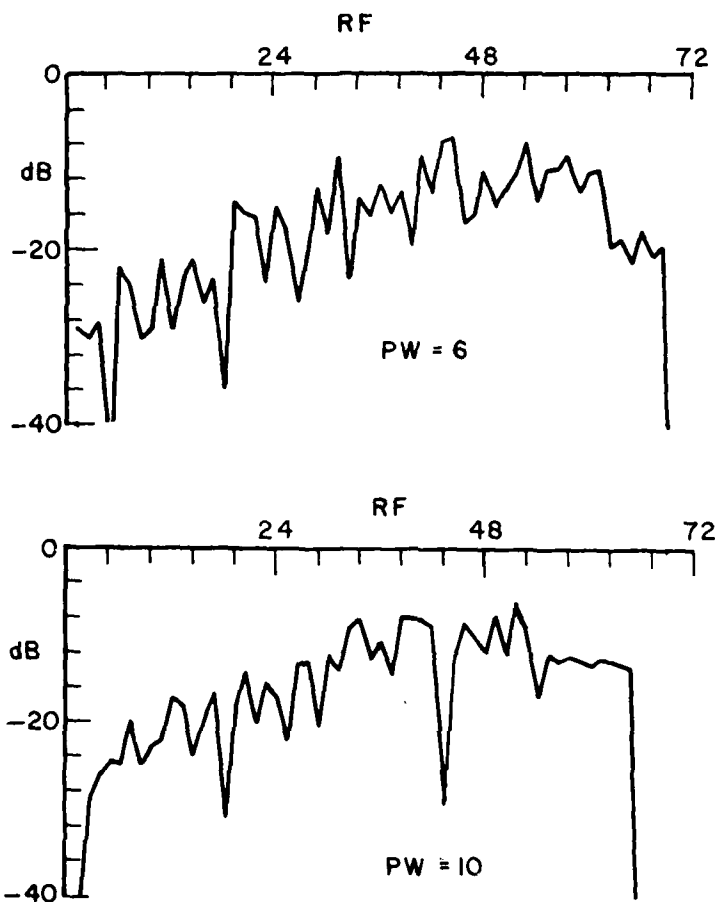


Figure 29 (continued). Ship-sea double-bounce signatures. Patch width PW in length units. Antenna beam depression angle is 30° . Antenna approach angle $SAH=0^\circ$. Ship's center is located at $RF=120$ length units.

CHAPTER VI SHIP SCATTERED SIGNATURES

Having illustrated the calculation of the back-scattered (clutter) signal from the sea and the ship-sea interaction term, the scattering from the ship itself must now be considered. In this chapter the simplified ship model is represented by two superimposed finite elliptic cylinders, and the computationally efficient GTD technique is utilized to compute the backscattered signals. There are two principal scattering mechanisms that contribute to the signature from the ship. These are the signatures caused by the corner reflection between the two cylinders, and the signatures due to diffracted-then-reflected (and reflected-then-diffracted) fields between the edge of one cylinder and the flat "deck" region. There is also a third backscattering mechanism, which is the direct diffraction from the curved wedges of either of the two cylinders. However, since the back diffracted direction is not anywhere close to the shadow boundaries, as illustrated in Figure 30, the direct diffracted energy is too small to be considered here.

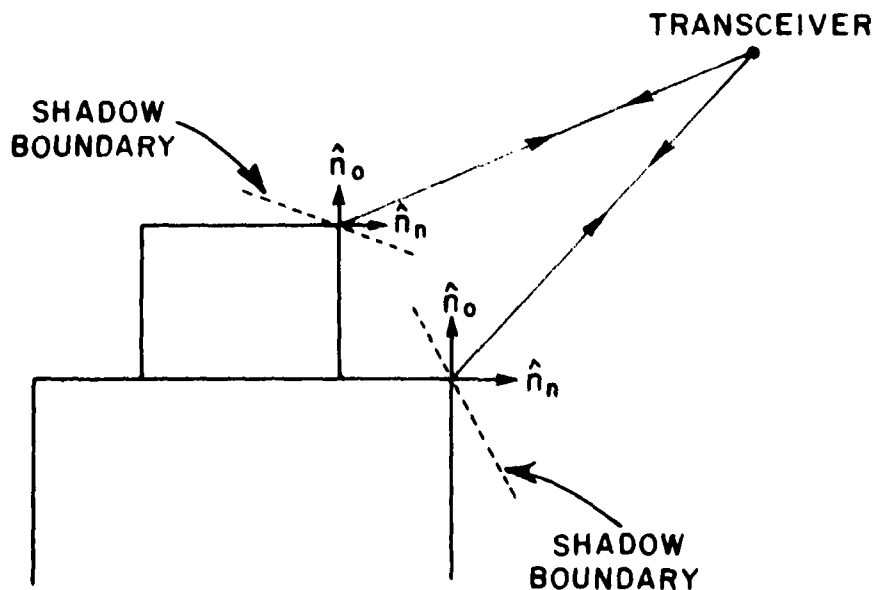


Figure 30. Direct wedge diffractions showing the shadow boundaries.

The two major ship scattering mechanisms are described below:

A. Corner reflected signature

The corner reflected signature as illustrated in Figure 31a is the signature bounced between the top flat surface of the bottom cylinder and the curved surface of the top cylinder. It is simple to show, using image theory, that if the surfaces are perpendicular to each other, then there exists only one reflection point, located at the corner between the two cylinders as shown in Figure 31b. Thus, one is able to move the source point to its image location as shown in Figure 31c, and the corner reflected field can then be computed as a single reflection from an elliptic cylinder. On this cylinder, the reflection point in the z-direction is always fixed at the height of the corner; but the reflection point in the x-y plane, designated by the angle ϕ as shown in Figure 32, remains to be determined. The elliptic parameter (v) is related to ϕ by $v = \arctan[(A^2/B^2)\tan\phi]$.

From the laws of reflection as described by Equation (2) and with the aid of the numerical search technique presented in Chapter V, the reflection point or the parameter v can be accurately specified. Knowing the location of the reflection point, Equation (1) can then be employed to calculate the corner reflected field received by the antenna. This corner reflected field for the geometry shown in Figure 33 is plotted against the distance traveled by the antenna in Figure 34. In this figure, the three different curves are distinguished by the three different antenna approach angles (SAH). The situations encountered here are similar to those observed with the ship-sea double-bounce signatures, where the received signal is the lowest when the approach angle is 45° , and the head-on reflection is lower than that for broadside incidence, for the same reason as given previously. However, one additional feature that can be more clearly noticed in Figure 34 is that the peak of the head-on signal occurs much earlier than the other two due to the fact that the bow of the ship is much closer to the relative antenna position than the broadside face of the ship. Since the ship model is assumed to be a perfect conductor, the above corner reflected signatures are expected to have the highest voltage level at the receiver terminal among all the signatures that are investigated in this report.

B. Diffracted-reflected signatures

The diffracted-reflected signature represents the field that is diffracted by the top wedge of the bottom cylinder and then reflected off the curved surface of the top cylinder. By the principle of reciprocity, the diffracted-reflected signature depicted in Figure 35a will produce the same voltage at the receiver terminal as the reflected-diffracted signature shown in Figure 35b. Hence

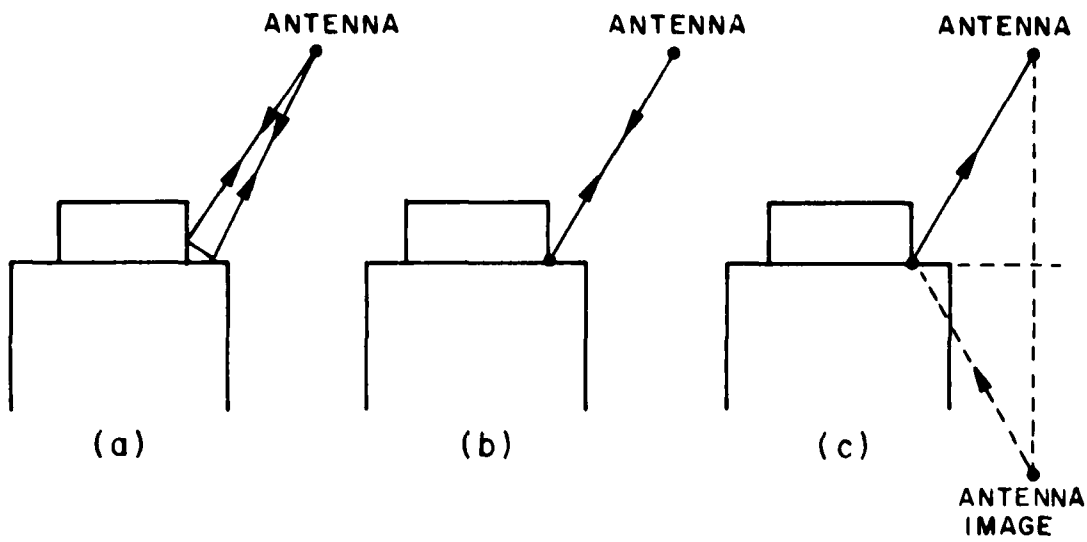


Figure 31. Corner reflection configurations.

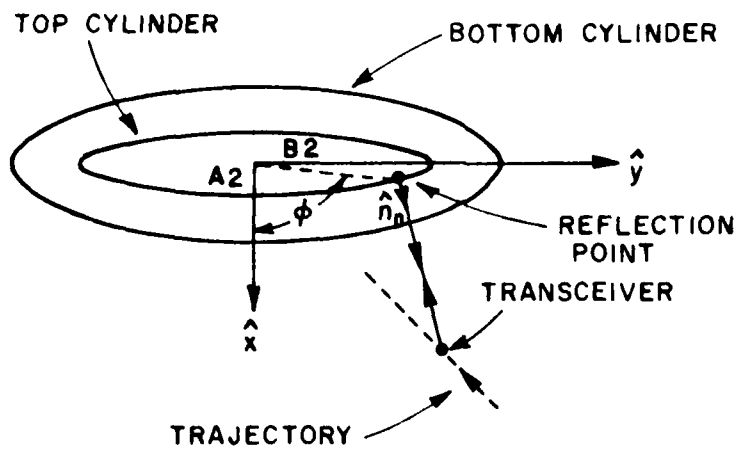


Figure 32. Top view of the ship's corner reflection.

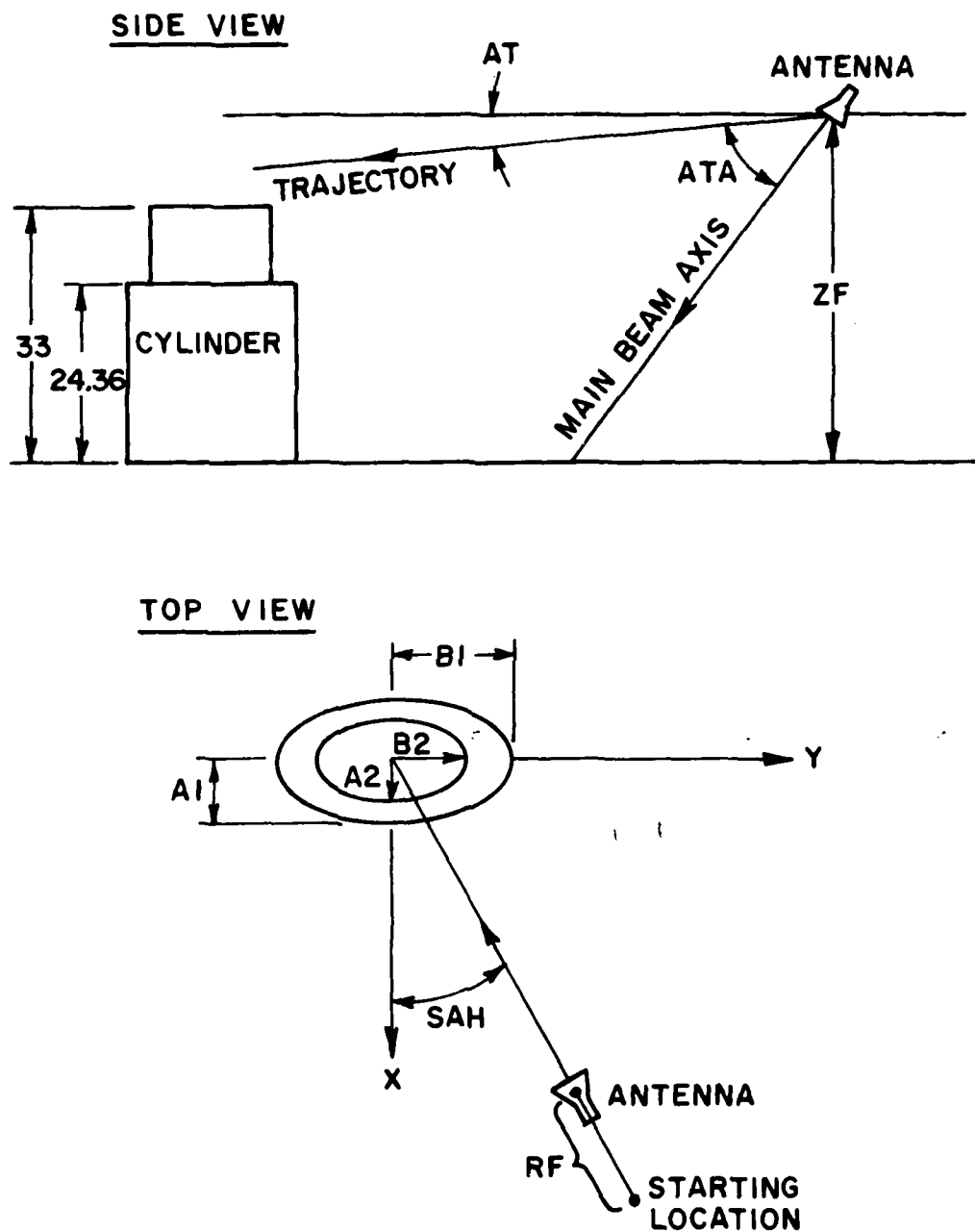


Figure 33. Configuration of two superimposed elliptic cylinders with respect to the antenna position.

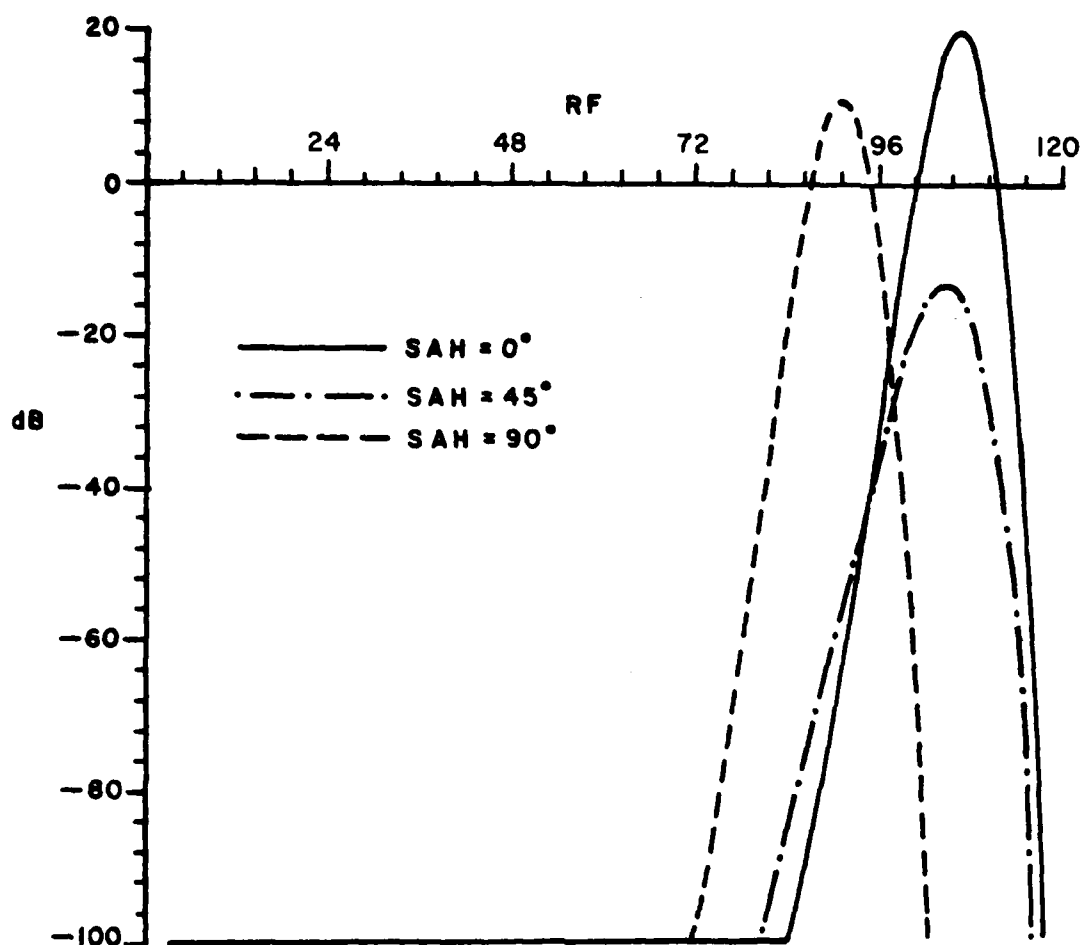


Figure 34. Corner reflected signatures between the two cylinders
 RF is the distance traveled by the radar from its starting
 locations. The vertical axis is the received voltage
 level measured in decibels. Ship's center is located
 at RF=120 length units. Ship dimensions are: A1=5,
 B1=25, A2=4, B2=20 length units. Two cylinders'
 heights are ZCY=24.36, ZCY2=33 length units.

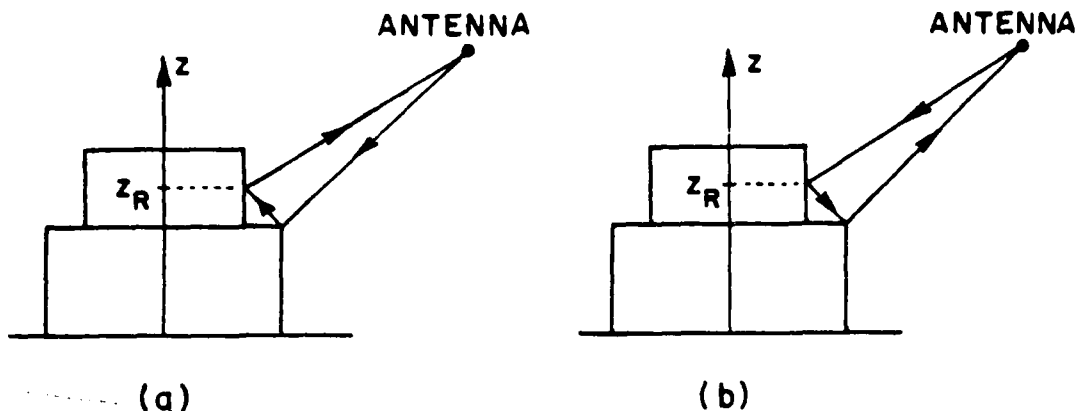


Figure 35. Ship scattering mechanisms for (a) diffracted-reflected signature (b) reflected-diffracted signature.

the received field due to these two scattering mechanisms is just twice the field predicted by either one. In order to calculate this term, it is essential that one accurately locate the diffraction point (ϕ_1) along the bottom cylinder's wedge, and the reflection point (ϕ_2, z_1) on the curved surface of the top cylinder as illustrated by Figure 36. A numerical search technique is employed again to find these points. This time not only do the laws of reflection need to be satisfied, but it is also required to satisfy the law of diffraction, as given by

$$-\frac{\vec{I}}{|\vec{I}|} \cdot \frac{\vec{e}}{|\vec{e}|} = -\frac{\vec{d}}{|\vec{d}|} \cdot \frac{\vec{e}}{|\vec{e}|} = \cos \beta_0 \quad (39a)$$

where \vec{e} and β_0 have been defined before in section (III-2) and (III-3) with

$$\vec{e} = -A \sin v_1 \hat{x} + B \cos v_1 \hat{y}.$$

where $v_1 = \tan^{-1} \left(\frac{A_1}{B_1} \tan \phi_1 \right)$.

The incident vector is given by

$$\begin{aligned} \vec{I} &= I_x \hat{x} + I_y \hat{y} + I_z \hat{z} \\ &= (A \cos v_1 - x_0) \hat{x} + (B \sin v_1 - y_0) \hat{y} + (z_d - z_0) \hat{z} \end{aligned}$$

where (x_0, y_0, z_0) is the antenna location and z_d is the height of the bottom cylinder. The diffracted vector is given by

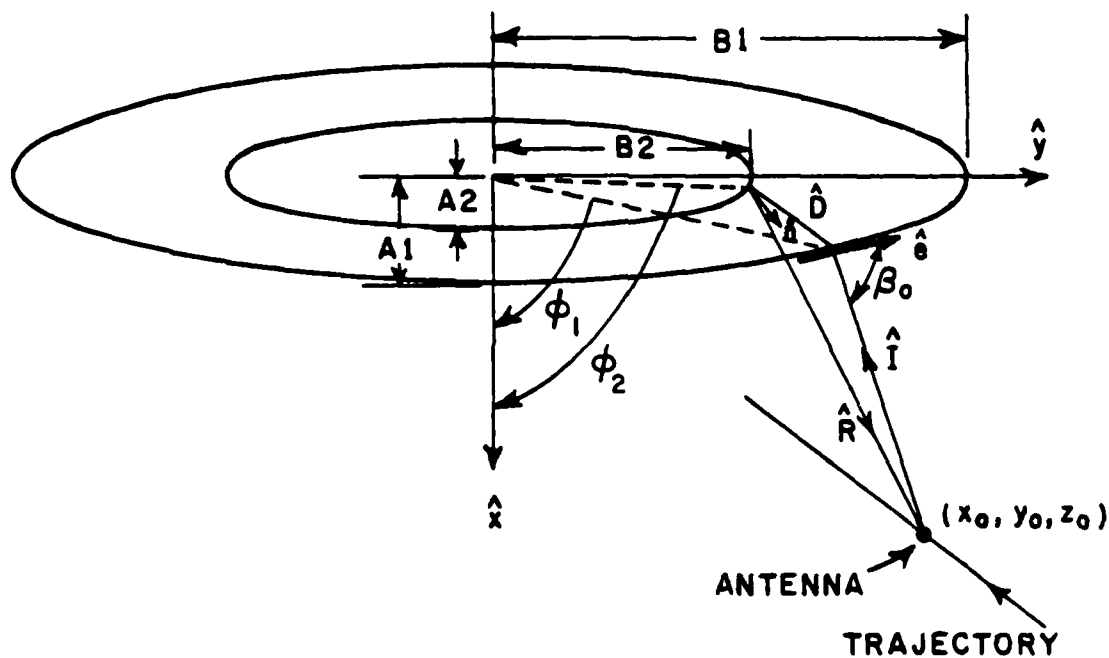


Figure 36. Top view of the diffracted-reflected configuration.

$$\begin{aligned}\vec{D} &= D_x \hat{x} + D_y \hat{y} + D_z \hat{z} \\ &= (A_2 \cos v_2 - A_1 \cos v_1) \hat{x} + (B_2 \sin v_2 - B_1 \sin v_1) \hat{y} + (z_r - z_d) \hat{z}\end{aligned}$$

where $v_2 = \tan^{-1} \left(\frac{A_2}{B_2} \tan \phi_2 \right)$,

A_1 , A_2 , B_1 , B_2 (semi-minor and semi-major axes of the lower and upper cylinders) and z_r is the height of the reflection point from the sea surface.

The reflected ray unit vector direction is given by

$$\begin{aligned}\vec{R} &= R_x \hat{x} + R_y \hat{y} + R_z \hat{z} \\ &= (x_0 - A_2 \cos v_2) \hat{x} + (y_0 - B_2 \sin v_2) \hat{y} + (z_0 - z_r) \hat{z}\end{aligned}$$

From Chapter III, the laws of reflection can be combined to form

$$(\vec{n} \cdot \vec{D})(\vec{n} \times \vec{R}) + (\vec{n} \times \vec{D})(\vec{n} \cdot \vec{R}) = 0 \quad (39b)$$

where $\vec{n} = n_x \hat{x} + n_y \hat{y}$

$$= B_2 \cos v_2 \hat{x} + A_2 \sin v_2 \hat{y}.$$

Equation (39a) can be rearranged to give

$$f_1(v_1, v_2, z_r) = \frac{\vec{I}}{|\vec{I}|} \cdot \vec{e} - \frac{\vec{D}}{|\vec{D}|} \cdot \vec{e} \quad (40)$$

and Equation (39b) can be separated into two equations (as in Equations (33a) and (33b)) in the form

$$f_2(v_1, v_2) = (n_x D_x + n_y D_y)(n_x R_x - n_y R_y) + (n_x R_x + n_y R_y)(n_x D_y - n_y D_x) = 0 \quad (41)$$

$$f_3(v_1, v_2, z_r) = (n_x D_x + n_y D_y)R_z + (n_x R_x + n_y R_y)D_z = 0 \quad (42)$$

The method of Taylor Series expansion, as described in Section V-A, can again be applied here to Equations (41), (42) and (43) to form the search equation given by

$$\begin{bmatrix} \delta v_1 \\ \delta v_2 \\ \delta z_r \end{bmatrix} = \begin{bmatrix} \partial f_1 / \partial v_1 & \partial f_1 / \partial v_2 & \partial f_1 / \partial z_r \\ \partial f_2 / \partial v_1 & \partial f_2 / \partial v_2 & 0 \\ \partial f_3 / \partial v_1 & \partial f_3 / \partial v_2 & \partial f_3 / \partial z_r \end{bmatrix}^{-1} \begin{bmatrix} AF \\ BF \\ CF \end{bmatrix} \quad (43)$$

where $AF = -f_1 - \frac{\partial f_1}{\partial x_0} \delta x_0 - \frac{\partial f_1}{\partial y_0} \delta y_0 - \frac{\partial f_1}{\partial z_0} \delta z_0$

$$BF = -f_2 - \frac{\partial f_2}{\partial x_0} \delta x_0 - \frac{\partial f_2}{\partial y_0} \delta y_0$$

$$CF = -f_3 - \frac{\partial f_3}{\partial x_0} \delta x_0 - \frac{\partial f_3}{\partial y_0} \delta y_0 - \frac{\partial f_3}{\partial z_0} \delta z_0$$

The new diffraction and reflection points are then given by

$$v_1^{\text{new}} = v_1^{\text{old}} + \delta v_1$$

$$v_2^{\text{new}} = v_2^{\text{old}} + \delta v_2$$

$$z_r^{\text{new}} = z_r^{\text{old}} + \delta z_r$$

One sees that Equation (43) implies that, as the antenna moves by an incremental distance of $(\delta x_0, \delta y_0, \delta z_0)$, the diffraction point moves by an incremental amount δv_1 and the reflection point by increments of δv_2 and δz_r . The right hand side of Equation (43) is not only a function of the change in antenna position but is also a function of the previous locations of (ϕ_1) , (ϕ_2, z_r) and (x_0, y_0, z_0) . Therefore, there still remains the task of finding the initial scattering points (v_1) and (v_2, z_r) so that the search equation can begin to generate the new points. Consequently, one must start with the antenna at such a position that the scattering points can be easily found. For example, the antenna can be initially located in the x-z plane as illustrated in Figure 37, and one can immediately see that $v_1 = v_2 = 0$. The reflection point z_r can also be easily calculated and is given by

$$z_r = \frac{A1 - A2}{XA + A1 - 2 \cdot A2} z_A$$

where all the parameters are defined in Figure 37.

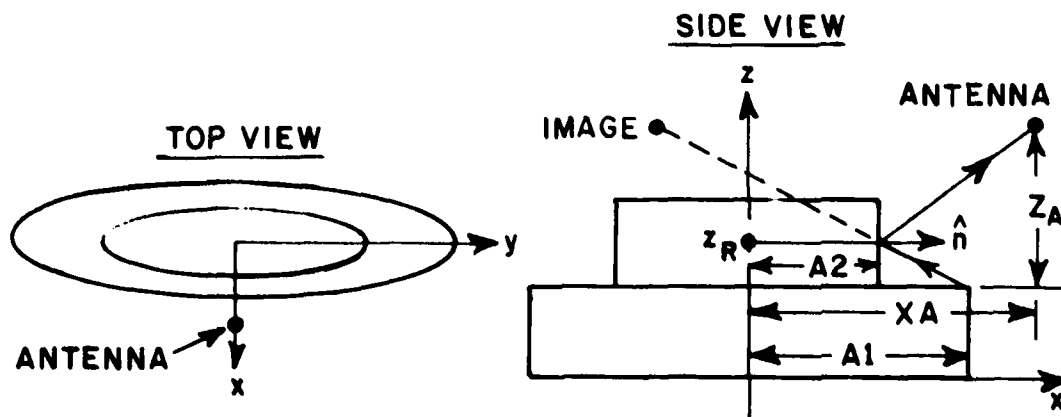


Figure 37. Configuration of the initial scattering points for the search equation.

At any location along the trajectory, once the scattering points are found by the numerical search technique, the diffracted and reflected fields can be obtained by Equations (12) and (1), respectively. Figure 38 shows the diffracted-reflected fields plotted against the incremental distance traveled by the antenna for three different antenna approach angles. The geometrical configuration used for these plots is illustrated in Figure 33. The general shapes of these plots are very similar to those obtained for the corner reflected field given in the previous section. This is expected, since the antenna provides a concentrated beam pattern and the size of the two elliptic cylinders are very much the same, thereby causing the scattering points of the two scattering mechanisms to be located close to each other. The amplitude of the diffracted-reflected

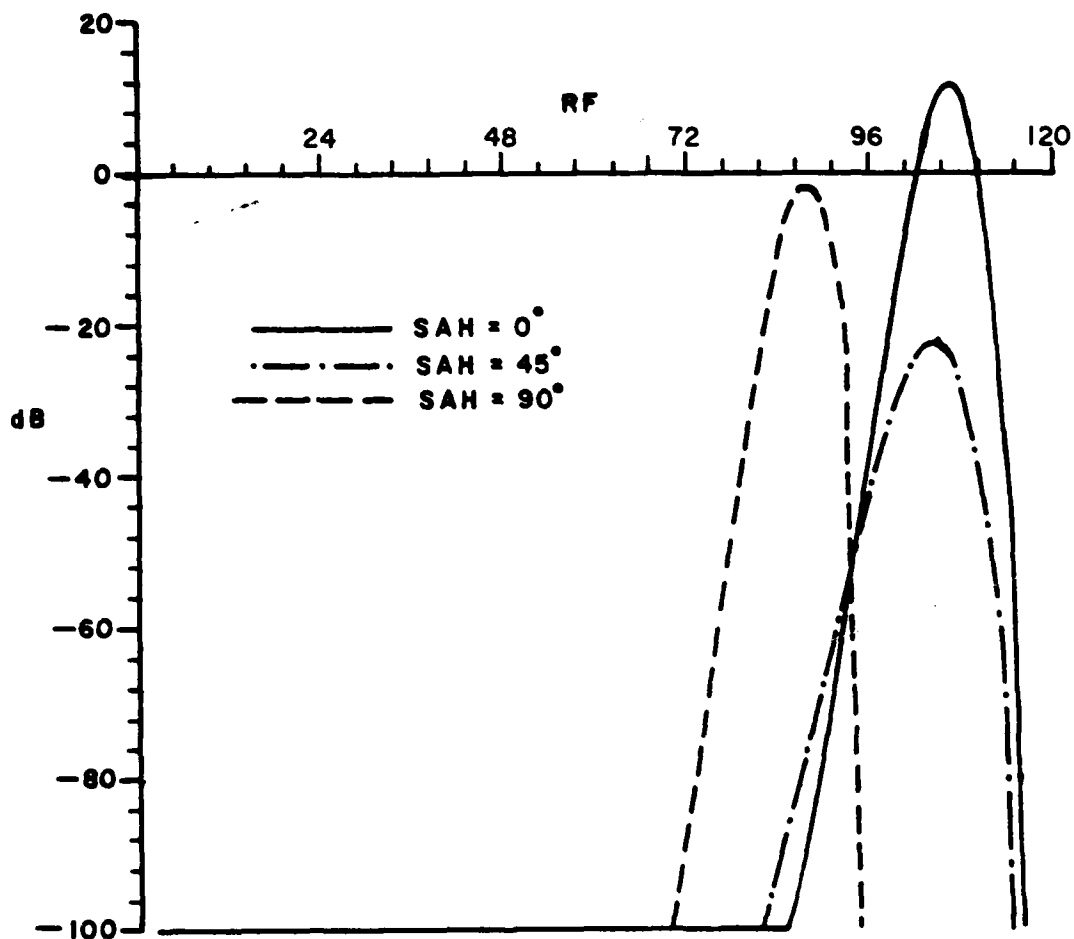


Figure 38. Diffracted-reflected fields between two elliptic cylinders. RF is the distance traveled by the radar from its starting location. Ship's center is located at RF=120 length units. Antenna-beam depression angle $ATA=60^\circ$. Ship dimensions are: $A1=5$, $B1=25$, $A2=4$, $B2=20$ length units. Two cylinder's heights are $ZCY=24.36$, $ACY2=33$ length units.

field is lower than that of the corner reflected field because in general a diffracted field is lower than a pure reflected field.

Figure 39 shows another diffracted-reflected mechanism that should be included in the calculation for the total field. This scattering mechanism, depending on the geometry of the two elliptic cylinders, has the possibility of producing fields of about the same magnitude as those shown for Figure 35. The reflected field from the flat top (deck) of the bottom cylinder can be easily calculated by using image theory, and the diffracted field off the top cylinder's curved wedge can again be calculated by Equation (12). It can be shown that, for the same antenna location, the diffraction point on the top cylinder's curved wedge has the same angular position - ϕ as that obtained for the corner reflected field shown in Figure 32. For the scattering geometry shown in Figure 39, the field versus the distance increments traveled by the antenna is shown in Figure 40. Since for the particular dimensions used here the top cylinder is too high for the narrow antenna beam to cover the diffraction and reflection points at the same instant, the field has relatively low amplitude. When the height of the top cylinder is reduced from 33 length units to 26 length units, the field is calculated again and is shown in Figure 41. This time the field has a much higher level and is comparable to that of Figure 38.

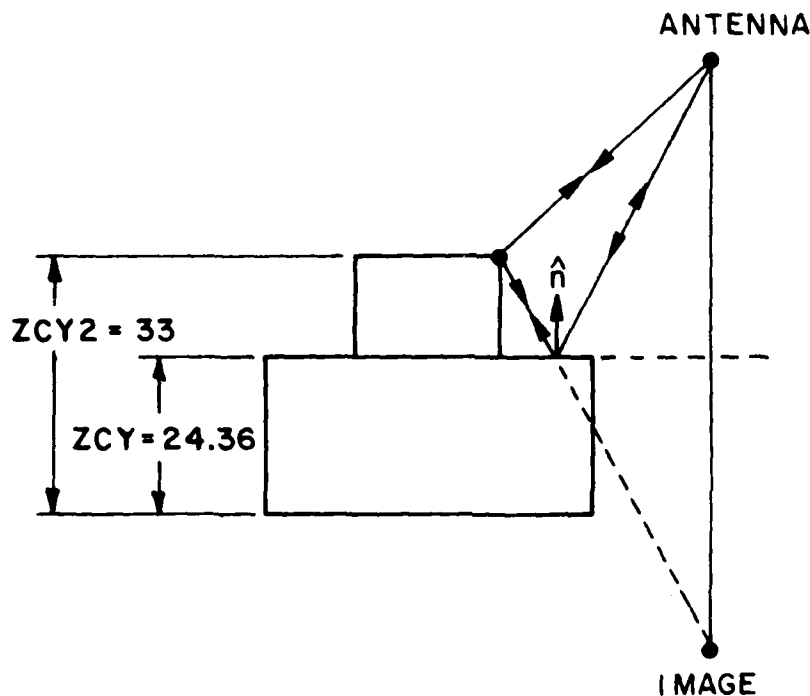


Figure 39. Diffracted-reflected field configuration.

Up to now, all the significant scattering mechanisms for the ship and the sea have been calculated separately; in the next chapter the solutions will be combined to form the total received field.

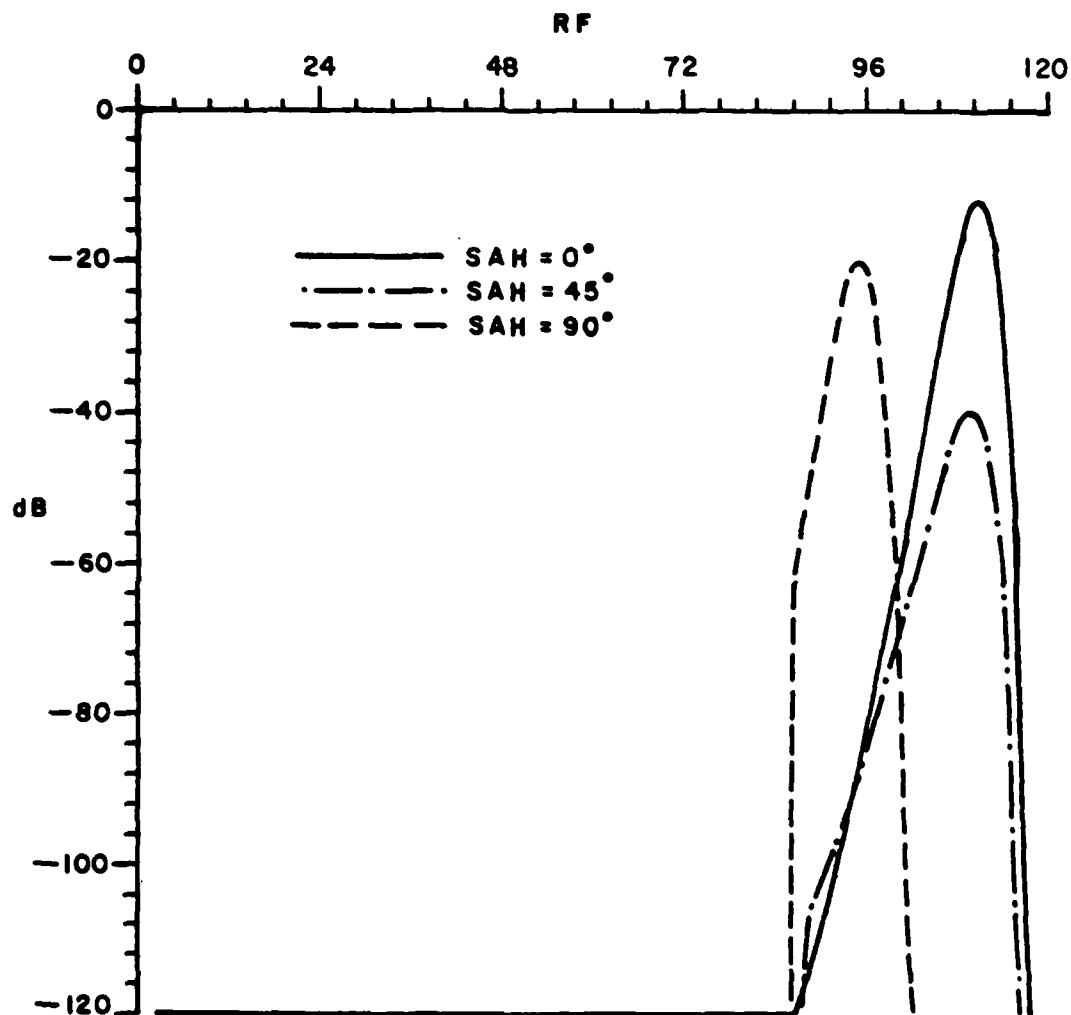


Figure 40. The diffracted-reflected field between two elliptic cylinders for the geometry shown in Figure 30. $7CY=24.36$, $ACY2=33$. Antenna depression angle= 60° . Ship's center is located at $RF=120$ length units. Ship's dimensions are $A1=5$, $B1=25$, $A2=4$, $B2=20$ units.

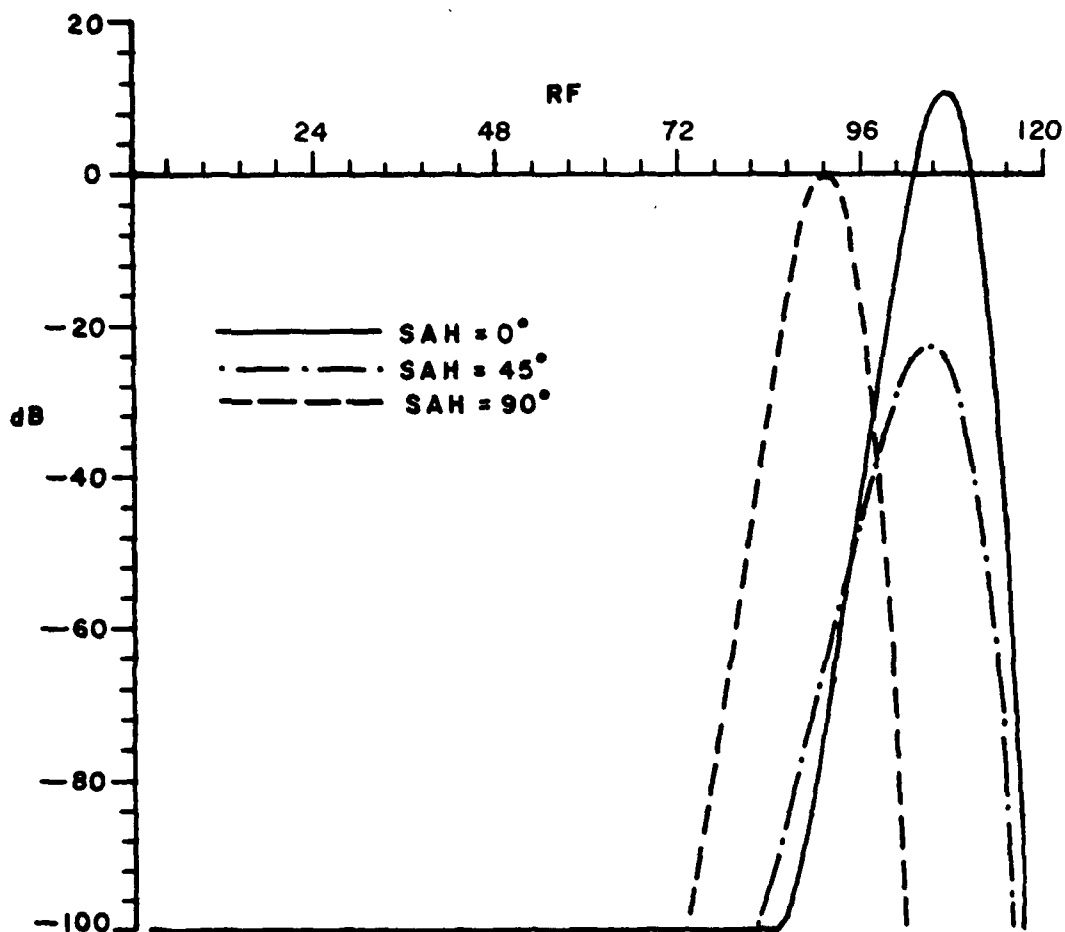


Figure 41. The diffracted-reflected field between two elliptic cylinders for the geometry shown in Figure 39. ZCY=24.36 ZCY2=26. Antenna beam depression angle = 60° . Ship's dimensions are A1=5, B1=25, A2=4, B2=20 units.

CHAPTER VII COMBINED SOLUTIONS WITH A CONICAL SHIP HULL AND DIFFERENT ANTENNA PATTERNS

Thus far the basic scattering mechanisms of the ship and sea have been analyzed individually, and it has been found that there are three dominant scattered signatures from the ship-sea model. It is worthwhile, at this point, to briefly summarize them as follows:

1. Backscattered signatures from the sea surface: Both the gravity waves and capillary waves may contribute significantly to the backscattered signature.
2. Double-bounce signature between the ship and sea: The forward scattered (bistatic) signature from the sea surface is predominantly governed by the scattering from gravity waves. The reflected field from the ship's hull (elliptic cylinder) is calculated from Equation (1).
3. Ship scattered signatures: There are two major contributions from the two-elliptic cylinders. These are the corner reflected and diffracted-reflected signatures.

By summing the above signatures or simply by adding together the signatures (with proper phase addition) in Figures 26 through 28 with those in Figures 34, 38 and 40, one obtains the total received fields produced by the ship-sea model, which are illustrated in Figures 42, 43 and 44. The geometrical configuration of the ship and the antenna trajectory is shown in Figure 33. For broadside incidence ($SAH=0^\circ$), the signature as shown in Figure 42 has a very strong ship-scattered term which is about 30 dB above the average sea clutter signal. For the same trajectory incident angle, the ship-sea double-bounce signal (which occurs at an earlier time than the ship scattered signal) has a peak level of about 10 dB above the sea clutter. When the antenna has an approach angle of 45° as shown in Figure 43, the ship scattered and ship-sea double-bounce signals have both disappeared into the sea clutter signal. For the head-on ($SAH=90^\circ$) signature as shown in Figure 44, the ship scattered signal has again become very strong, but the ship-sea double bounce signal is barely detectable, being only a few decibels above the sea clutter. Since all the above behavior has been interpreted previously in section (V-D) and (VI-A), no further comment is required here.

In this chapter we consider a further elaboration of the ship model in which the hull structure is modified from an elliptic cylinder to the physically more realistic shape of an elliptic cone.

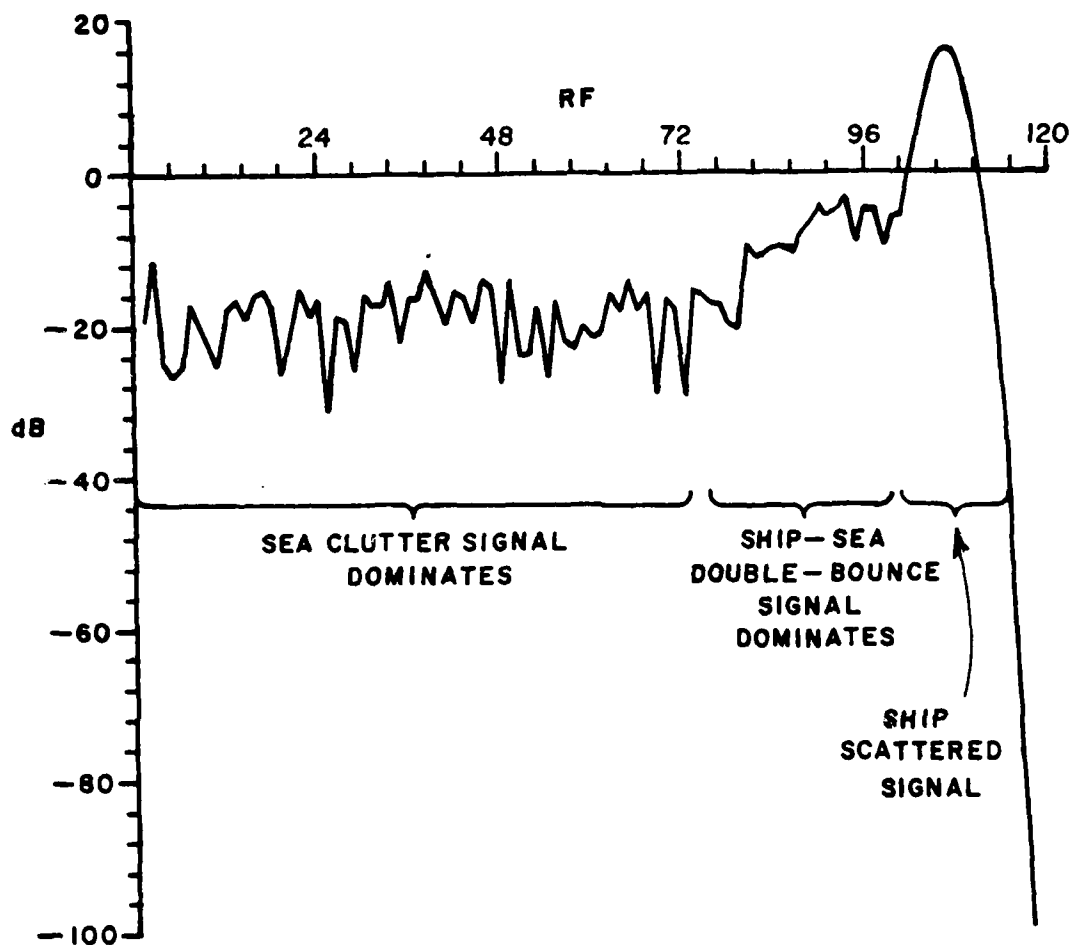


Figure 42. Total received field calculated when ship is represented by two elliptic cylinders. Geometry for the ship and antenna trajectory is shown in Figure 33. $A_1=5$, $B_1=25$, $A_2=4$, $B_2=20$, $A/A=60^\circ$, $A_T=0^\circ$, $ZF=40.5$, $SAH=0^\circ$. Ship's center is located at $RF=120$ length units with RF being the distance traveled by the antenna from its starting location.

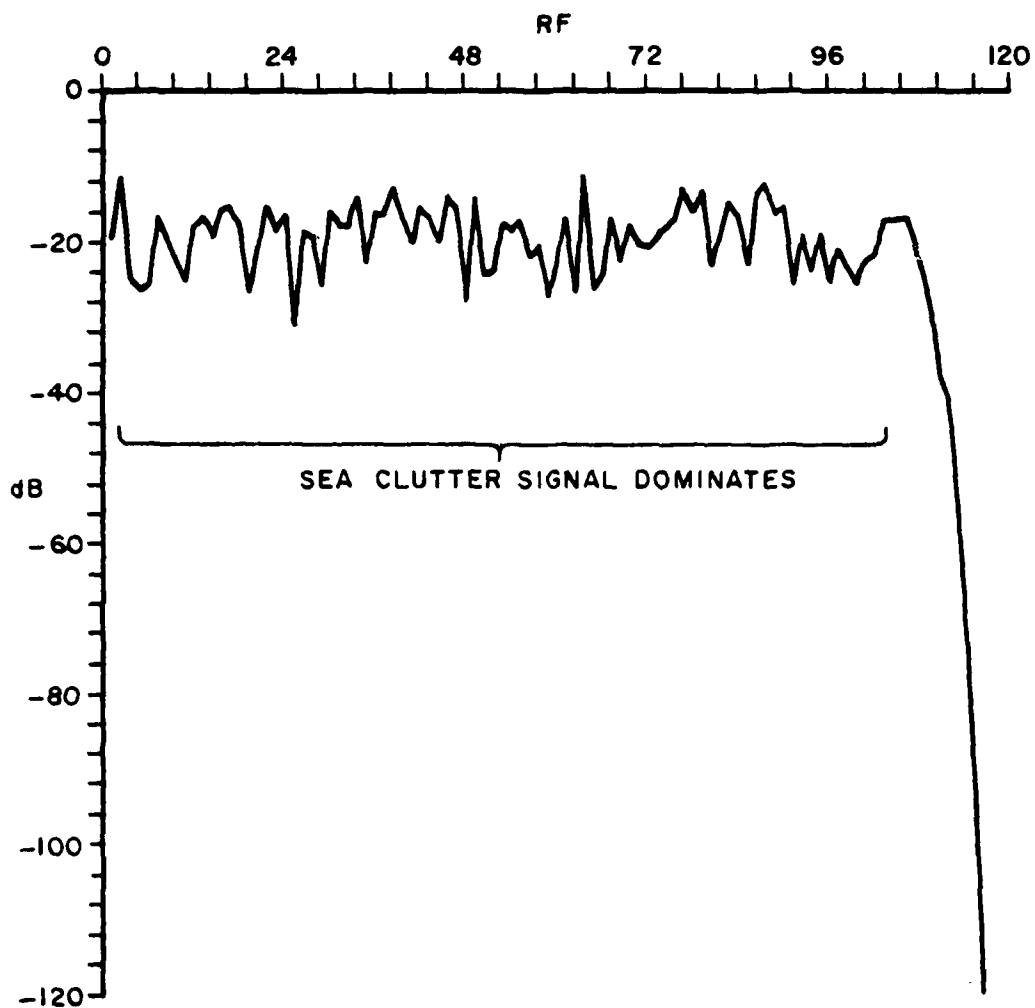


Figure 43. Ship-sea scattered signature for the same geometrical configuration as that for Figure 42 except that $SAH=45^\circ$.

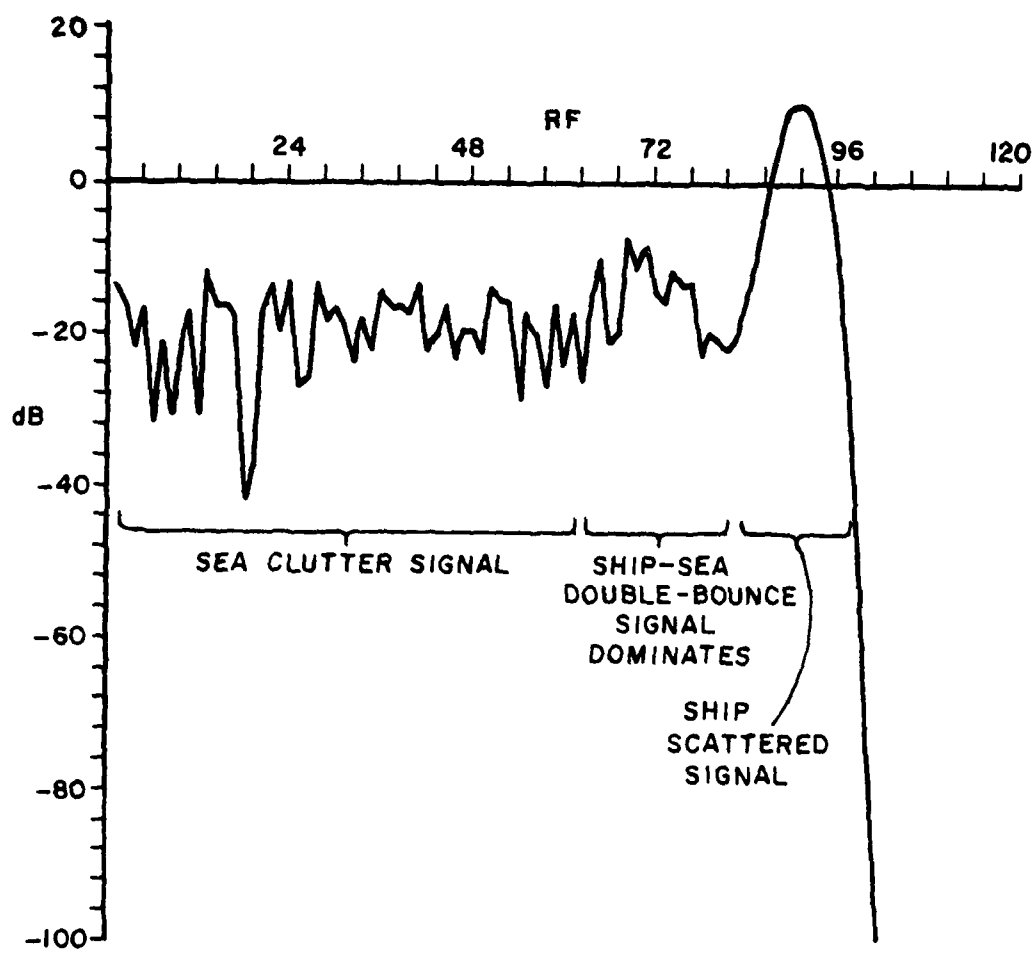


Figure 44. Ship-sea scattered signature for the same geometrical configuration as that for Figure 42 except that $SAH=90^{\circ}$.

In this form, the model is versatile enough to simulate the major scattering contributors of wide variety of ships. In addition, we wish to use a different antenna radiating characteristic so that the effect of antenna pattern on the signatures can also be studied. The geometrical configuration of the antenna trajectory and the new ship model resulting from the modification of the hull structure is shown in Figure 45. It is clear that the only scattered signal to be re-calculated due to this modification is the double bounce ship-sea interaction term. Consequently the numerical search technique for finding the reflection points must be modified and the GTD calculation for the reflected field from an elliptic cone must be obtained.

It is interesting to see first how the numerical search technique for an elliptic cone differs from that for an elliptic cylinder. For a general elliptic cone as shown in Figure 46, the locus of its surface is described by the vector

$$\vec{r} = (z+k)\tan\theta_1 \cos v \hat{x} + (z+k)\tan\theta_2 \sin v \hat{y} + z \hat{z} \quad (44)$$

where v is related to the ϕ angle in the x - y plane measured counter-clockwise from the x -axis; θ_1 , θ_2 and k are illustrated in Figure 46. (Note that θ_1 and θ_2 are different from those used in previous chapters and k is not the electromagnetic wave number).

The two principal tangents on the surface are, with \vec{r} defined in Equation (44),

$$\vec{r}_z = \frac{\partial \vec{r}}{\partial z} = \tan\theta_1 \cos v \hat{x} + \tan\theta_2 \sin v \hat{y} + \hat{z} \quad (45a)$$

$$\vec{r}_v = \frac{\partial \vec{r}}{\partial v} = -(z+k)\tan\theta_1 \cos v \hat{x} + (z+k)\tan\theta_2 \sin v \hat{y} \quad (45b)$$

The normal to the surface is

$$\begin{aligned} \hat{n} &= \vec{r}_v \times \vec{r}_z = n_x \hat{x} + n_y \hat{y} + n_z \hat{z} \\ &= \tan\theta_2 \cos v \hat{x} + \tan\theta_1 \sin v \hat{y} - \tan\theta_1 \tan\theta_2 \hat{z} \end{aligned} \quad (46)$$

The source location is on the surface of the sea and can be denoted by (x_s, y_s) . The observation point at the receiver is located at (x_o, y_o, z_o) . Therefore, the incident vector can be given by

$$\begin{aligned} \vec{I} &= I_x \hat{x} + I_y \hat{y} + I_z \hat{z} \\ &= [(z_R+k)\tan\theta_1 \cos v - x_s] \hat{x} + [(z_R+k)\tan\theta_2 \sin v - y_s] \hat{y} + z_R \hat{z}, \end{aligned} \quad (47)$$

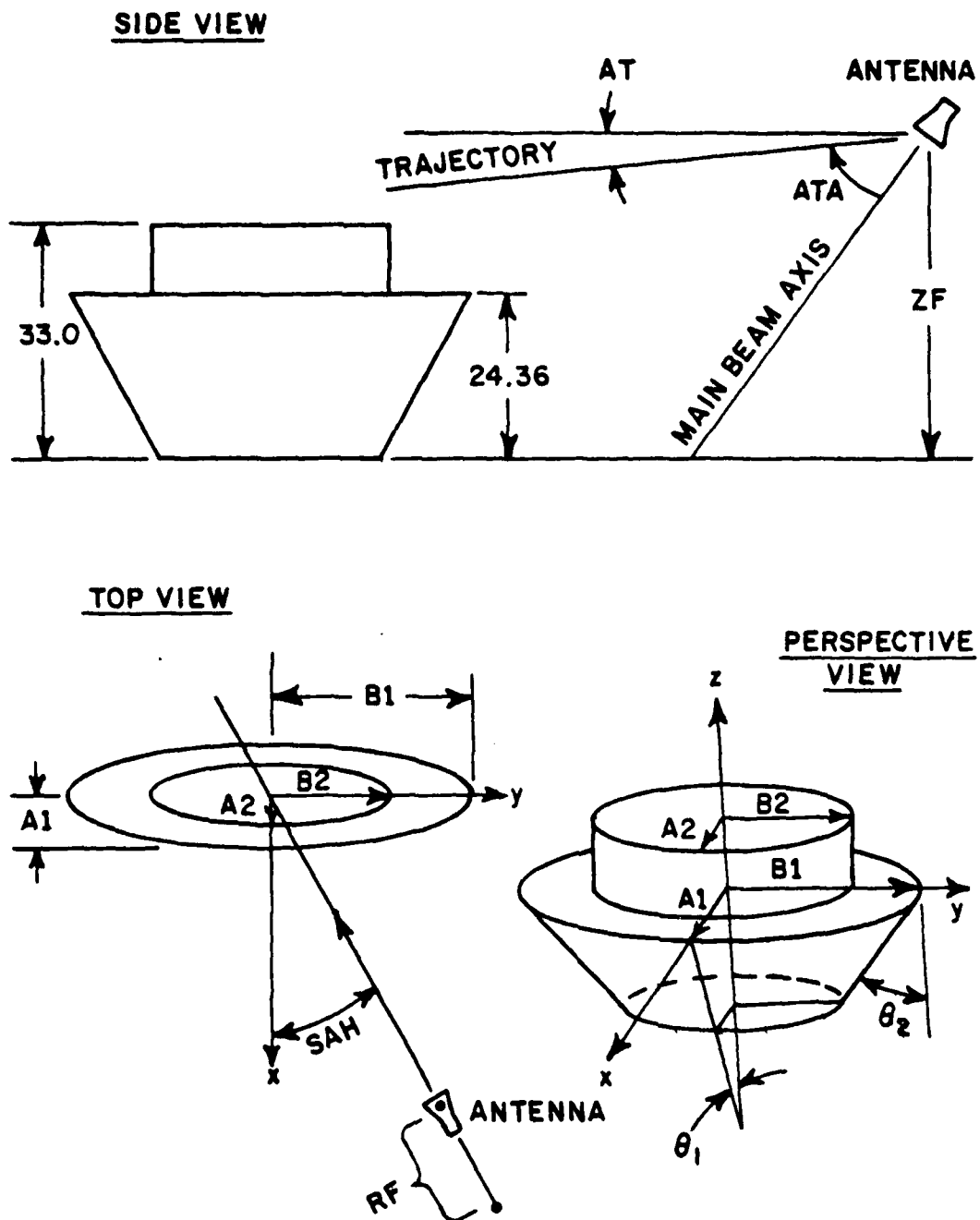


Figure 45. Geometrical configuration of the ship and antenna trajectory. The ship's hull is an elliptic cone.

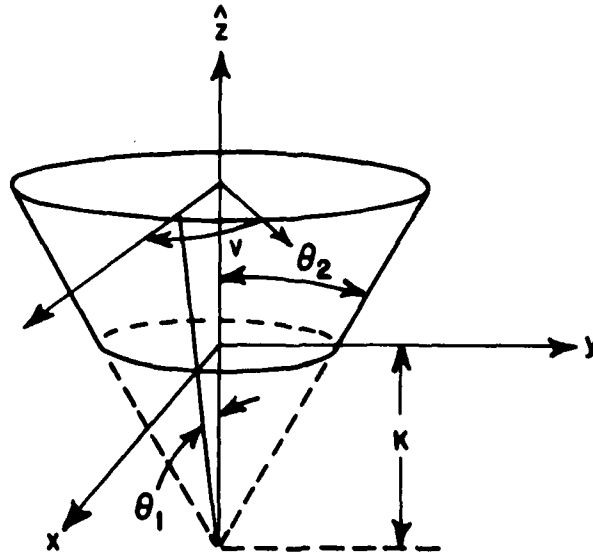


Figure 46. Elliptic cone configuration.

and the reflection vector is given by

$$\begin{aligned}\vec{R} &= R_x \hat{x} + R_y \hat{y} + R_z \hat{z} \\ &= [x_0 - (z_R + k) \tan \theta_1 \cos v] \hat{x} + [y_0 - (z_R + k) \tan \theta_2 \sin v] \hat{y} + (z_0 - z_R) \hat{z}\end{aligned}\quad (48)$$

where (z_R, v) are the height and elliptic parameter, respectively, defining the reflection point on the elliptic cone. Again it is essential to satisfy the laws of reflection as given by

$$(\vec{n} \cdot \vec{I})(\vec{n} \times \vec{R}) + (\vec{n} \times \vec{I})(\vec{n} \cdot \vec{R}) = 0 \quad (49)$$

where

$$\begin{aligned}\vec{n} \cdot \vec{I} &= n_x I_x + n_y I_y + n_z I_z \\ \vec{n} \times \vec{I} &= (n_y I_z - n_z I_y) \hat{x} + (n_z I_x - n_x I_z) \hat{y} + (n_x I_y - n_y I_x) \hat{z} \\ \vec{n} \times \vec{R} &= (n_y R_z - n_z R_y) \hat{x} + (n_z R_x - n_x R_z) \hat{y} + (n_x R_y - n_y R_x) \hat{z} \\ \vec{n} \cdot \vec{R} &= n_x R_x + n_y R_y + n_z R_z\end{aligned}$$

Equation (49) can thus be written as

$$(f_1) \hat{x} + (f_2) \hat{y} + (f_3) \hat{z} = 0$$

with

$$\begin{aligned}
 f_1 &= (n_x R_x + n_y R_y + n_z R_z)(n_y I_z - n_z I_y) + (n_x I_x + n_y I_y + n_z I_z)(n_y R_z - n_z R_y) = 0 \\
 f_2 &= (n_x R_x + n_y R_y + n_z R_z)(n_z I_x - n_x I_z) + (n_x I_x + n_y I_y + n_z I_z)(n_z R_x - n_x R_z) = 0 \\
 f_3 &= (n_x R_x + n_y R_y + n_z R_z)(n_x I_y - n_y I_x) + (n_x I_x + n_y I_y + n_z I_z)(n_x R_y - n_y R_x) = 0
 \end{aligned}
 \tag{50}$$

After substituting Equations (46), (47) and (48) into (50), one finds that f_1 , f_2 and f_3 are all functions of (v, z_R) , (x_s, y_s) and (x_o, y_o, z_o) with v and z_R as the two unknown variables. Since there are three equations with only two unknowns, one need only be concerned with two out of the three equations. However, in order to ensure that all the aspects of the reflection process have been considered, it is helpful to combine two of the three equations (since these are linearly dependent functions). Thus it is arbitrarily chosen to have

$$\begin{aligned}
 f_{12} &= f_1 + f_2 = 0 \\
 f_3 &= 0
 \end{aligned}
 \tag{51}$$

Once again, as shown in sections (V-A) and (VI-B), the Taylor Series expansion can be applied to Equation (51) with the result given by

$$\begin{bmatrix} \delta v \\ \delta z_R \end{bmatrix} = \begin{bmatrix} \frac{\partial f_{12}}{\partial v} & \frac{\partial f_{12}}{\partial z_R} \\ \frac{\partial f_3}{\partial v} & \frac{\partial f_3}{\partial z_R} \end{bmatrix}^{-1} \begin{bmatrix} AF \\ BF \end{bmatrix}
 \tag{52}$$

$$\text{where } AF = -f_{12} - \frac{\partial f_{12}}{\partial x_s} \delta x_s - \frac{\partial f_{12}}{\partial y_s} \delta y_s - \frac{\partial f_{12}}{\partial x_o} \delta x_o - \frac{\partial f_{12}}{\partial y_o} \delta y_o - \frac{\partial f_{12}}{\partial z_o} \delta z_o$$

$$BF = -f_3 - \frac{\partial f_3}{\partial x_s} \delta x_s - \frac{\partial f_3}{\partial y_s} \delta y_s - \frac{\partial f_3}{\partial x_o} \delta x_o - \frac{\partial f_3}{\partial y_o} \delta y_o - \frac{\partial f_3}{\partial z_o} \delta z_o.$$

Equation (52) enables one to calculate the shift of the reflection point $(\delta v, \delta z_R)$ resulting from the incremental distance change of

the source point $(\delta x_s, \delta y_s)$ or the observation point $(\delta x_o, \delta y_o, \delta z_o)$. Once again, before employing Equation (52), one needs to find the initial reflection point (v, z_R) in order to start the search. In Chapter V, the polynomial technique was used to find this initial point for the elliptic cylinder. In the case of an elliptic cone, it is found that the polynomial technique is much too complicated since it involves solving two equations with two unknowns. However, if one places both observation and source points on the x-axis as shown in Figure 47, it can be immediately determined that angle v is equal to zero and that the location z_R is given by the equation

$$z_R = (x' - b) \sin \theta_1 \cos \theta_1.$$

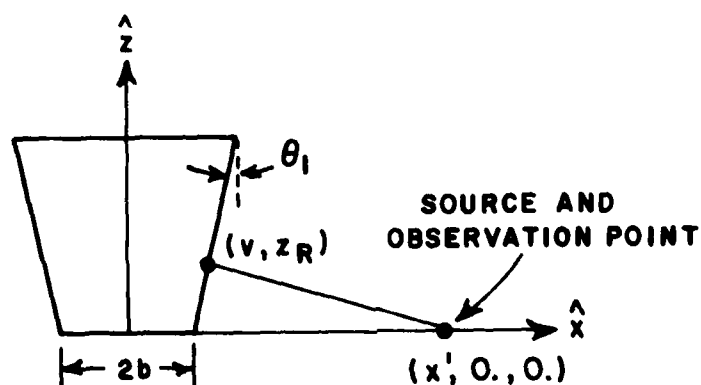


Figure 47. Initial location of (v, z_R) on the elliptic cone for the numerical search technique.

Once the reflection point on the elliptic cone has been initialized, it can be tracked along the surface to that reflection point which corresponds to the actual locations of the source and observation points, and thereby the reflected field can also be computed. The same equations that were used to calculate the reflected field from an elliptic cylinder can again be used here for the elliptic cone. The only difference is that one of the principal radii of curvature of the elliptic cone needs to be re-calculated. The principal radii of curvature are the surface radii which lie in the principal planes that contain the vector normal to the surface. In the case of an elliptic cone, one of the principal radii is infinite, and the other is given by

$$RG = - \frac{E + 2F(\partial z_R / \partial v) + G(\partial z_R / \partial v)^2}{e + 2f(\partial z_R / \partial v) + g(\partial z_R / \partial v)^2} \quad (53)$$

where

$$\begin{aligned} E &= \vec{r}_v \cdot \vec{r}_v \\ F &= \vec{r}_z \cdot \vec{r}_v \\ G &= \vec{r}_z \cdot \vec{r}_z, \end{aligned} \quad (54)$$

here \vec{r}_v and \vec{r}_z are the two principal tangents on the surface and are given by Equation (45),

$$\begin{aligned} e &= \vec{r}_{vv} \cdot \hat{n} \\ f &= \vec{r}_{zv} \cdot \hat{n} \\ g &= \vec{r}_{zz} \cdot \hat{n} \end{aligned} \quad (55)$$

with

$$\vec{r}_{vv} = \frac{\partial^2 \vec{r}}{\partial v^2}$$

$$\vec{r}_{zv} = \frac{\partial^2 \vec{r}}{\partial z \partial v}$$

$$\vec{r}_{zz} = \frac{\partial^2 \vec{r}}{\partial z^2}$$

where r is given by Equation (44).

If ∂l is the incremental distance on the surface in the x-y plane, one can show that

$$\begin{aligned} \frac{\partial z_R}{\partial v} &= \frac{\partial z_R}{\partial l} \cdot \frac{\partial l}{\partial v} \\ &= \frac{\sin v \cos v (\tan^2 \theta_1 - \tan^2 \theta_2)}{\sqrt{\tan^2 \theta_1 \sin^2 v + \tan^2 \theta_2 \cos^2 v + \tan^2 \theta_1 \tan^2 \theta_2 (\tan^2 \theta_2 \sin^2 v + \tan^2 \theta_1 \cos^2 v + 2)}} \\ &\quad \cdot \sqrt{(z+k)^2 \tan^2 \theta_1 \sin^2 v + (z+k)^2 \tan^2 \theta_2 \cos^2 v} \end{aligned} \quad (56)$$

After substituting the results from Equations (54), (55) and (56) into Equation (53), one is able to obtain the radius of curvature and, in turn, the reflected field from the elliptic cone using Equation (1). The validation of this calculated field is done by an experimental comparison as shown in Appendix D. A number of signatures for the geometry illustrated in Figure 45 have been computed and are shown in Figures 49, 50 and 51. All the dominant scattering mechanisms are included. It appears that no significant difference exists between the signatures for the elliptic cylinder and those for the elliptic cone.

One additional feature, besides the effects of the modified hull structure, that can be observed in these plots is that the ocean backscattered signature has been programmed beyond the ship's center. In other words, in the previous plots, all the signatures were calculated for an antenna position that starts at 120 length units from the ship's center and ends at the center of the ship. (However the sea scattered contribution was calculated only from the sub-areas in front of the ship.) Now, for the sake of completeness, the antenna starts to collect signature when it is 100 units from the ship's center and finishes it at 20 units beyond the ship's center, with backscattered contribution from the sub-areas that are behind the ship (see Figure 48).

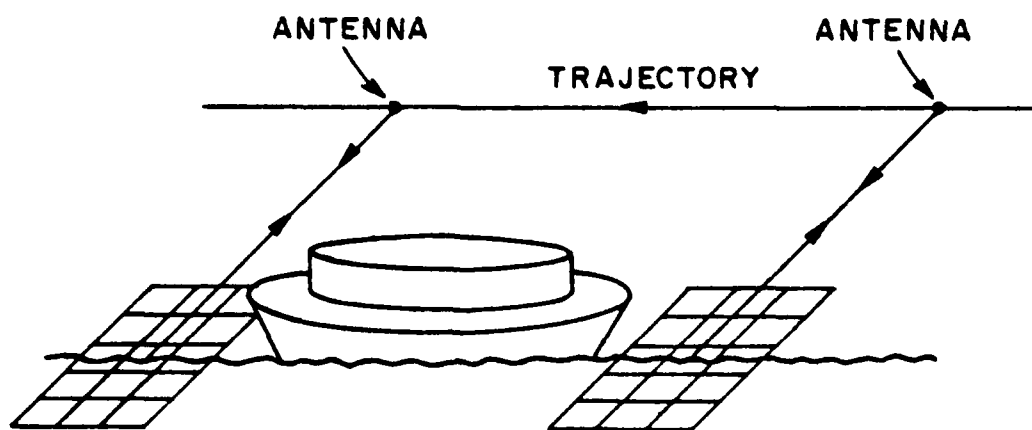


Figure 48. Configuration for sea scattered signature collected beyond the ship.

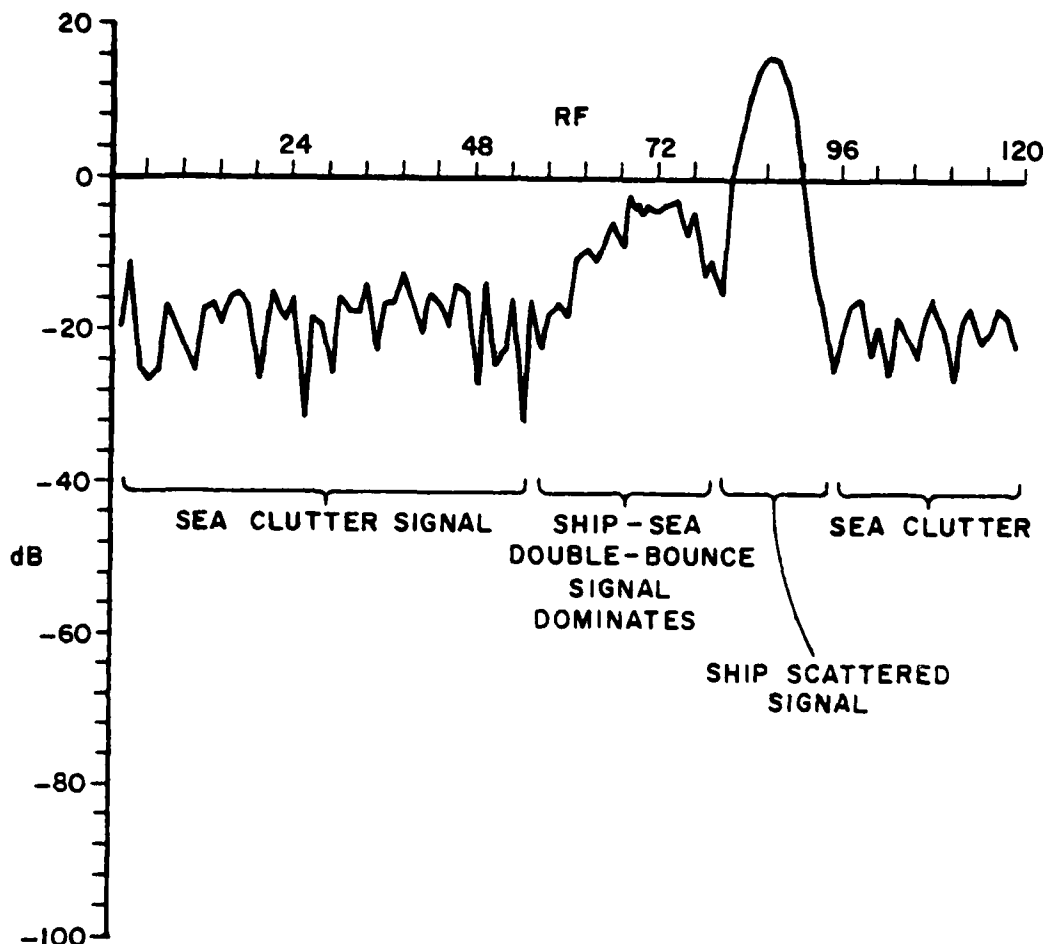


Figure 49. Total scattered signature for the ship with a conical hull. Signature is collected beyond the ship. Geometrical configuration is shown in Figure 45 with $\theta_1=4.7^\circ$ and $\theta_2=22.3^\circ$. Antenna approach angle $SAH=0^\circ$. Antenna beam depression angle $ATA=60^\circ$. Ship's center is located at $RF=100$ length units with RF being the distance traveled by the antenna from its starting location. Ship's dimensions are: $A1=5$, $B1=25$, $A2=4$, $B2=20$, $ZCY=24.36$, $ZCY2=33$ length units.

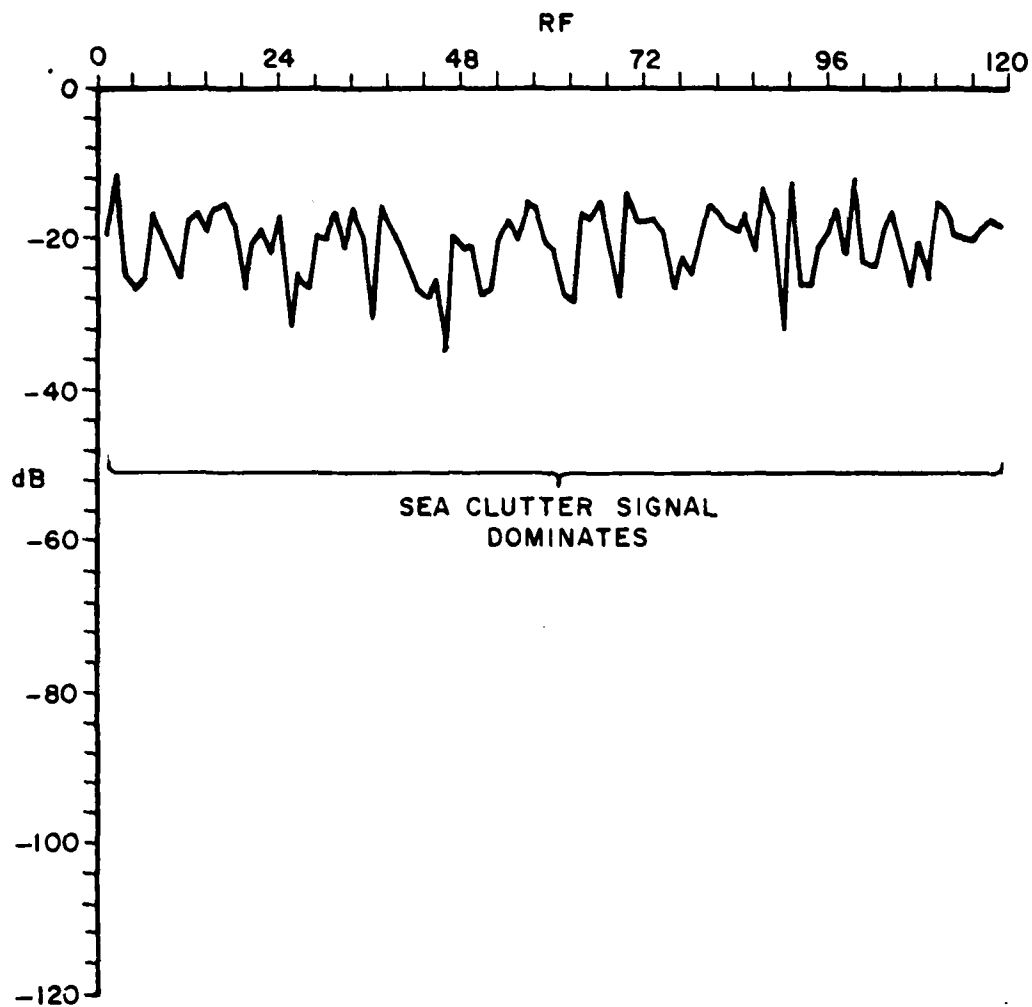


Figure 50. Total scattered signature for the ship with a conical hull. Same geometrical configuration as that for Figure 49 except the antenna approach angle $SAH=45^{\circ}$.

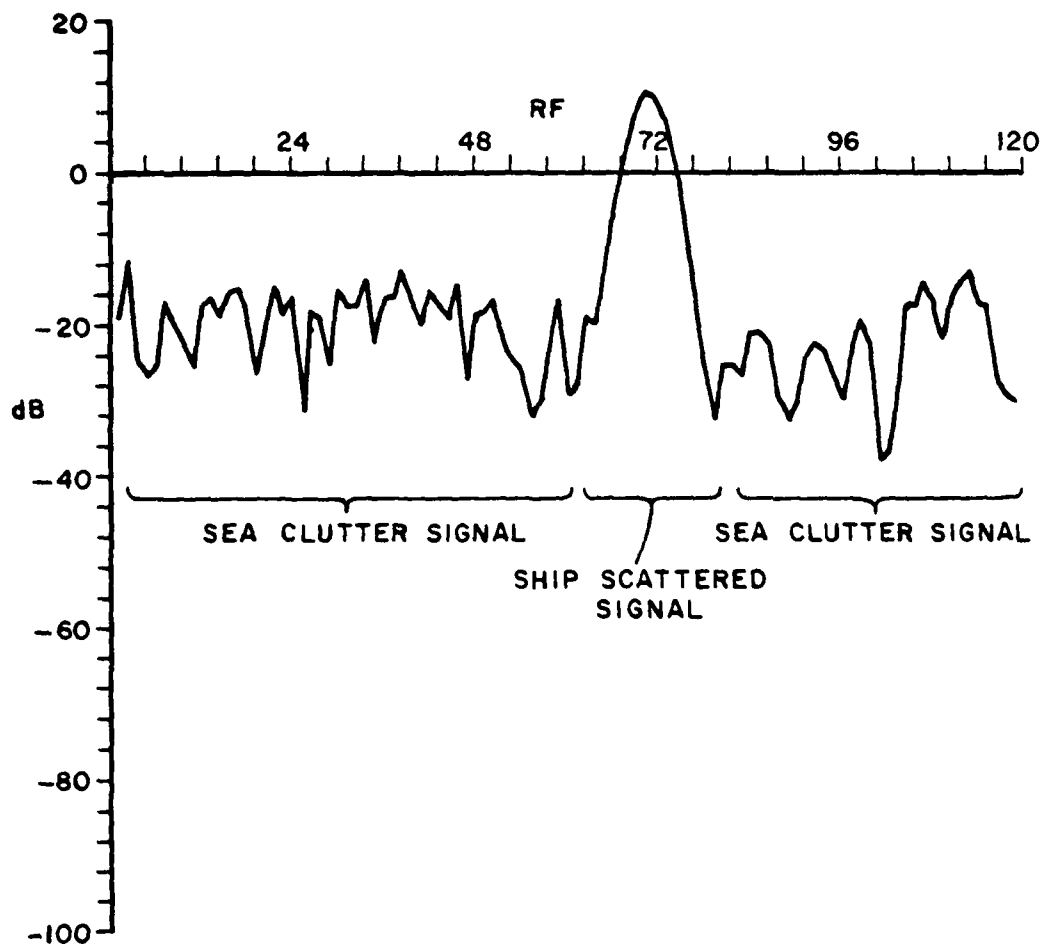


Figure 51. Total scattered signature for the ship with a conical hull. Same geometrical configuration as that for Figure 49 except the antenna approach angle $SAH=90^\circ$.

The antenna pattern can also play an important role in the form of the signature. Previously, the antenna pattern used was a 15-degree pencil beam, thus confining all the significant scattered power to be returned from only the small area illuminated by the narrow beam. It is interesting to see how the signatures change when a greatly broadened antenna beam is used. The new antenna radiating characteristic, as shown in Figure 52, has also a 15-degree Gaussian beam but it is transmitted conically around the antenna's trajectory. Thus looking down onto the ocean surface, the illuminated area has been greatly increased transverse to the trajectory direction. The analysis for the antenna radiation pattern must now be correspondingly changed.

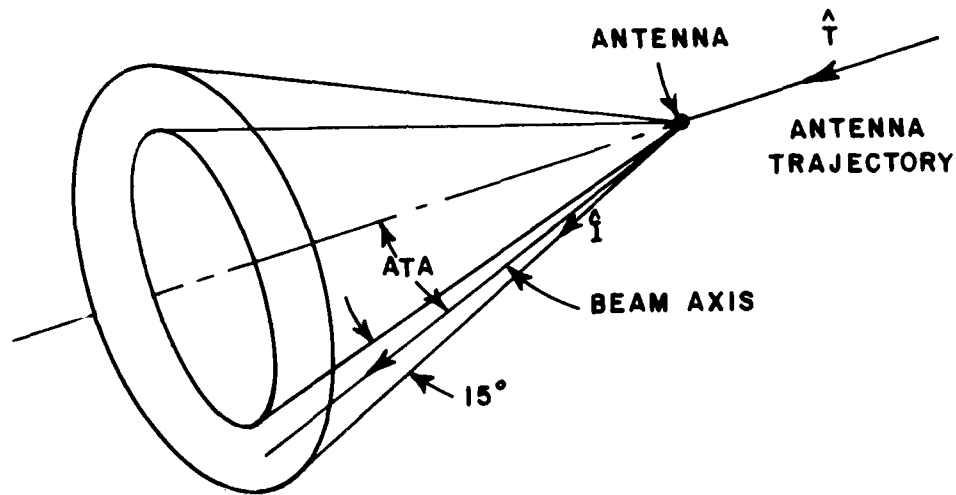


Figure 52. Conical antenna pattern.

If one denotes \hat{I} to be the arbitrary incident unit vector and \hat{T} to be the antenna trajectory direction, then the pattern angle θ from the trajectory direction is

$$\theta = \arccos(\hat{I} \cdot \hat{T}) \quad (57)$$

If ATA is the pattern cone half angle, then the far field pattern is assumed to have the form

$$E(\theta) = \frac{j\omega\mu}{4\pi r} J_0 a^2 e^{-jkr} e^{-\frac{|ka \cos(\theta-ATA)|^2}{4\pi}} \quad (58)$$

where "a" determines the beamwidth of the pattern, and $J_0 a^2 = 1$ is assumed in the computation.

When the elliptic-cone ship model is traversed with the new hollow-cone antenna pattern, one obtains the total ship-sea scattered signature shown in Figures 53, 54 and 55 for a cone half angle (ATA) of 60° . Signatures for the cone half angle of 30° are shown in Figures 56, 57 and 58. When comparing these signatures with those previously obtained for the antenna with a pencil beam, one significant difference can be observed. That is, when the pencil beam is used, the ship can not be detected for approach angles in the vicinity of 45° ; however, when the hollow-cone pattern is used, the ship contributes an observable backscattered signal no matter what may be the antenna approach angle. This is true for both the 30° and 60° cone half angles. Apparently, the beam is broad enough to pick up the major specular points on the ship even though it is not normally incident. Another noticeable difference is that the sea clutter signal for the conical antenna pattern is higher than that for the pencil beam pattern. This is true because more of the sea surface is being illuminated by the broadened antenna pattern. An additional anticipated feature observed in these plots is that when the cone half angle is 30° , the ship and ship-sea scattered signal occur much earlier than for the 60° cone half angle. This is because the main antenna beam reaches the ship much earlier when the angle ATA is 30° . The sea back-scattered signal is substantially lower when angle ATA is 30° , not only because the effective range has been increased but also because, at this angle, the backscattering cross section of the ocean decreases as the angle of incidence (from vertical) increases, particularly for horizontal polarization. The signatures illustrated in Figures 53 through 58 are for vertical polarization; keeping the same geometrical configurations, the signatures for horizontal polarization are illustrated in Figures 59 through 64.

Before concluding the analysis on the simplified ship-sea model, it is appropriate to repeat the calculation with a model that closely resembles a real ship. The ship U. S. S. Missouri is chosen, and a model of it is shown in Figure 65a. The simplified model with corresponding dimensions is illustrated in Figure 65b. The calculated signatures for this model with the same trajectory and geometrical configuration as that illustrated in Figure 45 are shown in Figures 66 through 71. The trajectory altitude is 200 length units, and the hollow cone antenna pattern is used. The signature sampling increment along the trajectory is 3 length units, and each sub-area of the sea surface has a width of 6 length units. The number of sub-areas is 21 by 13 with 21 sub-areas located transverse to the trajectory direction. With pattern cone half-angle of 60° , the three different signatures in Figures 66 through 68 correspond to three different antenna approach angles. The signatures in Figures 69 through 71 represent the signatures for pattern cone half angle of 30° . The starting location (SRF) of the radar from the center of the ship has to vary drastically from one antenna approach

angle to another. This is caused by the substantial size difference between the top and bottom cylinders. For example, when the antenna has a broadside incidence ($SAH=0^\circ$), the ship-scattered and the ship-sea double-bounce signatures are very close to each other in space; however, when the antenna approaches head-on ($SAH=90^\circ$), the above two signatures are very far apart. Thus, in order to show both signatures on a single run, both the antenna starting location and the distance it travels need to vary depending on the antenna approach angle. It can be seen that the ship scattered signatures are easily detectable, independent of the antenna approach angle or the pattern cone half angle. The ship-sea double-bounce signature, however, is only detectable when the antenna approaches from broadside. This characteristic so far has not varied for any of the models that have been used in this report. It should be pointed out that the scattered signatures due to the ship alone is believed to be a very crude approximation to the real scattered signature. This is based on the fact that there are many substructures on the ship that can scatter energy. Figure 72 demonstrates that, to improve the simplified U. S. S. Missouri Model, several objects such as blocks, cylinders and plates should be added onto the decks of the ship. The GTD technique can still be effectively applied to find the scattering from such a complicated ship structure at the cost of some extra complexity in the computer program.

In actuality, the ship contribution to the signature from either the more complex model, or the real ship, will be considerably different in duration, magnitude, and structure from those shown in the preceding figures. Our modelling of the hull and sea surface is a reasonably good approximation to the real situation, and it may be expected that the clutter and double bounce signatures will be quite similar to those obtained here. It is most unlikely however that a real ship would exhibit the long expanse of unbroken deck and cabin wall needed to form the continuous corner reflector which is the major contributor to a ship signature. Instead, the corner would be broken up by obstructions and augmented by reflections from other structures, producing an irregular signature of somewhat longer duration (especially for a bow or stern approach). It is probable, however, that the real ship signature would not ever be significantly larger in magnitude than the largest signatures shown here, because single, double or triple bounce reflected fields are all essentially image fields. In any event, no attempt should be made to evaluate system performance on the basis of the signatures in this report, because of the misleading simplicity of the ship-alone component.

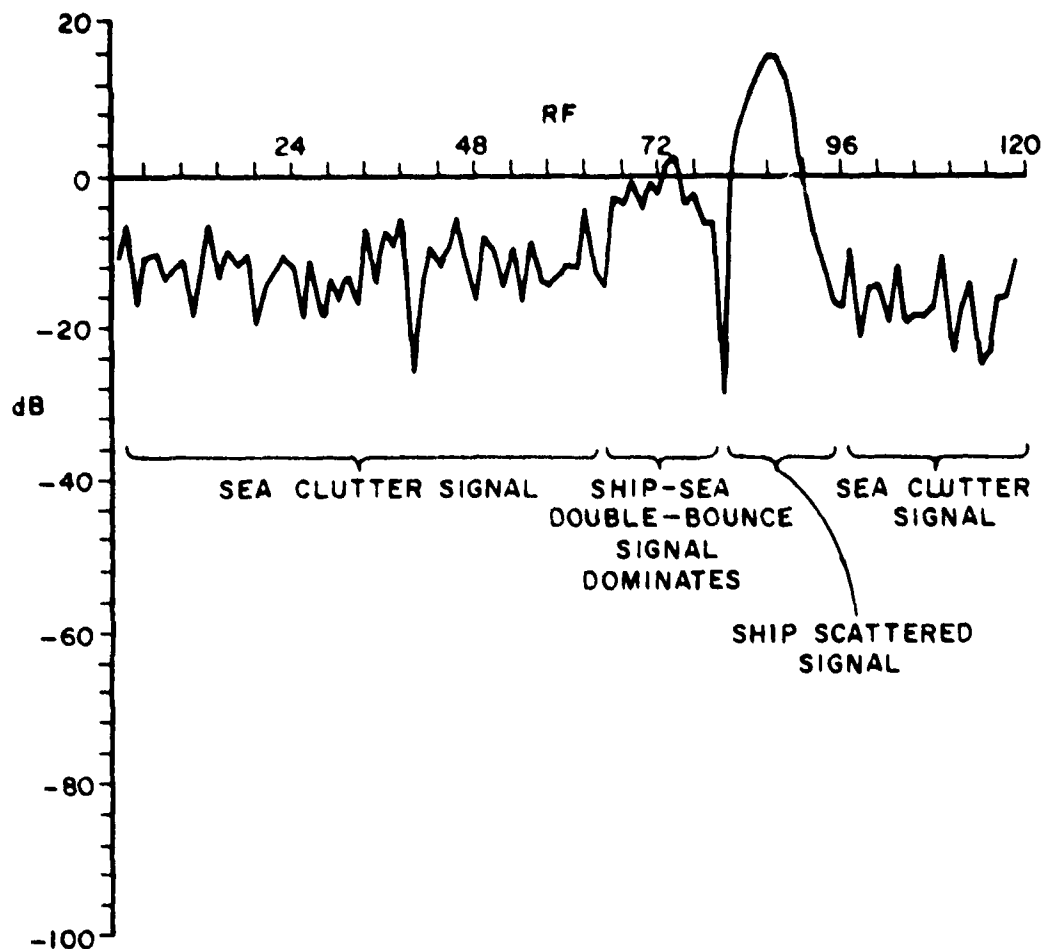


Figure 53. Total scattered signature from the sea and a ship with conical hull. Hollow cone antenna pattern is used. For the geometrical configuration of Figure 45, $SAH=0^\circ$. Antenna pattern cone half angle $ATA=60^\circ$. Ship's center is located at $RF=100$ length units with RF being the distance traveled by the antenna from its starting location. Ship's dimensions are $A1=5$, $B1=25$, $A2=4$, $B2=20$, $YC1=24, 36$, $YC2=33$ length units.

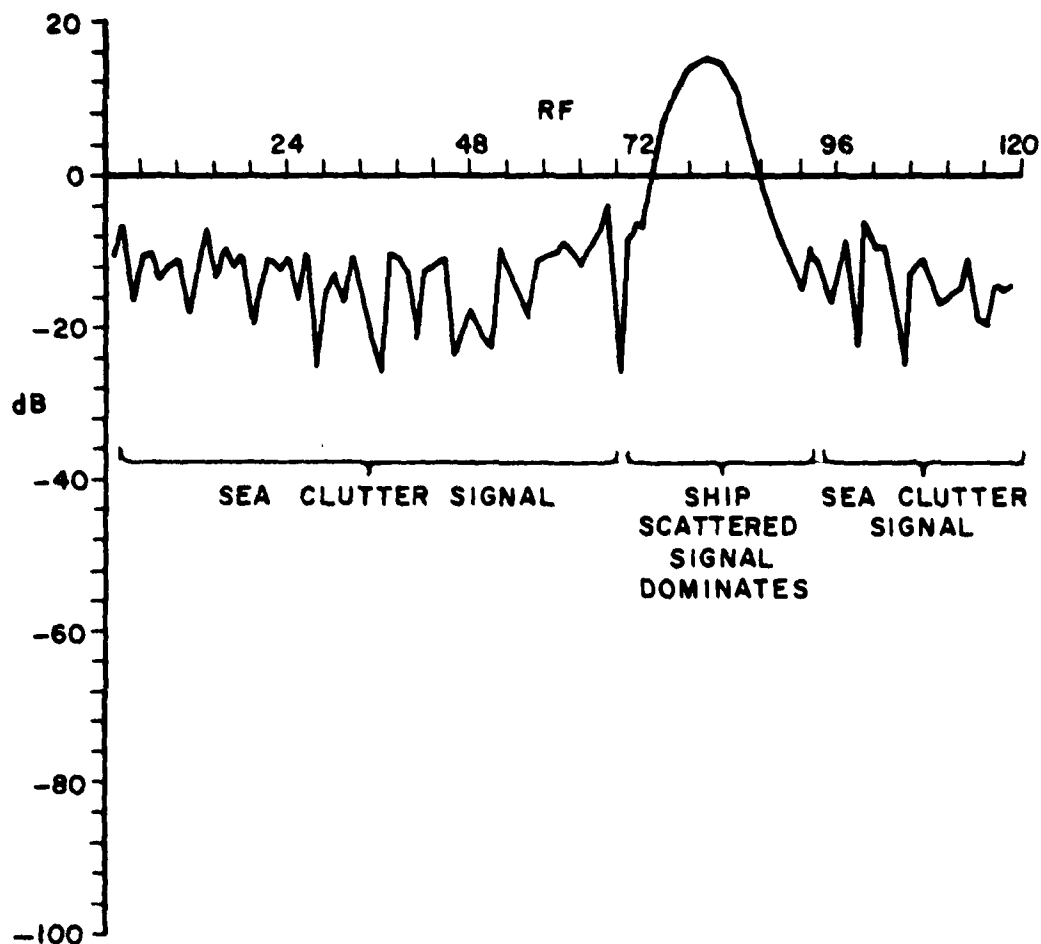


Figure 54. Total scattered signature from the sea and a ship with conical hull. Hollow cone antenna pattern is used. $SAH=45^\circ$, $ATA=60^\circ$. Other dimensions are the same as those shown in Figure 53.

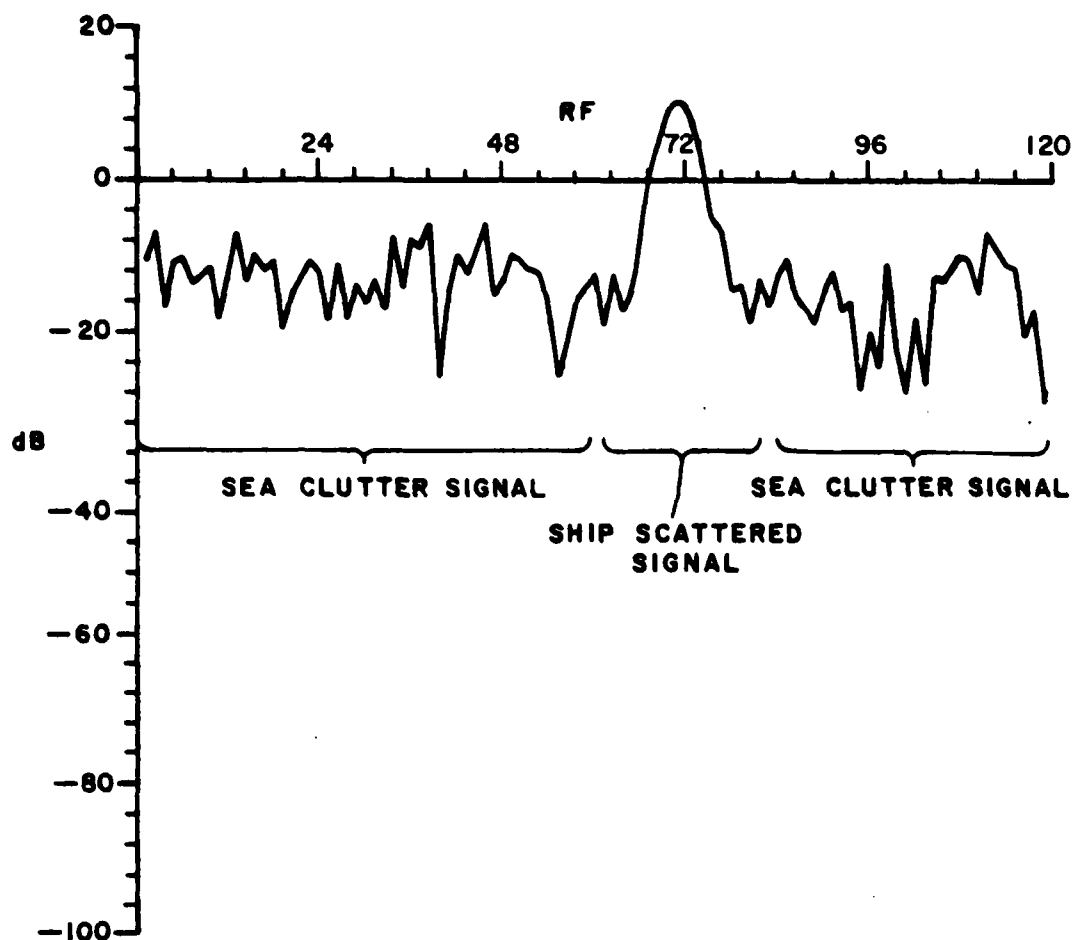


Figure 55. Total scattered signature from the sea and a ship with conical hull. Hollow cone antenna pattern is used. $SAH=90^\circ$, $ATA=60^\circ$. Other dimensions are the same as those shown in Figure 53.

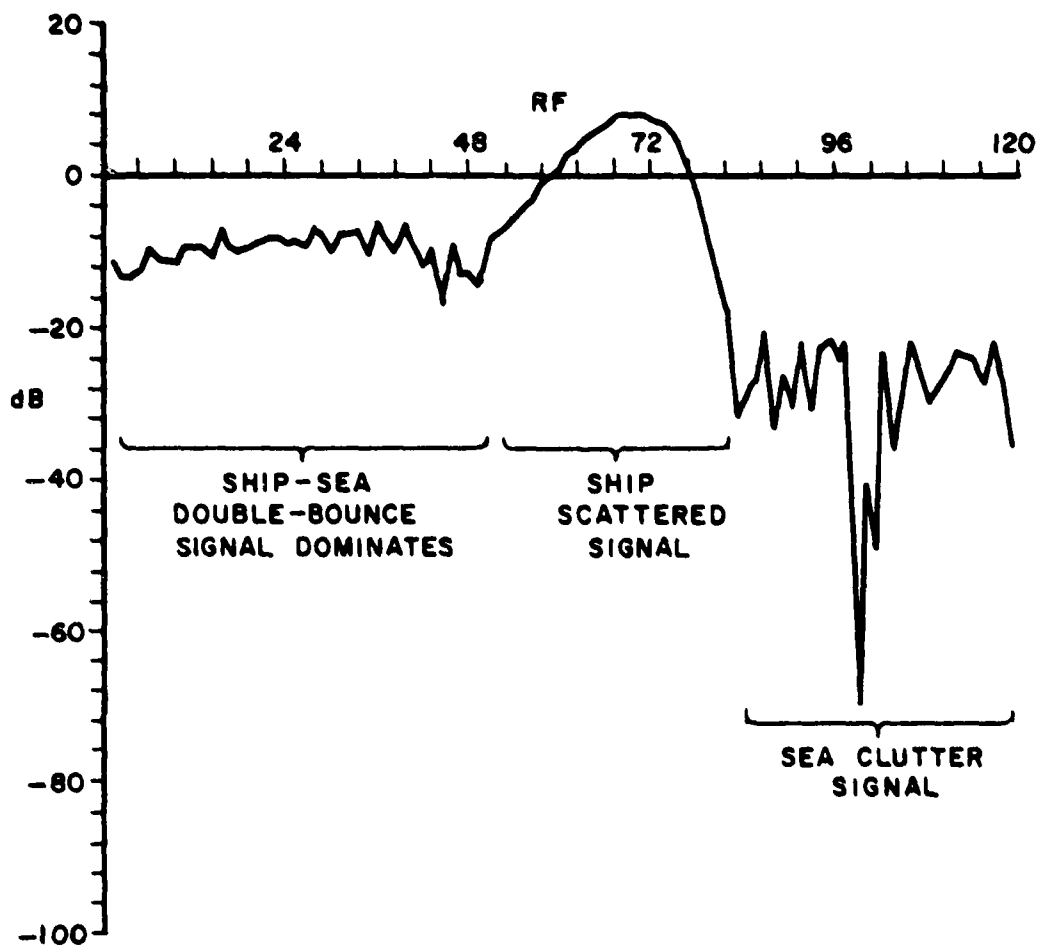


Figure 56. Total scattered signature for the same geometrical configuration as that for Figure 53. Here the antenna pattern cone half angle $ATA=30^{\circ}$. Antenna approach angle $SAH=0^{\circ}$.

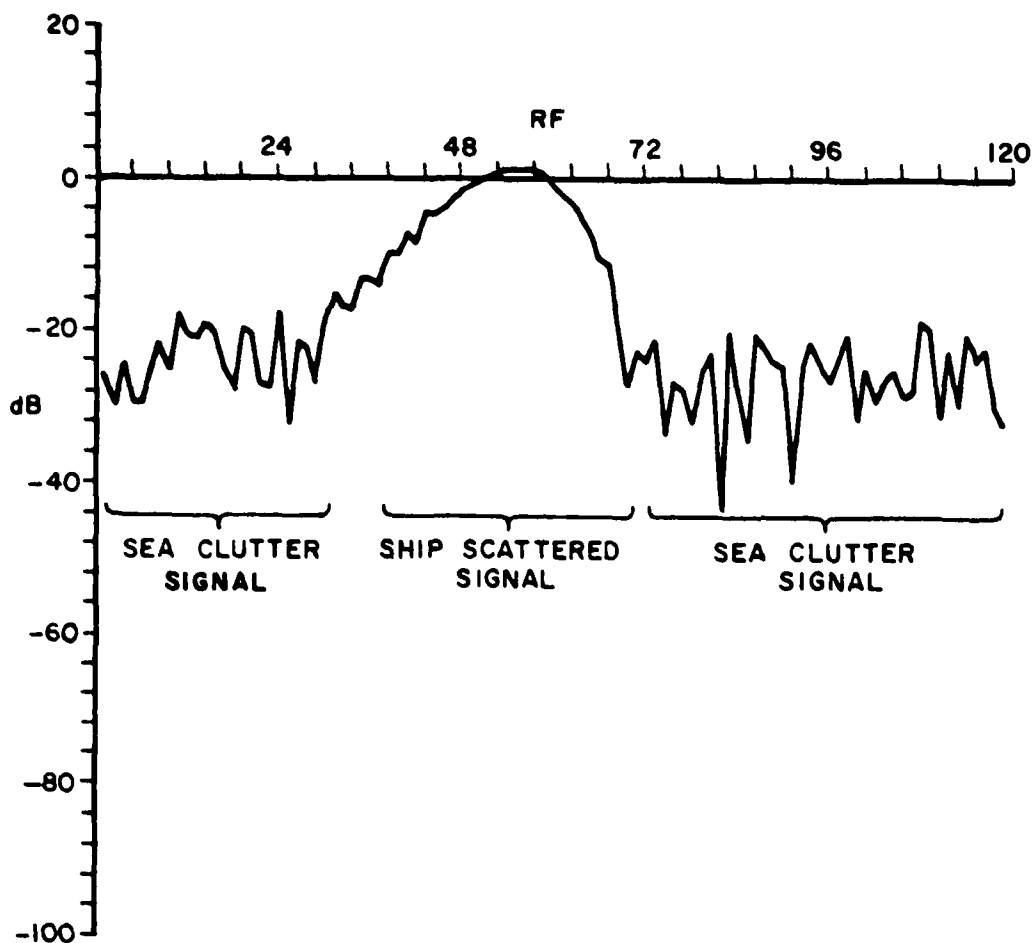


Figure 57. Total scattered signature from the sea and a ship with conical hull. Hollow cone antenna pattern is used. $SAH=45^\circ$, $ATA=30^\circ$. Other dimensions are the same as those shown in Figure 53.

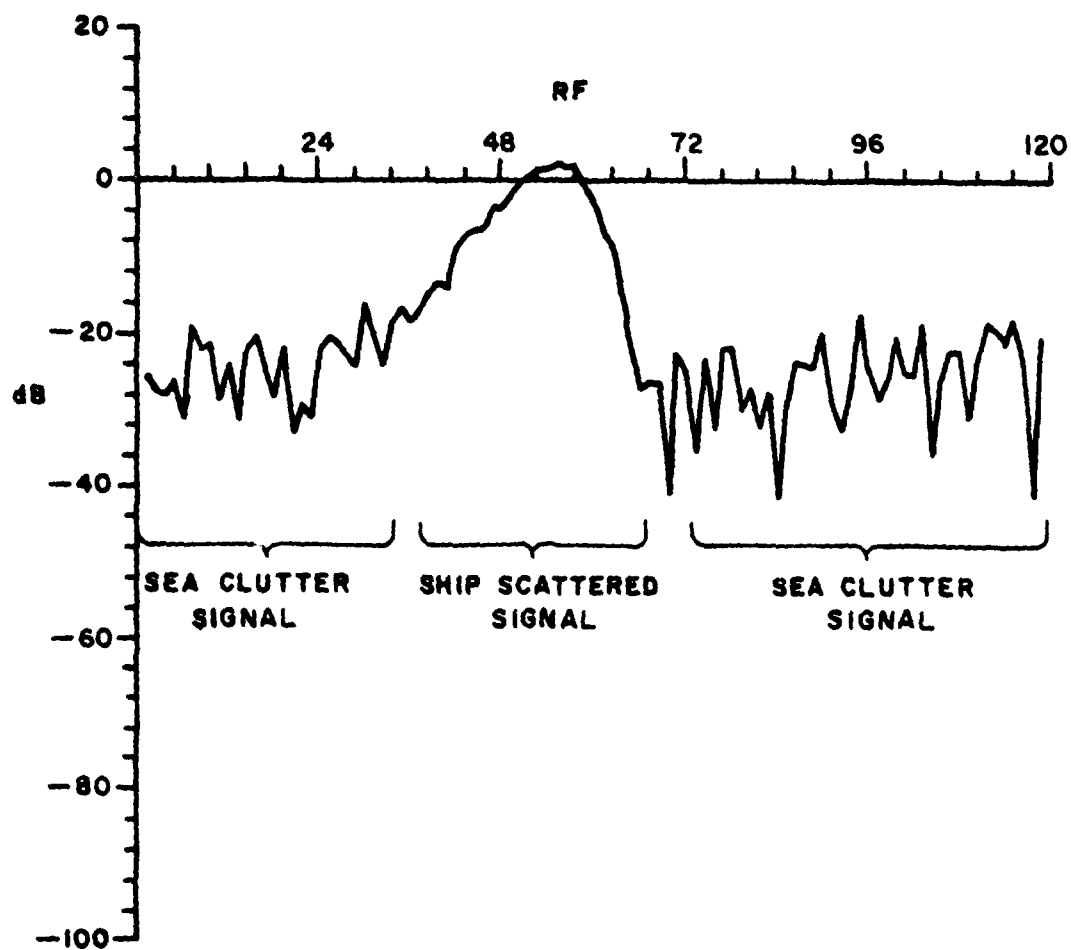


Figure 58. Total scattered signature from the sea and a ship with conical hull. Hollow cone antenna pattern is used. $SAH=90^{\circ}$, $ATA=30^{\circ}$. Other dimensions are the same as those shown in Figure 53.

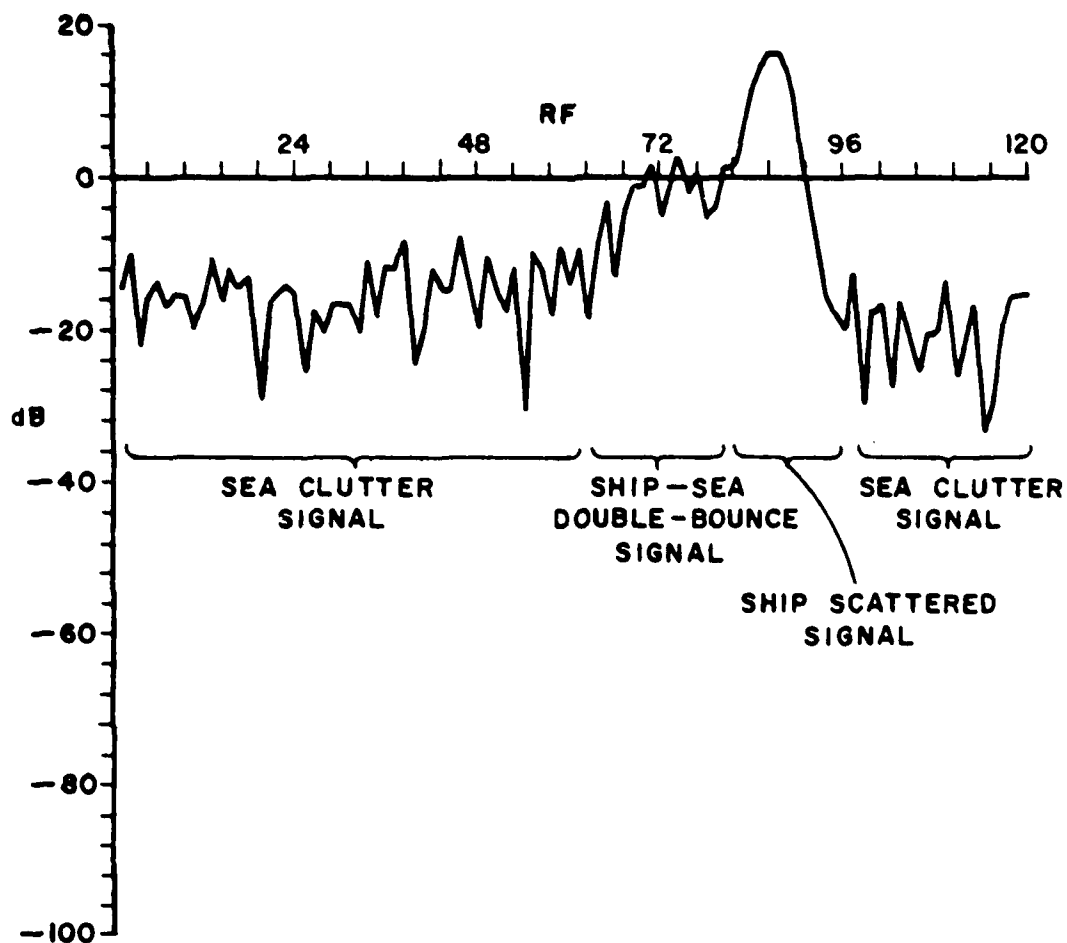


Figure 59. Total scattered signature from the sea and a ship with conical hull. Hollow cone antenna pattern is used. $SAH=0^\circ$, $ATA=60^\circ$, polarization is horizontal. Other dimensions are the same as those shown in Figure 53.

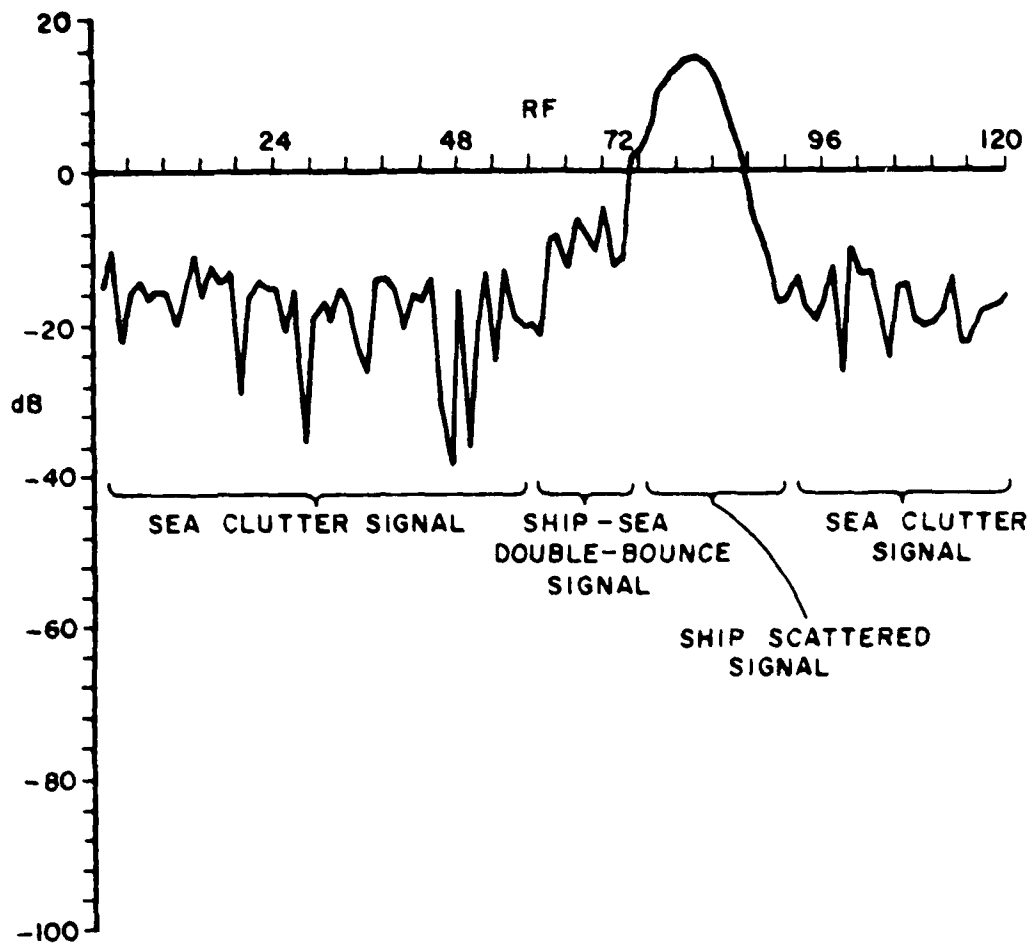


Figure 60. Total scattered signature from the sea and a ship with conical hull. Hollow cone antenna pattern is used. $SAH=45^\circ$, $ATA=60^\circ$, polarization is horizontal. Other dimensions are the same as those shown in Figure 53.

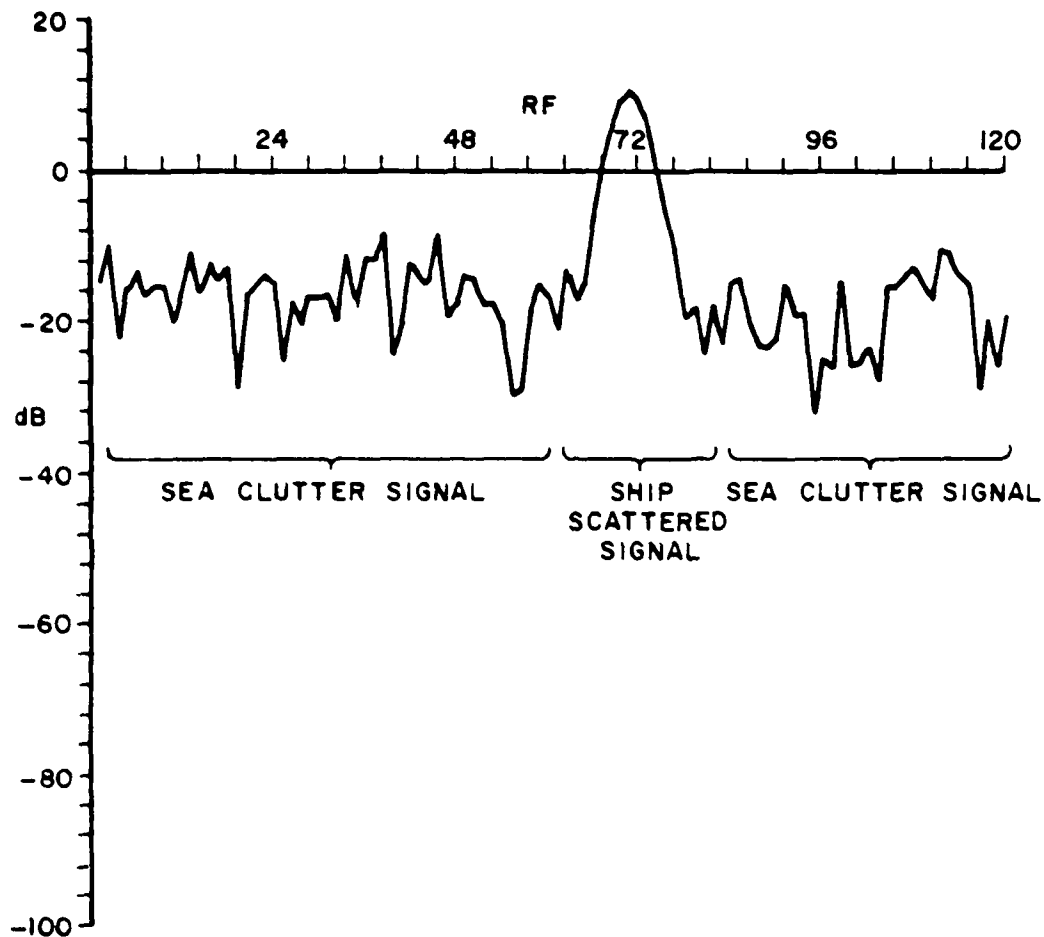


Figure 61. Total scattered signature from the sea and a ship with conical hull. Hollow cone antenna pattern is used.
 $SAH=90^\circ$, $ATA=60^\circ$, polarization is horizontal.
 Other dimensions are the same as those shown in Figure 53.

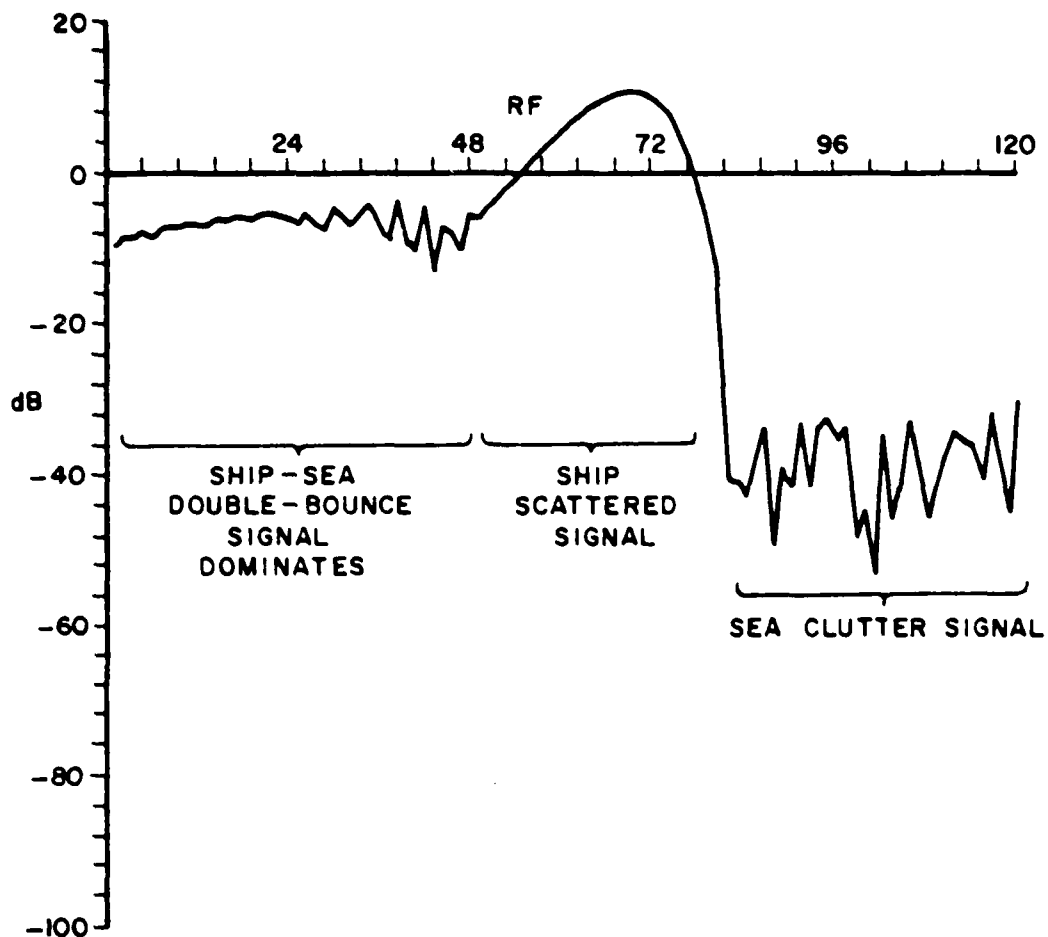


Figure 62. Total scattered signature from the sea and a ship with conical hull. Hollow cone antenna pattern is used.
 $SAH=0^{\circ}$, $ATA=30^{\circ}$, polarization is horizontal.
 Other dimensions are the same as those shown in Figure 53.

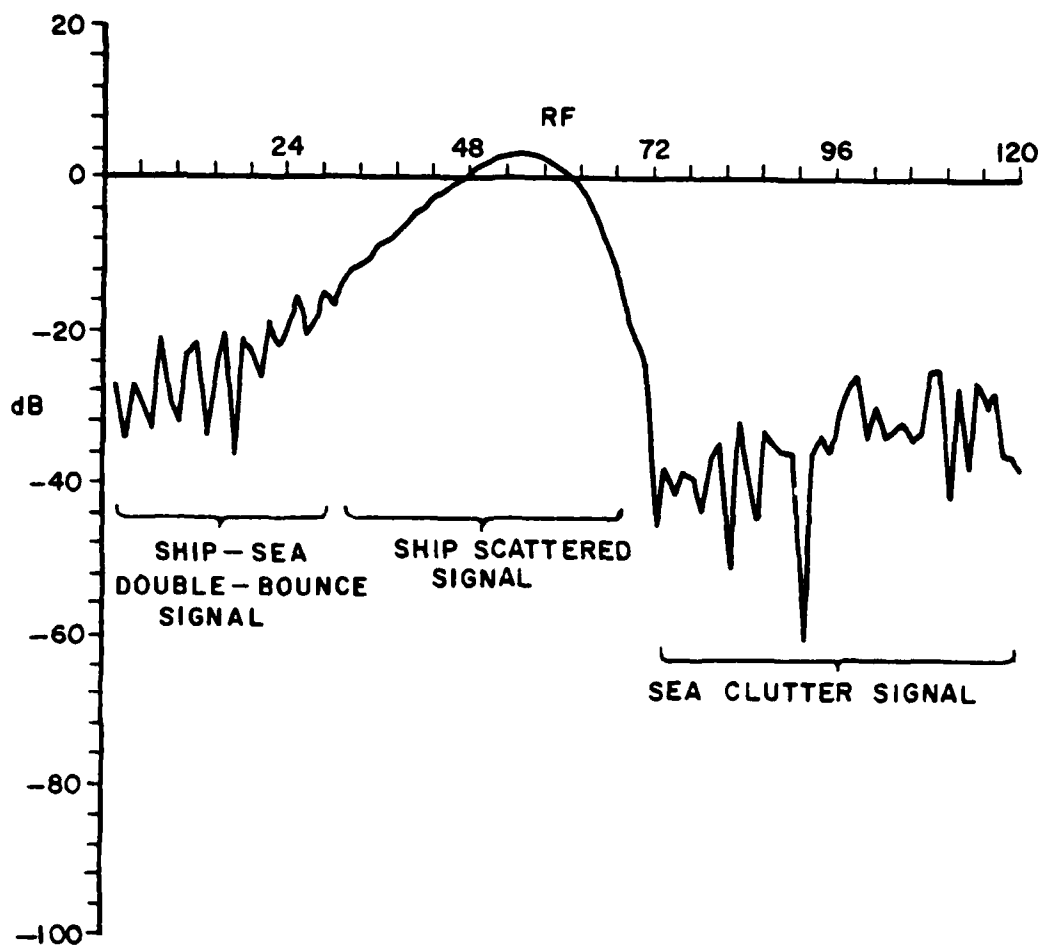


Figure 63. Total scattered signature from the sea and a ship with conical hull. Hollow cone antenna pattern is used. $SAH=45^\circ$, $ATA=30^\circ$, polarization is horizontal. Other dimensions are the same as those shown in Figure 53.

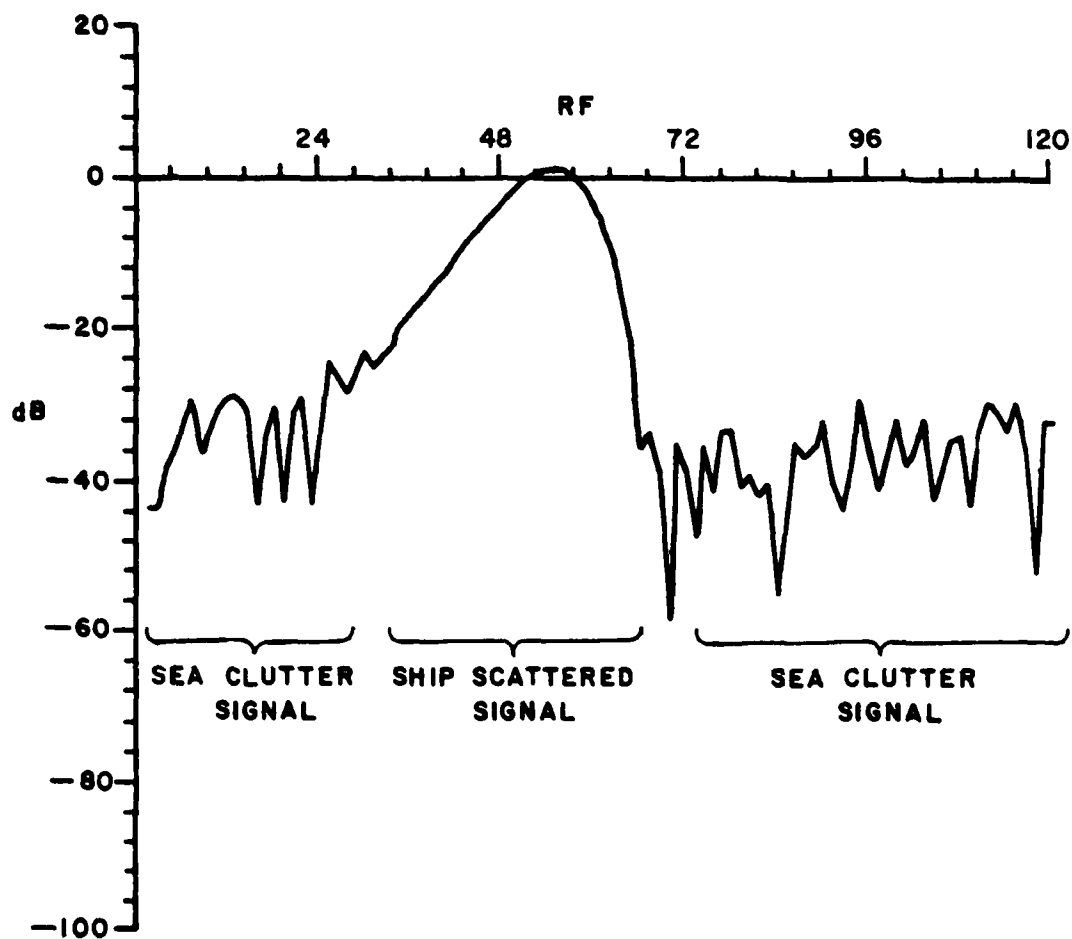
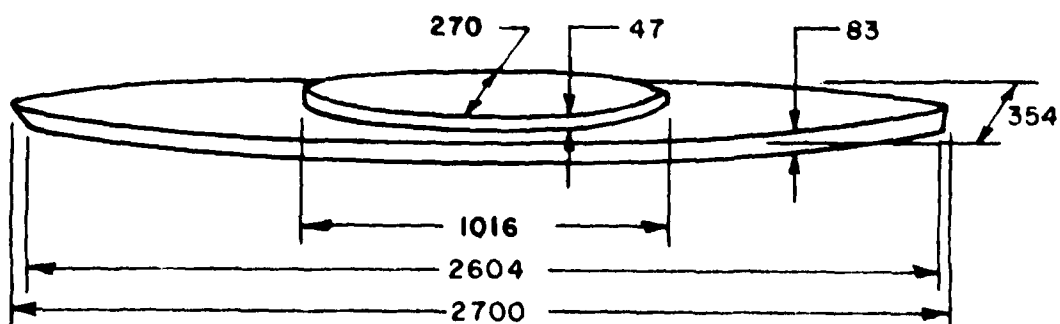


Figure 64. Total scattered signature from the sea and a ship with conical hull. Hollow cone antenna pattern is used.
 $SAH=90^{\circ}$, $ATA=30^{\circ}$, polarization is horizontal.
 Other dimensions are the same as those shown in Figure 53.



(a)



(b)

Figure 65. Actual model and simplified model of ship U.S.S. Missouri. All dimensions are in length units.

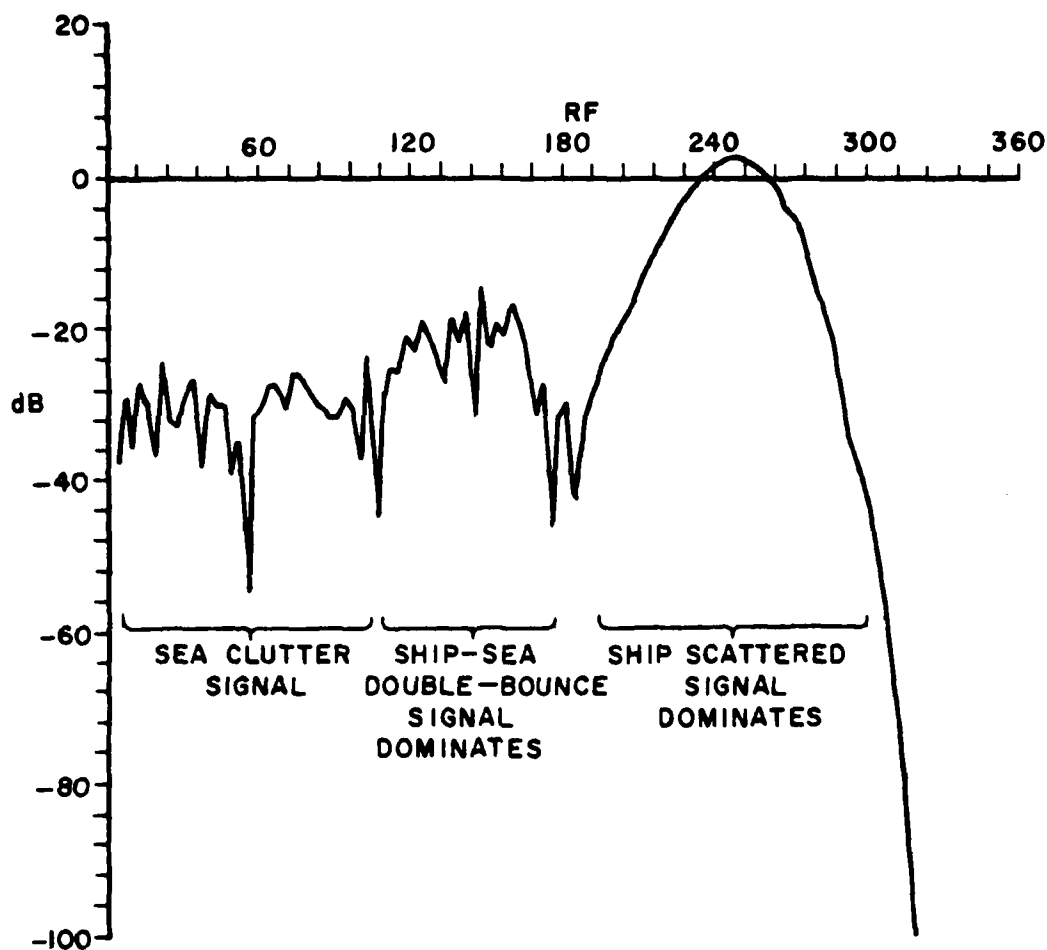


Figure 66. Ship-sea scattered signature from the simplified U.S.S. Missouri model. Pattern cone half angle $ATA=60^\circ$. Antenna approach angle $SAH=0^\circ$. RF is the distance between the antenna and its starting position. Vertical scale represents the received voltage in decibels. Ship's center is located at $RF=450$ length units and ship's dimensions are shown in Figure 65.

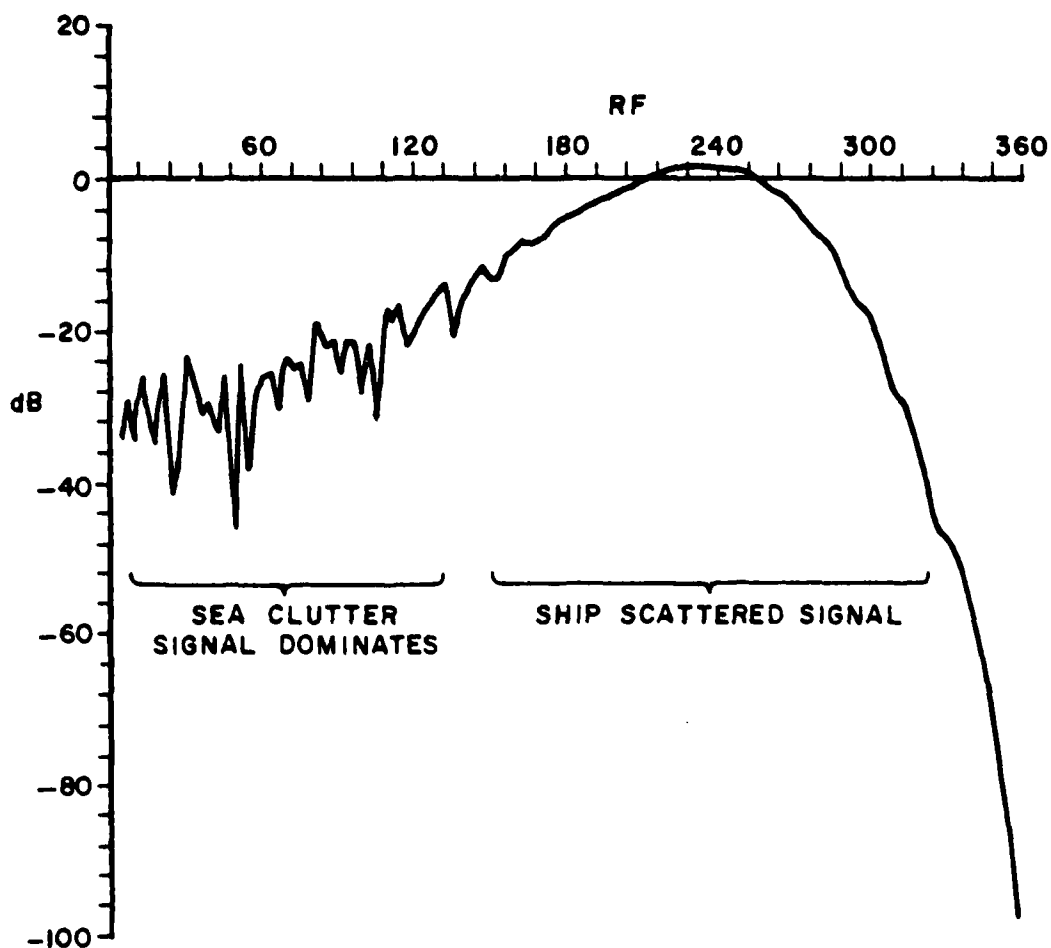


Figure 67. Ship-sea scattered signature from the simplified U.S.S. Missouri model. $SAH=45^\circ$, $ATA=60^\circ$. RF is the distance between the antenna and its starting position and ship's center is located at $RF=540$ length units. Ship's dimensions are shown in Figure 65.

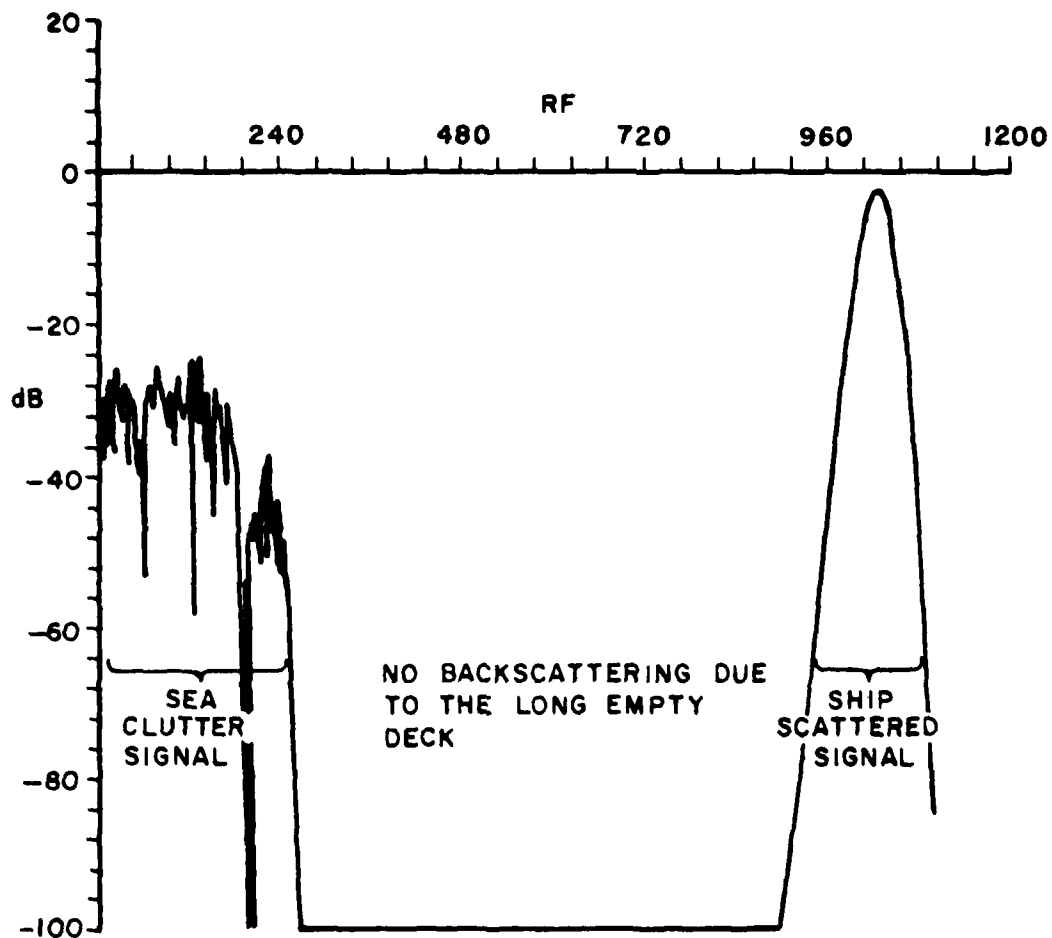


Figure 68. Ship-sea scattered signature from the simplified U.S.S. Missouri model. $SAH=90^\circ$, $ATA=60^\circ$. RF is the distance between the antenna and its starting position, and ship's center is located at $RF=1600$ length units. Ship's dimensions are shown in Figure 65.

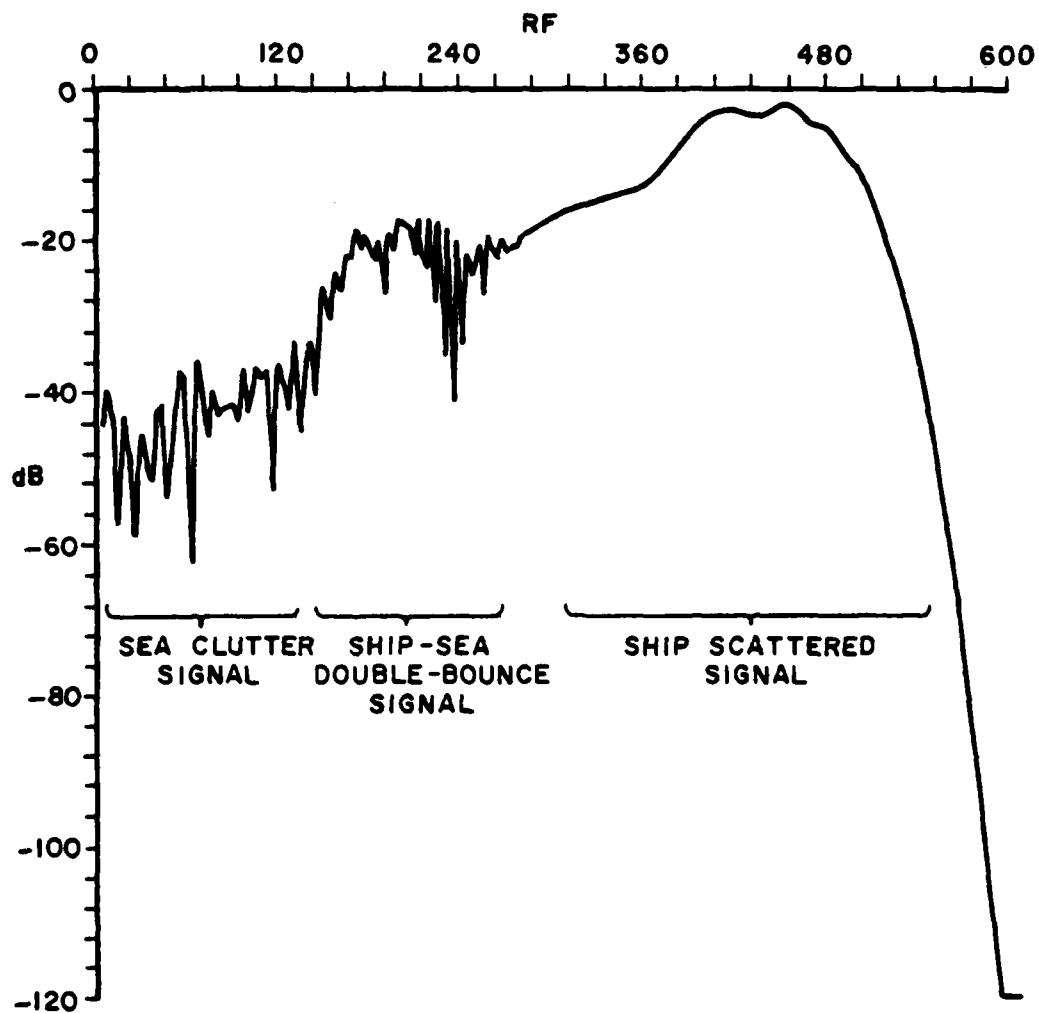


Figure 69. Ship and sea scattered signature from the simplified U.S.S. Missouri model. Pattern cone half angle $ATA=30^\circ$, antenna approach angle $SAH=0^\circ$. RF is the distance between antenna and its starting position. Ship's center is located at $RF=775$ length units. Ship's dimensions are shown in Figure 65.

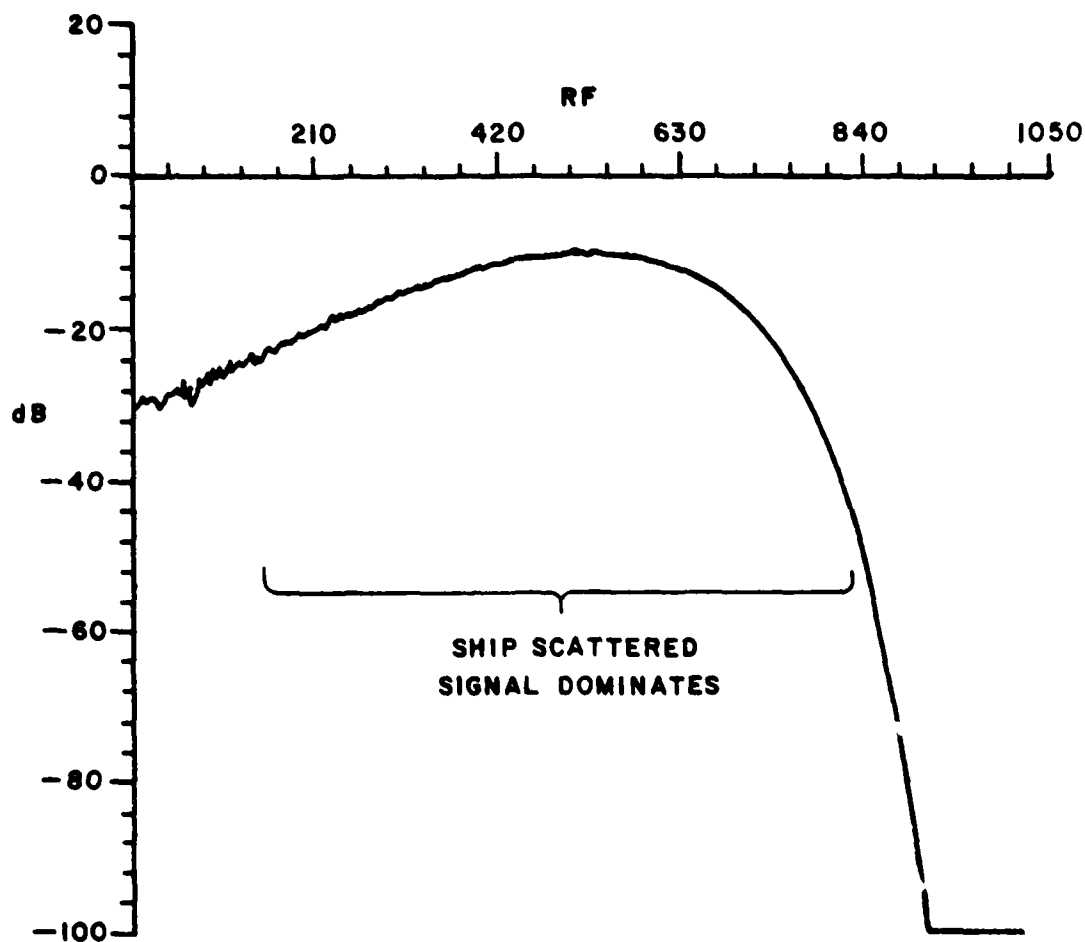


Figure 70. Ship-sea scattered signature from the simplified U.S.S. Missouri model. $SAH=45^\circ$, $ATA=30^\circ$. RF is the distance between the antenna and its starting position, and ship's center is located at $RF=1200$ length units. Ship's dimensions are shown in Figure 65.

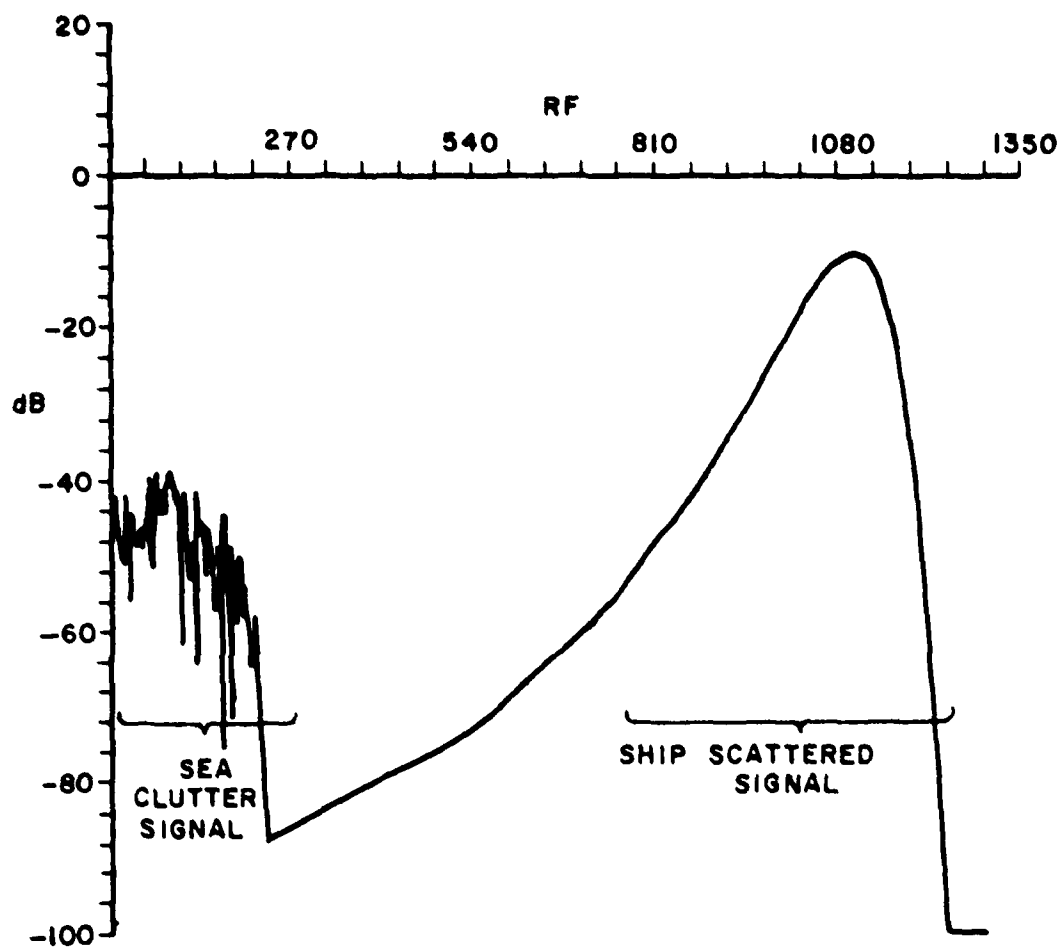


Figure 71. Ship-sea scattered signature from the simplified U.S. Missouri model. $SAH=90^\circ$, $ATA=30^\circ$. RF is the distance between the antenna and its starting position, and ship's center is located at $RF=1200$ length units. Ship's dimensions are shown in Figure 65.

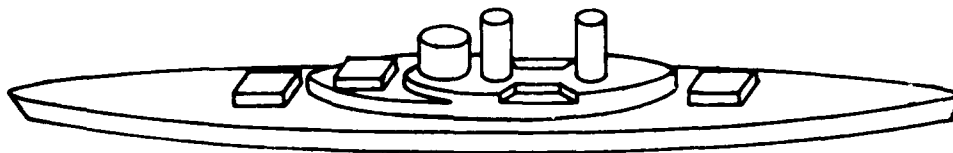


Figure 72. Improved U.S.S. Missouri model.

CHAPTER VII CONCLUSIONS AND RECOMMENDATIONS

The objective of this research has been to develop a simple model for the interaction between a radar system and a ship at sea which is adaptable to short range encounters, and which can be easily elaborated to handle fairly complex ship structures. In the most general form considered in this report, the superstructure of the ship is modelled by an elliptic cylinder, and the hull is modelled by a portion of an elliptic cone. The sea is modelled by an array of rectangular patches, each characterized by a polarization dependent bistatic radar cross-section. The radar system response is represented by an encounter signature, i.e., by the detector voltage as a function of the radar position. The total signature is then found from the (phasor) sum of the contributions from each of the dominant scattering mechanisms. These are the clutter (back-scattered) signal from the sea alone; the reflected and diffracted fields from the ship structure alone; and the double-bounce contribution produced by the fields scattered by the ocean surface onto the ship structure and then back to the radar system (or vice versa).

The fields scattered by the various component parts of the ship are calculated by the Geometrical Theory of Diffraction (GTD), combined with a very fast numerical search technique which was developed to track the reflection and diffraction points on the ship's structure.

From the perspective afforded by the detailed study of the computational procedures described in the preceding chapters, the advantages of this particular ship-sea model should be readily apparent. In the first place, since the GTD assigns a definite ray path to each contribution to the total signature, it is relatively simple to adapt the model to a variety of features found in operating radar systems, e.g., range gates, doppler filters, pulse-to-pulse frequency agility, etc. Secondly, because the total scattered field from each patch is radiated from the center of the patch, the location of which is known, only one point (that on the ship's surface) must be located to define the ray path. Since a large number of paths must be computed (one for each patch at each position of the radar), this feature of the model greatly reduces the overall computation time compared to any model in which two unknown reflection points per path must be tracked. Thirdly, since the actual bistatic scattering cross-section of the ocean is used to determine the strength of the field scattered by each patch, both the clutter signature and the double bounce signature should have the same statistical properties (average power, correlation function, spectrum,

first probability distribution) as do the actual signatures. Thus, one may use the model signatures to evaluate, for example, proposed antenna patterns, detection characteristics, transmitted signal designs, polarization diversity schemes, etc. For example, even though the random clutter signal may occasionally attain large values, i.e., in relation to the ship return, it could be distinguished from the ship return by the fact that it can sustain large values only for very short durations.

Although only relatively few signatures were actually calculated in preparing this report, one can already observe a variety of signature characteristics which may be of value in future system design. For example, it is clear that the "double-bounce" contribution may be significantly larger than the clutter, particularly at broadside and bow or stern aspects, and that the early position of its maximum response is determined by the waterline and hull rather than the superstructure details. On the other hand, (for pencil beam antennas) there are aspects near 45° for which neither the double-bounce nor the ship signature is detectable in the clutter. When a hollow cone antenna pattern was used, the presence of the ship was always detectable even though the clutter level was higher. However, in this case one could observe either a single peak or a double-peak in the overall signature depending again on the aspect angle of the trajectory. As mentioned on page 85, however, one should not use the signatures of the type developed in this report to evaluate system performance, because of the extreme simplicity of modelling the superstructure.

On the basis of these brief observations, and the other results and the signatures of Chapter VII, it may be concluded that the simple ship-sea scattering model developed here offers a convenient method for estimating the performance of a radar system traversing a ship at sea. It should be useful to the system designer in evaluating the effects of such system parameters as antenna pattern, polarization, radar trajectory, range gate, detection criteria, etc., when the modelling of the superstructure has been augmented by appropriate forms (plates, cones, cylinders, blocks, etc.) all of which can be handled by the technique of the GTD implemented here. In addition, the sea surface model can be elaborated to include non-random components (e.g., the bow-wave structure always associated with ships in motion, which may be the dominant surface disturbance in smooth water). Alternatively, one could use measured signatures from an isolated model of the ship, in conjunction with computed signatures for the clutter and double bounce contributions to obtain an overall signature.

APPENDIX A PENCIL BEAM RADIATION FROM A RECTANGULAR APERTURE

An antenna with the rectangular aperture and coordinate system shown in Figure 73, emits a radiated far zone electric field given by

$$E_{\theta} = \frac{j\omega\mu}{4\pi r} e^{-jkr} \int_{-L/2}^{L/2} \int_{-W/2}^{W/2} [\sin\theta J_z(x', z') - \cos\theta \cos\phi J_x(x', z')] e^{jk(x' \sin\theta \cos\phi + z' \cos\theta)} dx' dz' \quad (59)$$

$$E_{\phi} = \frac{j\omega\mu}{4\pi r} e^{-jkr} \sin\phi \int_{-L/2}^{L/2} \int_{-W/2}^{W/2} J_x(x', z') e^{jk(x' \sin\theta \cos\phi + z' \cos\theta)} dx' dz' \quad (60)$$

when the origin of the coordinates is taken at the center of the aperture, and the spherical coordinate system for the radiated field is as shown.

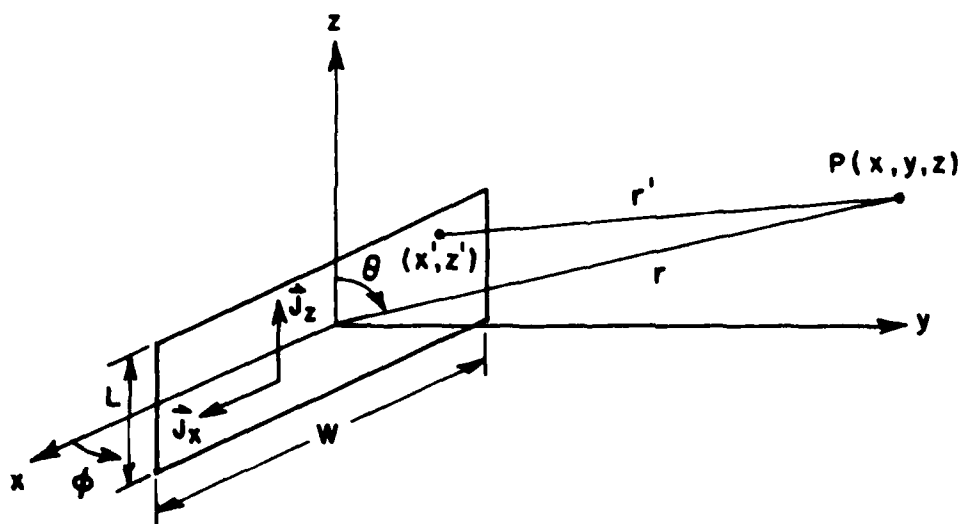


Figure 73. Source coordinate system.

Since the assumed antenna current distribution is Gaussian, the z-directed aperture current is given by

$$J_z(x', z') = J_0 e^{-\pi(x'/a)^2} e^{-\pi(z'/a)^2} \quad (61)$$

$$J_x = 0$$

where a is a constant parameter that determines the beamwidth and has units of length. J_0 is a reference surface current density in units of amperes per meter. Since the Gaussian source function is diminishingly small outside the limits of integration, the integrals can be approximated by letting the limits go to infinity, with the result that

$$\begin{aligned} E_\theta &= \frac{j\omega\mu}{4\pi r} J_0 a^2 e^{-jkr} \sin\theta e^{-\frac{(ka \cos\theta)^2}{4\pi}} e^{-\frac{(ka \sin\theta \cos\phi)^2}{4\pi}} \\ &= \frac{j\omega\mu}{4\pi r} J_0 a^2 e^{-jkr} \sin\theta e^{-\frac{(ka)^2}{4\pi} (\cos^2\theta + \sin^2\theta \cos^2\phi)} \quad (62) \end{aligned}$$

$$E_\phi = 0.$$

Similarly, for an x-directed Gaussian aperture current, the electric fields are given by

$$E_\theta = \frac{-j\omega\mu}{4\pi r} J_0 a^2 e^{-jkr} \cos\theta \cos\phi e^{-\frac{(ka)^2}{4\pi} (\cos^2\theta + \sin^2\theta \cos^2\phi)} \quad (63)$$

$$E_\phi = \frac{j\omega\mu}{4\pi r} J_0 a^2 e^{-jkr} \sin\phi e^{-\frac{(ka)^2}{4\pi} (\cos^2\theta + \sin^2\theta \cos^2\phi)} \quad (64)$$

Since the antenna generates a narrow broadside ($\theta=90^\circ$, $\phi=90^\circ$) beam, and $\cos\theta \cos\phi$ is vanishingly small near the broadside direction, E_θ is negligible for the x polarized source distribution.

To conclude, the fields that are incident upon the sea surface and the ship are given by Equations (62) and (64) for a vertically (J_z) and horizontally (J_x) polarized antenna, respectively. In the report, all the above calculations have assumed $J_0 a^2 = 1$ ampere-meter.

APPENDIX B

BISTATIC SCATTERING MATRIX ELEMENTS (slightly rough surface)

The bistatic scattering matrix elements for a slightly rough surface with homogeneous dielectric material are given by

$$\alpha_{hh} = - \frac{(\epsilon_r - 1) \cos \phi_s}{(\cos \theta_i + \sqrt{\epsilon_r - \sin^2 \theta_i})(\cos \theta_s + \sqrt{\epsilon_r - \sin^2 \theta_s})} \quad (65a)$$

$$\alpha_{vh} = \sin \phi_s \frac{-(\epsilon_r - 1) \sqrt{\epsilon_r - \sin^2 \theta_s}}{(\cos \theta_i + \sqrt{\epsilon_r - \sin^2 \theta_i})(\epsilon_r \cos \theta_s + \sqrt{\epsilon_r - \sin^2 \theta_s})} \quad (65b)$$

$$\alpha_{hv} = \sin \phi_s \frac{(\epsilon_r - 1) \sqrt{\epsilon_r - \sin^2 \theta_i}}{(\epsilon_r \cos \theta_i + \sqrt{\epsilon_r - \sin^2 \theta_i})(\cos \theta_s + \sqrt{\epsilon_r - \sin^2 \theta_s})} \quad (65c)$$

$$\alpha_{vv} = \frac{(\epsilon_r - 1)(\epsilon_r \sin \theta_i \sin \theta_s - \cos \phi_s \sqrt{\epsilon_r - \sin^2 \theta_i} \sqrt{\epsilon_r - \sin^2 \theta_s})}{(\epsilon_r \cos \theta_i + \sqrt{\epsilon_r - \sin^2 \theta_i})(\epsilon_r \cos \theta_s + \sqrt{\epsilon_r - \sin^2 \theta_s})} \quad (65d)$$

In the above expressions, ϵ_r , the relative permittivity, may be either real or complex (indicating lossless or lossy material), and may be either greater, equal to, or less than unity in magnitude. The angles θ_i , θ and ϕ are defined in Figure 8. The first index η of $\alpha_{\eta\epsilon}$ is the scattered polarization state and the second index ϵ is the incident polarization state. For a perfect conducting surface $\epsilon_r \rightarrow \infty$.

APPENDIX C
BISTATIC SPECULAR REFLECTION COEFFICIENTS
(very rough surface)

The specular reflection coefficients for a surface with large scale roughness are given by²¹

$$R_{hh} = \frac{\sin\theta_i \sin\theta_s \sin^2\phi_s R_{||}(\nu) + a_2 a_3 R_{\perp}(\nu)}{4 \sin^2(\nu) \cos^2(\nu)} \quad (66a)$$

$$R_{vh} = -\sin\phi_s \frac{a_2 \sin\theta_s R_{||}(\nu) - a_3 \sin\theta_i R_{\perp}(\nu)}{4 \sin^2(\nu) \cos^2(\nu)} \quad (66b)$$

$$R_{hv} = -\sin\phi_s \frac{a_2 \sin\theta_s R_{\perp}(\nu) - a_3 \sin\theta_i R_{||}(\nu)}{4 \sin^2(\nu) \cos^2(\nu)} \quad (66c)$$

$$R_{vv} = -\frac{\sin\theta_i \sin\theta_s \sin^2\phi_s R_{\perp}(\nu) + a_2 a_3 R_{||}(\nu)}{4 \sin^2(\nu) \cos^2(\nu)} \quad (66d)$$

where

$$a_2 = \cos\theta_i \sin\theta_s + \sin\theta_i \cos\theta_s \cos\phi_s$$

$$a_3 = \sin\theta_i \cos\theta_s + \cos\theta_i \sin\theta_s \cos\phi_s$$

The quantities $R_{||}(\nu)$ and $R_{\perp}(\nu)$ are the Fresnel reflection coefficients defined as

$$R_{||}(\nu) = \frac{\epsilon_r \cos\nu - \sqrt{\epsilon_r^2 - \sin^2\nu}}{\epsilon_r \cos\nu + \sqrt{\epsilon_r^2 - \sin^2\nu}} \quad (67a)$$

$$R_1(v) = \frac{\cos v - \sqrt{\epsilon_r - \sin^2 v}}{\cos v + \sqrt{\epsilon_r - \sin^2 v}} \quad (67b)$$

where v is the local angle of incidence at the specular reflecting facets, and is given by

$$\cos^2 v = \frac{1}{2} (1 - \sin \theta_i \sin \theta_s \cos \phi_s + \cos \theta_i \cos \theta_s) \quad (68)$$

with θ_i , θ_s and ϕ_s defined in Figure 8. Note that special care is required in evaluating these coefficients in the back-scattering direction. For this reason, a somewhat different procedure for evaluating these coefficients are used in the computer programs in this report.

APPENDIX D COMPARISON OF THE MEASURED AND CALCULATED FIELDS SCATTERED BY A CIRCULAR CONE

In order to validate the calculation for the reflected field from an elliptic cone, the most appropriate verification is to compare the results with experimental measurements, since neither calculated nor measured results are available in the standard literature. However, because the elliptic cone is very difficult to fabricate, the experimental data reported here, and consequently the theoretical solution derived in this appendix, is restricted to the case of the circular cone. The experimental results were obtained by Dr. Edward Pelton in the ESL (ElectroScience Laboratory) microwave anechoic chamber using S-band setups. The field scattered by the circular cone is received by a rectangular horn antenna and detected by a Scientific Atlanta receiver.

The experimental configuration of the circular cone is illustrated in Figure 74. A half-wave dipole which is located in the near zone of the cone illuminates the cone with either vertical or horizontal polarization, and the near-zone field is measured azimuthally around the cone. Since the measured result includes not only the reflected field but also the incident field plus the surface diffracted creeping wave, it is essential to calculate all these fields in order to have an adequate comparison. The reflected field in the deep lit region (away from the shadow boundary) is calculated by the same Geometrical Optics technique that is employed for calculating the field reflected from the ship's hull. The reflected field near the shadow boundary (transition region) and the surface diffracted creeping wave are both calculated by the uniform GTD method using the formulation of Pathak²³.

Before calculating the creeping wave field it is essential to accurately locate the geodesic ray path for each creeping wave on the conical surface. The geodesic curve on a surface is the shortest path between two points. For given locations of the source (x_s, y_s, z_s) and observation point (x_o, y_o, z_o) , the geodesic ray path on a circular cone can be found as follows:

Let the incident and the outgoing vector tangent points be denoted by \hat{Q}_1 and \hat{Q}_2 , respectively, as illustrated in Figure 75, with

$$\begin{aligned}\hat{Q}_1 &= \rho_1 \cos v_1 \hat{x} + \rho_1 \sin v_1 \hat{y} + \rho_1 \cot \theta_0 \hat{z} \\ \hat{Q}_2 &= \rho_2 \cos v_2 \hat{x} + \rho_2 \sin v_2 \hat{y} + \rho_2 \cot \theta_0 \hat{z}\end{aligned}\tag{69}$$

Diagram illustrating the field of a dipole source near a perfectly conducting sphere. The diagram shows the incident field (solid line), the reflected field (dashed line), and the creeping wave (dotted line) along the surface of the sphere. The dipole source is located at a distance x from the sphere's surface. The field point is located at a distance y from the center of the sphere.

Legend:

- CREEPING WAVE
- - - REFLECTED FIELD
- INCIDENT FIELD

Labels:

- DIPOLE SOURCE
- FIELD POINT
- x
- y

114

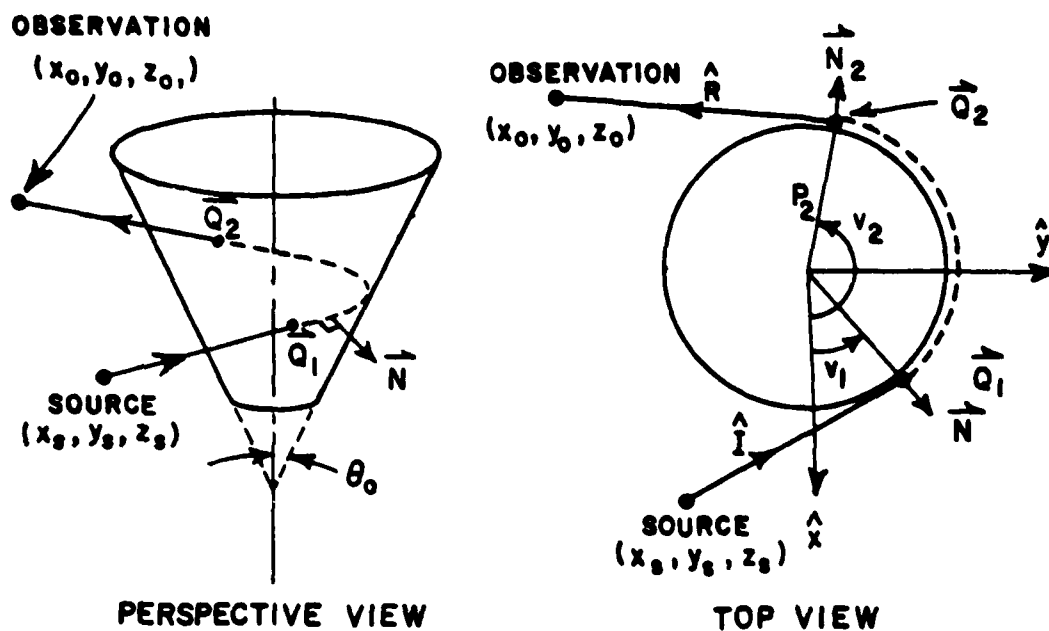


Figure 75. Diffraction mechanism for creeping wave.

where ρ_1 , ρ_2 , v_1 , v_2 are the unknowns to be solved for, with ρ_1 being horizontal radii of the cone and v_1 being angular positions measured from the x-axis; θ_0 is the cone half angle.

The incident vector \hat{I} and the outgoing vector \hat{R} can be described by

$$\begin{aligned}\hat{I} &= (\rho_1 \cos v_1 - x_s) \hat{x} + (\rho_1 \sin v_1 - y_s) \hat{y} + (\rho_1 \cot \theta_0 - z_s) \hat{z} \\ \hat{R} &= (x_o - \rho_2 \cos v_2) \hat{x} + (y_o - \rho_2 \sin v_2) \hat{y} + (z_o - \rho_2 \cot \theta_0) \hat{z} .\end{aligned}\quad (70)$$

The normal to the surface is given by (see Equation (46))

$$\vec{N}_1 = \cos v_1 \cot \theta_0 \hat{x} + \sin v_1 \cot \theta_0 \hat{y} - \hat{z} .\quad (71)$$

Since the ray path has to be everywhere perpendicular to the surface normal, at the incident point one must satisfy

$$\hat{I} \cdot \vec{N}_1 = 0$$

which results in the equation

$$z_s - \cot \theta_0 (x_s \cos v_1 + y_s \sin v_1) = 0. \quad (72)$$

At the outgoing tangent point one should have

$$\vec{R} \cdot \vec{N}_2 = 0$$

which yields the equation

$$z_0 - \cot \theta_0 (x_0 \cos v_2 + y_0 \sin v_2) = 0. \quad (73)$$

Equations (72) and (73) allow one to solve for the angular positions v_1 and v_2 independent of the distances ρ_1 and ρ_2 , which can be determined by the following method.

If a circular cone is cut open along a generating line and is un-rolled onto a flat surface, one obtains the so-called developed surface, which is illustrated in Figure 76. The distances from the tip of the cone to the source and observation points are given by

$$l_1 = \sqrt{x_s^2 + y_s^2 + z_s^2}$$

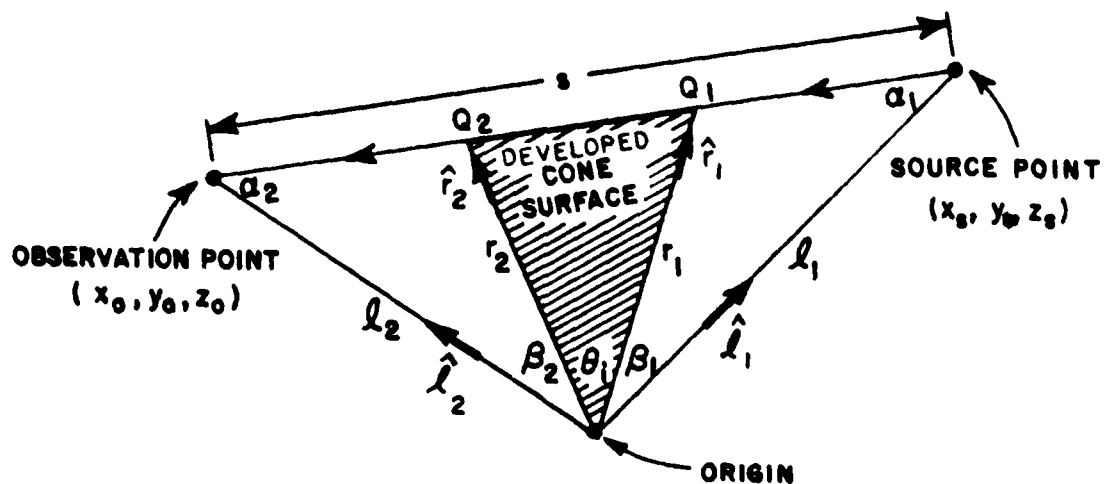


Figure 76. Developed cone surface.

and

$$l_2 = \sqrt{x_0^2 + y_0^2 + z_0^2},$$

respectively, with unit direction vectors given by

$$\hat{l}_1 = (x_s \hat{x} + y_s \hat{y} + z_s \hat{z})/l_1$$

$$\hat{l}_2 = (x_0 \hat{x} + y_0 \hat{y} + z_0 \hat{z})/l_2$$

The generating lines for the cone at the two tangent points are described by the following unit vectors

$$\hat{r}_1 = \cos v_1 \sin \theta_0 \hat{x} + \sin v_1 \sin \theta_0 \hat{y} + \cos \theta_0 \hat{z}$$

$$\hat{r}_2 = \cos v_2 \sin \theta_0 \hat{x} + \sin v_2 \sin \theta_0 \hat{y} + \cos \theta_0 \hat{z}.$$

The angles θ_1 , β_1 , β_2 , as shown in Figure 76, are given by

$$\theta_1 = (v_2 - v_1) \sin \theta_0$$

$$\beta_1 = \arccos(\hat{l}_1 \cdot \hat{r}_1)$$

$$\beta_2 = \arccos(\hat{l}_2 \cdot \hat{r}_2)$$

Thus, the ray-path distance between the source and observation points is

$$s = [l_1^2 + l_2^2 - 2l_1l_2 \cos(\beta_1 + \beta_2 + \theta_1)]^{1/2}, \quad (74)$$

and the angles α_1 and α_2 , as illustrated in the same figure, are given by

$$\alpha_1 = \arccos[(l_1^2 + s^2 - l_2^2)/2l_1s] \quad (75)$$

$$\alpha_2 = \pi - \alpha_1 - (\beta_1 + \beta_2 + \theta_1)$$

Finally, ρ_1 and ρ_2 can be obtained from

$$\rho_1 = \frac{l_1 \sin \alpha_1}{\sin(\alpha_1 + \beta_1)} \sin \theta_0$$

$$\rho_2 = \frac{l_2 \sin \alpha_2}{\sin(\alpha_2 + \beta_2)} \sin \theta_0.$$

After obtaining the locations of the two tangent points (ρ_1, v_1) and (ρ_2, v_2) , one is able to solve for the constants c_1 and c_2 in the geodesic equation,

$$\rho_i = c_i \sec[(v_i - c_2) \sin \theta_0] . \quad (76)$$

The surface diffracted field of the creeping wave (see Figure 77) has been derived by Pathak and is given by

$$\vec{E}^d(p) = \vec{E}^i(Q_1) \cdot [\hat{b}_1 \hat{b}_2 D_s + \hat{n}_1 \hat{n}_2 D_h] \int \frac{d\eta}{d\eta_2} \sqrt{\frac{\rho_c}{s(\rho_c + s)}} e^{-jks} \quad (77)$$

where \hat{b}_1 and \hat{b}_2 are the binormal unit vectors ($\hat{b}_1 = \hat{t}_1 \times \hat{n}_1$, $\hat{b}_2 = \hat{t}_2 \times \hat{n}_2$), and $\vec{E}^i(Q_1)$ is the arbitrary polarized incident field at point Q_1 ;

$\int d\eta_1/d\eta_2 = \sqrt{\frac{s'}{s'+t}}$ is the ray spreading factor;

ρ_c is the radius of the spherical wave front at Q_2 and is given by $\rho_c = s' + t$ with t being the geodesic path length.

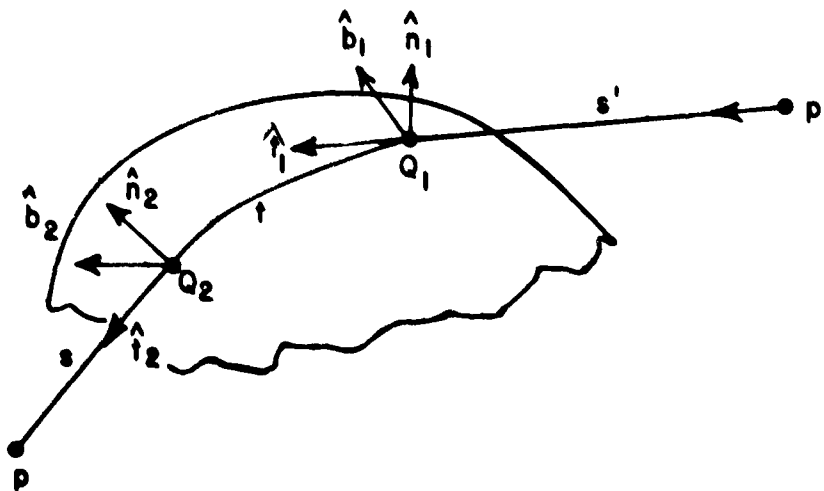


Figure 77. Configuration of surface diffracted creeping wave.

The diffraction coefficient D_s and D_h for the soft and hard boundary conditions, respectively, are given by

$$D_{s,h} = -\sqrt{m(Q_1)m(Q_2)} e^{-jkt} \sqrt{\frac{2}{k}} \left\{ \frac{e^{-j\pi/4}}{2\sqrt{\pi\xi^S}} [1-F(x^S)] + \hat{\rho}_s(\xi^S) \right\} \quad (7R)$$

where

$$m(Q_i) = \left[\frac{k\rho_g(Q_i)}{2} \right]^{1/3},$$

and

$$\rho_g(Q_i) = \frac{\rho_i^3}{c_1^2 \cos\theta_0 \cos^2 w_i}$$

where $w_i = \frac{\pi}{2} - \alpha_i - \beta_i$

is the equation for the radius of curvature of the geodesic ray path and is obtained in a fashion similar to Equation (53). The constant c_1 is the same constant as that shown in Equation (76). The distance parameter (ξ^S) from Q_1 to Q_2 is defined by

$$\xi^S = \int_{Q_1}^{Q_2} \frac{m(t')}{\rho_g(t')} dt'.$$

For a circular cone, ξ^S is

$$\xi^S = \frac{1}{2} k\rho_1 \sin\Omega_1)^{1/3} |v_2 - v_1| \cos^{2/3}\theta_0 \quad (7a)$$

where

$$\Omega_1 = \arcsin \left\{ \frac{\rho_2}{s \sin\theta_0} \sin|(v_2 - v_1) \sin\theta_0| \right\}.$$

The function $F(x^S)$ is formulated in terms of the Fresnel integral,

$$F(x^S) = 2j\sqrt{x^S} e^{-jx^S} \int_{\sqrt{x^S}}^{\infty} e^{-j\tau^2} d\tau \quad (80)$$

where

$$x^S = \frac{ks's}{s'+s} \frac{[\xi^S]^2}{2m(Q_1)m(Q_2)}.$$

The function $\hat{P}_S^h(\xi^S)$ is the Pekeris' caret function and is identical to the definitions of Logan²⁴ and Pathak²³.

The geometrical optics field will not blend accurately with the field in the shadow region unless the geometrical reflected field is modified in the transition region according to (see Figure 78)

$$E^r(\rho) = E^i(Q_R) \cdot \bar{R} \sqrt{\frac{\bar{\rho}_1^r \bar{\rho}_2^r}{(\bar{\rho}_1^r + s)(\bar{\rho}_2^r + s)}} e^{-jks} \quad (81)$$

where
$$\frac{1}{\bar{\rho}_1^r} = \frac{1}{s'} + \frac{1}{\rho_1^r}$$

with ρ_1^r being the principal radii of curvature of the reflected wavefront at the reflection point Q_R for a plane wave incidence, and s' being the distance between the source point and Q_R .

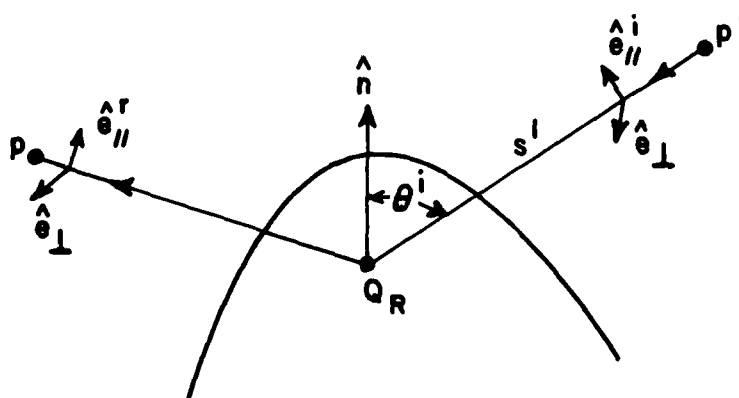


Figure 78. Configuration of curved surface reflection.

The dyadic reflection coefficient is given by

$$R = R_s \hat{e}_s \hat{e}_s + R_h \hat{e}_h^i \hat{e}_h^r$$

$$\text{where } R_{sh} = -\sqrt{\frac{-4}{\xi^L}} e^{-j(\xi^L)^3/12} \left\{ \frac{e^{-j\pi/4}}{2\sqrt{\pi} \xi} \left[1 - F(x^L) + \hat{p}_{sh}(\xi^L) \right] \right\}$$

$$\text{with } x^L = 2 \frac{ks's}{s'+s} \cos^2 \theta^i$$

$$\xi^L = -2m h^{1/3} \cos \theta^i$$

$$\text{where } m = \left[\frac{k \rho_g(Q_R)}{2} \right]^{1/3}, \quad h = \left[1 + \frac{\rho_g(Q_R) \cos^2 \theta^i}{\rho_{tn}(Q_R)} \right]^{-1}$$

Here $\rho_g(Q_R)$ is the radius of curvature of the surface at Q_R in the plane of incidence; whereas, $\rho_{tn}(Q_R)$ is the radius of the surface in the orthogonal plane.

The reflected field from the circular cone is calculated by Equation (81) if the field point is close to the shadow boundary or by Equation (1) if the field point is in the deep lit region. The total field is then composed of the incident field and the reflected field plus the surface diffracted creeping wave calculated by Equation (77). The comparison between this calculated total field and the measured result from the geometry given in Figure 74 is shown in Figure 79. It can be seen that excellent agreement is obtained between the GTD analysis and the measurement. Consequently, one can conclude that the reflected field from the elliptic-cone shaped ship hull has been correctly calculated.

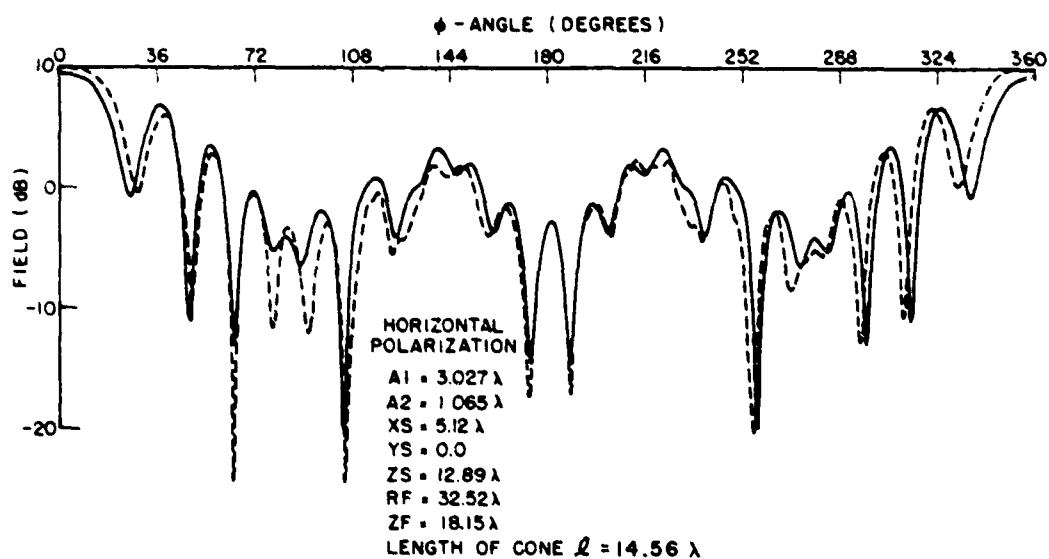
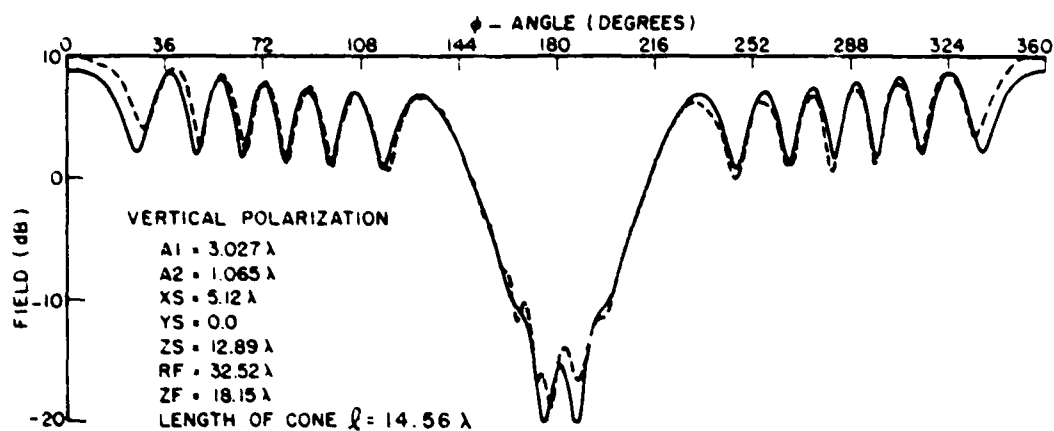


Figure 79. Field scattered from the circular cone. (Solid curve is the calculation, dashed curve is the measurement.)

REFERENCES

1. Peake, W. H. and Barrick, D. E., "Scattering from Surfaces with Different Roughness Scales; Analysis and Interpretation," Report 1388-26, September 1967, The Ohio State University Electro-Science Laboratory, Department of Electrical Engineering; prepared under Grant Number NSG-213-61 for National Aeronautics and Space Administration.
2. Kouyoumjian, R. G. and Pathak, P. H., "A Uniform Geometrical Theory of Diffraction for an Edge in a Perfectly Conducting Surface," Proc. IEEE, vol. 62, No. 11, November 1974.
3. Sommerfeld, A., Optics, Academic Press, Inc., New York, 1954, pp. 245-265.
4. Pauli, W., "An Asymptotic Series for Functions in the Theory of Diffraction of Light," Phys. Rev., 54 (1 December 1938), pp. 924-931.
5. Keller, J. B., "Geometrical Theory of Diffraction," Jour. Optical Soc. Amer., 52 (February 1962), pp. 116-130.
6. Hutchins, D. L., and Kouyoumjian, R. G., "A New Asymptotic Solution to the Diffraction by a Wedge," URSI 1967 Spring Meeting, Ottawa, Canada, pp. 154-155.
7. Pathak, P. H. and Kouyoumjian, R. G., "The Dyadic Diffraction Coefficient for a Perfectly Conducting Wedge," Report 2183-4, June 1970, The Ohio State University ElectroScience Laboratory, Department of Electrical Engineering; prepared under Contract AF19(628)-5929 for Air Force Cambridge Research Laboratories. (AFCRL-69-0546) (AD 707821)
8. Rice, S., (1963), "The Reflection of Electromagnetic Waves by Slightly Rough Surfaces," in The Theory of Electromagnetic Waves edited by M. Kline, Interscience Publishers, also Dover.
9. Peake, W. H., "The Interaction of Electromagnetic Waves with Some Natural Surfaces," Ph.D. Dissertation, The Ohio State University. Also appears as Report 898-2, 30 May 1959, Antenna Laboratory, The Ohio State University; prepared under Contract AF33(616)-6158, Wright Air Development Center, Wright-Patterson Air Force Base, Ohio; Also "Theory of Radar Return from Terrain," IRE Convention Record, vol. 7, p. 27.

10. Phillips, O. M., (1966), Dynamics of the Upper Ocean, Cambridge University Press, London, pp. 109-119.
11. Valenzuela, G. R., et al., "Ocean Spectra for the High-Frequency Waves as Determined from Airborne Radar Measurements," Jour. of Marine Research, vol. 29, 2, 1971.
12. Semenov, B. (1966), "An Approximate Calculation of Scattering of Electromagnetic Waves from a Slightly Rough Surface," *Radio-tekhnika i Elektronika* (USSR), 11, p. 1351 (English Translation).
13. Kodis, R., (1966), "A Note on the Theory of Scattering from an Irregular Surface," *IEEE Transactions on Antennas and Propagation*, AP-14, No. 1, p. 77.
14. Barrick, D. E., "A More Exact Theory of Backscattering from Statistically Rough Surfaces," Report 1388-18, August 1965, The Ohio State University ElectroScience Laboratory, Department of Electrical Engineering; prepared under Grant NSG-213-61, National Aeronautics and Space Administration, Washington, D.C.
15. Muhleman, D. (1964), "Radar Scattering from Venus and the Moon," *The Astronomical Journal*, 69, No. 1, p. 34.
16. Cox, C. and Munk, W., *Bull. Scripps, Institute of Oceanography, University of California*, 6, 401 (1956).
17. Beckmann, P., "Shadowing of Random Rough Surfaces," *IEEE Transactions Antenna Propagation*, vol. AP-13, pp. 384-388, May 1965.
18. Marhefka, R. J., "Analysis of Aircraft Wing-Mounted Antenna Patterns," Report 2902-25, June 1976, The Ohio State University ElectroScience Laboratory, Department of Electrical Engineering; prepared under Grant NGL 36-008-138 for National Aeronautics and Space Administration, Hampton, Virginia.
19. Lee, S. W., "Differential Geometry for GTD Applications," Report No. 77-21, October 1977, Electromagnetics Laboratory, University of Illinois, Department of Electrical Engineering; supported by Grant NSF ENG 73-08218, National Science Foundation, Washington, D.C.
20. Lipschutz, M. M., Theory and Problems of Differential Geometry, Schaum's Outline Series, McGraw-Hill Book Co., 1969.

21. Barrick, D. E., "Rough Surface Scattering Based on the Specular Point Theory," IEEE Trans. Antennas and Propagation, vol. AP-16, No. 4, July 1968, pp. 449-454.
22. Walter, C. H., Traveling Wave Antennas, Dover Publications, Inc., New York, 1970, pp. 46-85.
23. Pathak, P. H., "An Asymptotic Result for the Scattering of a Plane Wave by a Smooth Convex Cylinder," to be published.
24. Logan, N. A., "General Research in Diffraction Theory," Vol. I, LMSD-288087; and Vol. II, LMSD-288088, Missiles and Space Division, Lockheed Aircraft Corp., 1959.
25. Valenzuela, G., "Depolarization of EM waves by slightly Rough Surfaces," IEEE Transactions on Antennas and Propagation, AP-15, No. 4, p. 552, 1967.